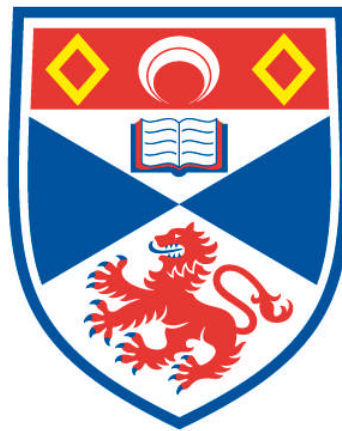


APPLICATIONS OF MICROFLUIDICS AND OPTICAL MANIPULATION FOR PHOTOPORATION AND IMAGING

Helen Anne Rendall

**A Thesis Submitted for the Degree of PhD
at the
University of St Andrews**



2015

**Full metadata for this item is available in
Research@StAndrews:FullText
at:**

<http://research-repository.st-andrews.ac.uk/>

Please use this identifier to cite or link to this item:

<http://hdl.handle.net/10023/6622>

This item is protected by original copyright

**This item is licensed under a
Creative Commons Licence**

Applications of microfluidics and optical manipulation for photoporation and imaging

Helen Anne Rendall



University of
St Andrews

This thesis is submitted in partial fulfilment for the degree of
Doctor of Philosophy
at the
University of St Andrews

24th October 2014

Declaration

1. Candidates declarations:

I, Helen Anne Rendall, hereby certify that this thesis, which is approximately 31000 words in length, has been written by me, and that it is the record of work carried out by me, or principally by myself in collaboration with others as acknowledged, and that it has not been submitted in any previous application for a higher degree.

I was admitted as a research student in October 2010 and as a candidate for the degree of Doctor of Philosophy in June 2011; the higher study for which this is a record was carried out in the University of St Andrews between 2010 and 2014.

Signature of candidate: Date:

2. Supervisors declaration:

I hereby certify that the candidate has fulfilled the conditions of the Resolution and Regulations appropriate for the degree of Doctor of Philosophy in the University of St Andrews and that the candidate is qualified to submit this thesis in application for that degree.

Signature of supervisor: Date:

3. Permission for publication:

In submitting this thesis to the University of St Andrews I understand that I am giving permission for it to be made available for use in accordance with the regulations of the University Library for the time being in force, subject to any copyright vested in the work not being affected thereby. I also understand that the title and the abstract will be published, and that a copy of the work may be made and supplied to any bona fide library or research worker, that my thesis will be electronically accessible for personal or research use unless exempt by award of an embargo as requested below, and that the library has the right to migrate my thesis into new electronic forms as required to ensure continued access to the thesis. I have obtained any third-party copyright permissions that may be required in order to allow such access and migration, or have requested the appropriate embargo below.

The following is an agreed request by candidate and supervisor regarding the publication of this thesis:

PRINTED COPY - No embargo on print copy

ELECTRONIC COPY - No embargo on electronic copy

0. DECLARATION

Signature of candidate: Date:
Signature of supervisor: Date:

Abstract

Optical manipulation covers a wide range of techniques to guide and trap cells using only the forces exerted by light. Another optical tool is photoporation, the technique of injecting membrane-impermeable molecules using light, which has become an important alternative to other injection techniques. Together they provided sterile tools for manipulation and molecule delivery at the single-cell level.

In this thesis, the properties of low Reynolds fluid flows are exploited to guide cells through a femtosecond Bessel beam. This design allows for high-throughput optical injection of cells without the need to individually target cells. A method of ‘off-chip’ hydrodynamic focusing was evaluated and was found to confine 95.6% of the sample within a region which would receive a femtosecond dose compared to 20% without any hydrodynamic focusing. The system was tested using two cell lines to optically inject the membrane-impermeable dye, propidium iodide. This resulted in an increase of throughput by an order of magnitude compared to the previous microfluidic design (to up to 10 cells s^{-1}).

Next optical trapping and photoporation were combined to create a multimodal workstation. The system provides 3D beam control using spatial light modulators integrated into a custom user interface. The efficiency of optical injection of adherent cells and trapping capabilities were tested. The development of the system provides the groundwork for exploration of the parameters required for photoporation of non-adherent cells.

Finally optical trapping is combined with temporally focused multiphoton illumination for scanless imaging. The axial resolution of the system was measured using different microscope objectives before imaging cells stained with calcein. Both single and a pair of recently trypsinised cells were optically trapped and imaged. The position of the trapped cells was manipulated using a spatial light modulator in order to obtain a z-stack of images without adjusting the objective position.

Acknowledgements

I would like to begin by thanking my supervisor, Prof. Kishan Dholakia for giving me the opportunity to work in the Optical Manipulation Group and for his support and guidance throughout the course of my PhD. I am also very grateful to Prof. Frank Gunn-Moore for his guidance on the biological aspects I have encountered. Next I would like to personally thank Praveen and Rob for their encouragement to pursue a PhD and for teaching me the tricks of the trade when working with microfluidics.

I have had the privilege of working with a number of great people and those who have directly been involved with the projects presented in this thesis are acknowledged at the end of each chapter. Whilst I can't name them all, I would like to thank the members of the Optical Manipulation Group for their insight and for sharing their experiences over lunch, coffee and cake.

Special thanks go to my family, Mum, Dad and Claire for their support over the years. Finally I would like to thank Linus for his encouragement over the final stretch of my PhD. Thank you to you all.

0. ACKNOWLEDGEMENTS

Publications

Peer-reviewed publications

- “Temporal focusing for multiphoton imaging of trapped cells,” R. Spesyvtsev, **H. A. Rendall**, M. Chen, F. J. Gunn-Moore, K. Dholakia (In preparation)
- “Enhanced optical manipulation of cells using anti-reflection coated microparticles,” D. Craig, A. McDonald, **H. A. Rendall**, F. J. Gunn-Moore, K. Dholakia. *ACS Photonics* (Submitted)
- “High-throughput optical injection of mammalian cells using a Bessel light beam,” **H. A. Rendall**, R. F. Marchington, B. B. Praveen, G. Bergmann, Y. Arita, A. Heisterkamp, F. J. Gunn-Moore, K. Dholakia. *Lab on a Chip*, vol. 12, pp. 4816-20, Nov. 2012

Conference contributions

Talks

- “High-throughput optical injection of mammalian cells using a non-diffracting beam in a microfluidic platform,” *Frontiers in Ultrafast Optics: Biomedical, Scientific, and Industrial Applications XIII*, SPIE Conference - Photonics West (San Francisco, USA), 2013.

Posters

- “High-throughput optical injection of mammalian cells using a Bessel beam,” *European Optical Society Topical Meeting in Biophotonics* (Aberdeen, Scotland), 2012.
- “High-throughput optical injection of mammalian cells using 2-D hydrodynamic focusing and a non-diffracting beam,” *Lab-on-a-Chip European Congress* (Edinburgh, Scotland), 2012.
- “Waveguide confined Raman spectroscopy for the interrogation of microdroplets,” *5th International Graduate Summer School Biophotonics ‘11* (Ven, Sweden), 2011.

0. PUBLICATIONS

Contents

Declaration	iii
Abstract	v
Acknowledgements	vii
Publications	ix
List of Abbreviations	xv
1 Manipulation and poration of microscopic particles using light	1
1.1 Introduction	1
1.2 Photoporation	2
1.3 Mechanisms for photoporation	3
1.3.1 Photoporation using continuous-wave lasers	3
1.3.2 Optical breakdown using pulsed lasers	4
1.4 Methods of photoporation	8
1.4.1 Targeted single-cell photoporation	8
1.4.2 Indirect photoporation of multiple cells	10
1.5 Optical tweezers for manipulating microscopic particles	13
1.5.1 Trapping in the Mie Regime	13
1.6 Calibrating optical forces	16
1.6.1 Comparison of calibration methods	19
1.7 Combining photoporation with optical trapping	20
1.8 Conclusion	21
1.9 Synopsis	22
2 Microfluidic photoporation using a Bessel beam	25
2.1 Introduction	25
2.2 Microfluidics - fluid flow at the micrometre scale	27
2.2.1 The Reynolds number	29
2.2.2 Flow profile within microfluidic channels	30
2.2.3 The Péclet number	31
2.2.4 1D hydrodynamic focusing	33
2.2.5 2D hydrodynamic focusing	36
2.3 The Bessel beam	39

2.3.1	Bessel beam generation using an annular slit	40
2.3.2	Bessel beam generation using an axicon	42
2.3.3	Bessel beam generation and control using a spatial light modulator	43
2.3.4	‘Self-reconstruction’ properties of the Bessel beam	44
2.3.5	Power distribution	44
2.4	Design of the microfluidic chip	45
2.5	Off-chip 2D hydrodynamic focusing	47
2.5.1	‘Off the shelf’ 2D hydrodynamic focusing	48
2.5.2	Holder for the microfluidic chip	53
2.6	Optical setup - construction of a Bessel beam	53
2.7	Cell culture and sample preparation	55
2.8	Microfluidic optical injection	58
2.9	Results and discussion	59
2.9.1	Attempts at microfluidic optical transfection	62
2.10	Conclusions and future work	63
2.11	Contributions	65
3	Developing a multimodal workstation for photoporation and optical trapping	67
3.1	Introduction	67
3.2	Methods of optical beam steering	68
3.2.1	Acousto-optic deflectors (AODs)	69
3.2.2	Spatial light modulators (SLMs)	71
3.2.3	Comparison between AODs and SLMs for beam steering	74
3.3	Optical setup of a workstation	75
3.4	Pulse Broadening	76
3.5	Aberration correction	79
3.5.1	Zernike polynomials	80
3.5.2	In situ wavefront correction	80
3.6	Developing a user interface	81
3.6.1	Camera Control	83
3.6.2	Shutter Control	84
3.6.3	Creating a ‘point and shoot’ and ‘drag and trap’ interface	86
3.6.4	Calibrating Z positioning	87
3.6.5	Shot modalities	88
3.6.6	Amplitude correction	89
3.6.7	Additional UI elements	92
3.7	Optical Trapping	95
3.8	Photoporation of adherent CHO-K1 cells	100
3.8.1	Sample preparation for optical injection experiments	100
3.8.2	Optical injection results for adherent CHO-K1	102

3.8.3	Attempts at optical transfection	105
3.9	Conclusions and future work	109
3.10	Contributions	112
4	Temporal focusing for multiphoton imaging of optically trapped cells	113
4.1	Introduction	113
4.2	Temporal Focusing	114
4.2.1	Developments and applications of temporal focusing	117
4.3	Experimental Setup	119
4.4	Imaging using temporally focused femtosecond pulses	121
4.4.1	Temporal focusing with different magnifications	121
4.4.2	Imaging of adherent Chinese hamster ovary cells	125
4.4.3	Temporal focusing for imaging optically trapped cells	126
4.5	Conclusions and future work	127
4.6	Contributions	129
5	Summary and future work	131
5.1	Summary	131
5.2	Future work	133
A	Appendix	147
A.1	Contents of supplementary CD	147

CONTENTS

List of Abbreviations

AOD	acousto-optic deflector
CAM	calcein-AM
CHO-K1	Chinese hamster ovary
CW	continuous wave
DNA	deoxyribonucleic acid
FCS	foetal calf serum
FITC	fluorescein isothiocyanate
FPGA	field programmable gate array
fps	frames per second
fs	femtosecond
FWHM	full width at half maximum
GFP	green fluorescent protein
HEK293	human embryonic kidney
HL-60	human promyelocytic leukemia
HWP	half wave plate
ID	inner diameter
NIR	near-infrared
ns	nanosecond
OD	outer diameter
PDMS	polydimethylsiloxane
PEEK	polyether ether ketone
PI	propidium iodide
QPD	quadrant photodiode
rcf	relative centrifugal force
SLM	spatial light modulator
TRITC	tetramethylrhodamine isothiocyanate
UI	user interface
UV	ultraviolet
VI	virtual instrument

1

Manipulation and poration of microscopic particles using light

1.1 Introduction

This thesis addresses optical injection, trapping and imaging of cells in a static suspension or within a microfluidic flow. This chapter looks at two fields where light has been harnessed as a tool for biophotonics. In this chapter photoporation is discussed, which is a technique where the application of light is used to permeabilise biological cells and inject extracellular matter without compromising cell viability. This will be followed by a discussion of the use of light to exert pN forces to manipulate small objects, also known as optical trapping. Chapter 2 details the behaviour of fluids at micron scale where, unlike the macroscopic scale, fluids can be readily manipulated. The properties of these flows, which lie within the low Reynolds regime, are exploited to confine a cell suspension in two dimensions. This is combined with a non-diffracting femtosecond Bessel beam to create a microfluidic platform for high-throughput optical injection. Next in Chapter 3, a multi-modal

workstation for photoporation and optical trapping is designed and built. The aim of the workstation is to provide a platform to study differences in the experimental parameters between photoporation of adherent and non-adherent cells. In the final experimental chapter, Chapter 4, the workstation is modified slightly to combine optical trapping with temporal focusing for the first time. Temporal focusing is an imaging technique where pulsed light is focused temporally at the imaging plane rather than spatially. This allows for scanless multiphoton illumination of a fluorescent sample.

1.2 Photoporation

Photoporation has evolved over the last 30 years as a means of introducing extracellular matter into a cell using only light. The method was first presented by Tsukaoshi et al as a novel method for DNA transfection using a nanosecond pulsed Nd:YAG laser ($\lambda = 355 \text{ nm}$) [1]. Since this first paper a wide range of laser sources have been used, including continuous-wave [2, 3, 4] and pulsed lasers [5, 6] over a wide range of wavelengths. The term originates from the use of light to create a small hole in the cellular membrane through which extra cellular material can pass. Other terms attributed to the technique include optical injection and optical transfection. In this thesis the terms will be defined as outlined in the book chapter “Transfection by optical injection” [7]. Optical injection (optoinjection) describes the injection of membrane-impermeable molecules such as fluorescent dyes into cells. Successful optical injection is usually apparent shortly after the laser dose (of the order of minutes). Optical transfection on the other hand is more specialised and describes the technique of delivering genetic material such as DNA, messenger RNA (mRNA) or small interfering RNA (siRNA) into cells. Optical transfection requires

a biological response from the cell for success whilst injection requires only the physical response by targeting the cellular membrane. The term photoporation is more general and refers to the process of temporarily compromising the cell membrane. It is these definitions which will be used throughout this thesis.

There are a wide variety of methods which can be used to introduce foreign matter through the barrier of the cell membrane and into the cell body. These methods include microinjection [8], electroporation [9], lipofection [10] and viral transfection [11]. Microinjection is a physical process where individual cells are injected using a micropipette. Whilst efficiency is high, the throughput of this method is limited due to its delicate nature. Higher throughput can be obtained using viral or chemical methods or by using electroporation. Each method has its benefits and drawbacks; creating an appropriate viral vector can be time consuming, whilst chemical and electroporation methods can exhibit low cell viability. The best approach for transfection will depend on the end goal of a particular experiment. An alternative to the afore mentioned methods is photoporation which boasts single-cell selectivity within a sterile environment. A number of methods have been developed covering the issue of throughput which will be addressed in Section 1.4 and in the next chapter.

1.3 Mechanisms for photoporation

1.3.1 Photoporation using continuous-wave lasers

The mechanisms involved in photoporation depend on the type of laser source used. These can broadly be split into two categories, continuous wave (CW) lasers and pulsed lasers. When using CW source or long-pulsed (greater than $\sim 10 \mu\text{s}$), the

mechanism is based on linear absorption [12]. This linear absorption leads to localised heating around the laser focus. Since the absorption is linear, it requires using wavelengths that are well absorbed by biological cells such as those in the UV region. Absorption can be improved by using absorbing dyes in the surrounding medium such as phenol-red [2, 3, 13] and by additionally staining the membrane with a non-toxic dye [13]. In these cases a CW argon-ion laser (488 nm) was used. Alternatively, both successful stable and transient transfection have been reported using a violet diode laser (CW, 405 nm) [4, 14]. Violet diode lasers have the benefit of being relatively inexpensive and have a small footprint compared to argon-ion lasers or the pulsed femtosecond lasers. This can potentially enable researchers to use the technique when it would otherwise be cost-prohibitive.

1.3.2 Optical breakdown using pulsed lasers

Pulsed lasers have high peak powers at the laser focus which allow multi-photon absorption to occur. Whilst the mechanisms for membrane permeabilisation are not fully understood, the model proposed by Vogel et al provides an insight into optical breakdown [12]. As biological matter has a high water content, the model considered an amorphous semiconductor based on water with a band gap energy of 6.5 eV. This band gap corresponds to the energy required to promote an electron from the $1b^1$ orbital into an excitation band. Hence for a femtosecond laser tuned to 800 nm, with photon energy of 1.56 eV, it is expected that five photons are required to overcome the band gap and for the creation of a “free electron”. The term “free electron” is used in literature as an abbreviation of “quasi-free electrons” and the term “ionisation” refers to “excitation into the conduction band”. Ionisation

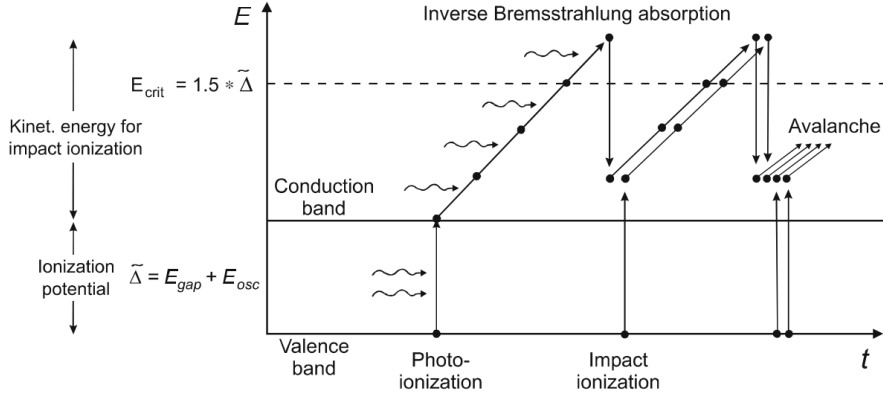


Figure 1.1: Illustration of avalanche ionisation In Vogel’s model of optical breakdown, water is considered an amorphous semiconductor. Multiphoton absorption (photo-ionisation) excites an electron from the valence band to the conduction band. A series of inverse Bremsstrahlung absorption and impact ionisation events lead to an avalanche growth of free electrons. *With kind permission from Springer Science and Business Media [12].*

can occur either through multiphoton absorption (photo-ionisation) or by impact ionisation.

Once a free electron has been created it can absorb photons through a process known as ‘inverse Bremsstrahlung’. After a sufficient number of Bremsstrahlung absorption events, the seed electron has enough energy to produce a second free electron through impact ionisation. These electrons continue to absorb further photons which results in an avalanche growth of free electrons, if the laser irradiation is sufficient to overcome losses. This process is called ‘avalanche ionisation’ or ‘cascade ionisation’ and is depicted in Figure 1.1. Optical breakdown occurs when the laser irradiance is sufficient to produce a free electron density plasma of $\rho_{cr} = 10^{21} \text{ cm}^{-3}$ [12].

The evolution of free-electron density and plasma formation differs greatly between nanosecond and femtosecond lasers. Vogel et al compare this evolution between 6 ns, 1064 nm pulses and 100 fs, 800 nm pulses. Nanosecond pulses produce no free electrons before the irradiance threshold, I_R , because the laser irradiance

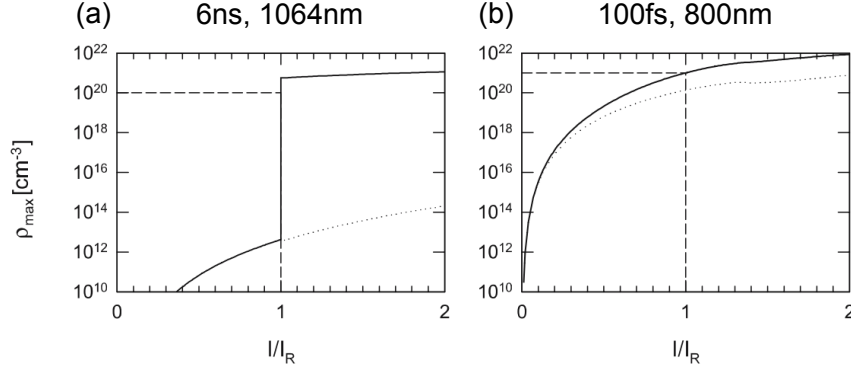


Figure 1.2: Evolution of free electron plasma with irradiance The formation of free electron plasma differs greatly between nanosecond and femtosecond pulses. For nanosecond pulses, avalanche growth of free electrons only occurs once the laser irradiance exceeds I_R , where the free electron density reaches the threshold. This results in a sharp increase in the free electron density. On the other hand, femtosecond pulses can create a low density plasma below the breakdown threshold. *With kind permission from Springer Science and Business Media [12].*

is insufficient to provide the seed electrons through photo-ionisation. It is only once the optical breakdown threshold has been reached that avalanche growth is observed. This occurs very quickly and results in an abrupt increase in the free electron-density, as show in Figure 1.2. Conversely, shorter, femtosecond pulses require much higher irradiance for optical breakdown. The generation of free electrons is dominated by multiphoton absorption rather than by impact ionisation. Due to the greater number of multiphoton absorption events, there are always seed electrons for impact ionisation. Thus an avalanche is initiated at irradiance values below the breakdown threshold and the critical free electron density is approached in a gentler way compared to longer, nanosecond, pulses. Femtosecond optical transfection typically uses high repetition rates (around 80MHz) and pulse energies below the optical breakdown threshold to generate a low-density plasma. Permeabilisation of the cell membrane is the result of a cumulative effect from thousands to several million pulses without destructive effects which occur at higher powers. In contrast, a

nanosecond pulse can cause optical breakdown of the material and generate a large cavitation bubble, often with collateral damage to cells nearest the point of origin (See Section 1.4.2).

Pulse propagation and dispersion of ultrashort pulses

Frequency-dependant effects such as dispersion can be problematic when using ultrashort pulses which have large bandwidths and thus consist of a large number of frequencies. Dispersion can cause broadening of the laser pulse thereby reducing the peak power. This can be of concern for femtosecond photoporation, particularly when using very short pulses (sub 30 fs). Rudhall et al studied the effects of pulse duration, ranging from 17 fs to 143 fs on optical injection of Chinese hamster ovary (CHO-K1) cells [15]. The study required the use of dispersion compensation using Multiphoton Intrapulse Interference Phase Scan (MIIPS) characterisation. Uchugonova et al have also used sub 20 fs femtosecond laser pulses to successfully transfect stem cells [16]. The benefits of these short pulses is that much lower powers can be used (5 mW to 7 mW) [16] compared to the powers when using a more typical 100 fs laser [17].

Dispersion is more easily described by performing a Taylor expansion of the spectral phase around the central frequency, ω_0 [18]:

$$\begin{aligned} \phi(\omega) = \phi(\omega_0) + \phi^{(1)}(\omega_0)(\omega - \omega_0) + \frac{1}{2!}\phi^{(2)}(\omega_0)(\omega - \omega_0)^2 + \frac{1}{3!}\phi^{(3)}(\omega_0)(\omega - \omega_0)^3 \\ + \dots + \frac{1}{n!}\phi^{(n)}(\omega_0)(\omega - \omega_0)^n \quad (1.1) \end{aligned}$$

where $\phi(\omega_0)$ is the spectral phase at ω_0 and $\phi^{(n)}(\omega_0) = \frac{d^n \phi(\omega_0)}{d\omega^n}$. The different derivatives correspond to different orders of dispersion. The first derivative,

$\phi^{(1)}$, is known as the group delay, $\phi^{(2)}$ as the group velocity dispersion (GVD), $\phi^{(3)}$ as third-order dispersion (TOD) and so on [18]. GVD describes the velocity of light for a particular wavelength. As ultrashort pulses contain multiple frequencies, positive GVD results in a broadening in time of the pulse. It is this broadening which can be detrimental for photoporation experiments, particularly when working with ultrashort pulses thereby requiring the use of dispersion compensation techniques [15, 16]. The femtosecond lasers used for photoporation experiments in this thesis have pulse duration of ~ 150 fs. At this pulse duration, dispersion compensation is not required [17].

1.4 Methods of photoporation

1.4.1 Targeted single-cell photoporation

Whilst inexpensive CW laser sources have been used for optical transfection (Section 1.3.1), high repetition rate NIR femtosecond lasers have been the most popular method for optical transfection. Femtosecond transfection of cells was first demonstrated by Tirlapur and König in 2002 [5]. In the experiment, a mode-locked Ti:sapphire laser was used (100 fs pulses, 80 MHz repetition rate) to transfect Chinese hamster ovarian (CHO) and rat-kangaroo kidney epithelial (PtK2) cells with the pEGFP-N1 plasmid. The femtosecond laser was tightly focused on the cell membrane using a high numerical aperture objective lens. This compromised the cell membrane so that the plasmid, in solution in the surrounding medium, could enter the cell. Since this first paper, femtosecond lasers have been used to transfect and/or optically inject a wide range of cells including primary neurons [19], human stem cells [16], embryos (*pomatosceros lamarckii* embryos) [20] and plant cells [21].

Stevenson et al provide a good review of single-cell photoporation [22] and more recently, Antkowiak et al published a paper in Nature Protocols which provides an excellent practical guide [17].

Typically, doses of femtosecond light are delivered to cells individually via a glass coverslip or glass-bottomed dish, as illustrated in Figure 1.3. The membrane-impermeable substance (i.e. a dye or genetic material such as DNA) is simply added to the photoporation medium. Cells are targeted either from above or below. Targeting cells from below decreases the effect of evaporation and the likelihood of contamination during the experiment, as the lid can be kept on the dish. Using a tightly focused Gaussian beam has been the most common method for optical transfection. Targeting the cell membrane is critical for successful poration and so a number of different methods have been employed to increase the chances of correctly targeting the chosen cell and to increase throughput. Using propagation-invariant beams such as the Bessel beam can increase the margin of error compared to a single Gaussian dose [23]. The properties and advantages of Bessel beams will be discussed in more detail in the next chapter. Alternatively when using a Bessel beam is not practical i.e. due to limited laser power, photoporation efficiencies can be improved by using different shot modalities. These can include multiple axially spaced shots or applying a grid of laterally spaced shots over a cell [19]. Manually targeting cells is time-consuming and limits the number of cells which can be dosed during a single experiment. Photoporation systems using holographic elements such as the spatial light modulator (SLM) have been developed to improve ease of use and cell throughput [24, 25]. Microfluidic systems have also been developed which exploit the properties of low Reynolds number flow to guide cells through a femtosecond beam without the need for beam deflection [26, 27]. Chapter 2 will describe one of these microfluidic photoporation systems.

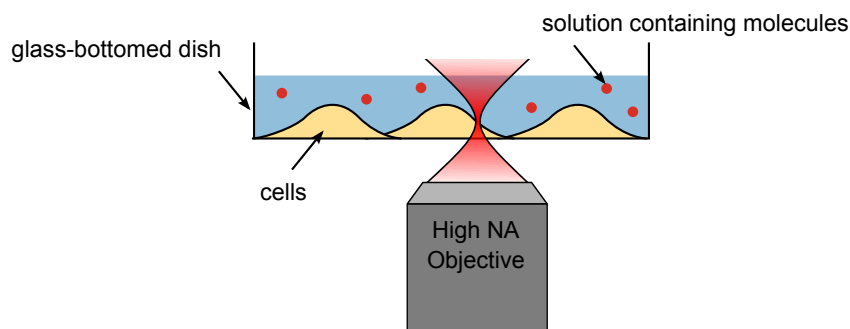


Figure 1.3: Illustration of single cell femtosecond photoporation A typical setup for single cell photoporation uses a tightly focused femtosecond laser which targets the cell membrane. The item which is to be injected (e.g. a membrane-impermeable dye or plasmid DNA) is in solution.

1.4.2 Indirect photoporation of multiple cells

As targeting cells individually can be time consuming, a variety of methods have been developed which target multiple cells simultaneously (Figure 1.4 (a) & (b)). Instead of targeting the cell membrane, Hellman et al used a ns pulsed laser (Nd:YAG $\lambda = 532$ nm) to cause the optical breakdown of water $10 \mu\text{m}$ above the cell culture. The resultant cavitation bubble generated a shear stress on nearby cells. The effect is significant and they categorised the results into three circular zones of cellular injury. In the zone closest to the target, cell lysis and cell detachment occurred. Beyond the cell lysis zone they observed a ring of necrotic cells that did not detach. In the final zone, cells were permeabilised and showed uptake of a dextran whilst maintaining viability. It is this ‘goldilocks’ region which is useful for molecular delivery. Increasing the pulse energy increases the area where cells experience sufficient shear stresses to be permeabilised at the expense of increasing the zone where cells are lysed or are otherwise non-viable.

Further studies by Arita et al use the breakdown of polystyrene and gold nanoparticles in order to gain more control over the resultant cavitation bubble [28, 29]. A range of nanoparticles were optically trapped and then targeted with a ns laser pulse. The lower breakdown threshold of polystyrene and gold compared to water means that ns pulses with significantly less energy could be used. This results in smaller cavitation bubbles being created and offers greater control over cell viability. Optimal parameters for polystyrene particles lead to 30 transfected cells from 10 breakdown events. Gold nanoparticles offered greater control over cavitation size and so powers could be reduced to effectively target a single cell without compromising cell viability.

An alternative to using a tightly focused beam has been to use a weakly focused pulsed laser to simultaneously irradiate several gold nanoparticles which lie on the cell membranes (Figure 1.4.2 (e)). The first plasmonic perforation of living cells was reported by Schomaker et al [32, 35]. These proof of principle experiments demonstrated delivery of fluorescent dyes, siRNA and plasmid DNA. Since then weakly focused ns pulses have been used for gold nanoparticle mediated (GNOME) laser transfection [33, 34, 36, 37]. The precise mechanism is unknown but current understanding implies a combined permeabilisation mechanism which consists of both photochemical and photothermal effects [38].

A variety of methods of using a therapeutic dose of light to permeabilise cell membranes have been discussed over the course of this section. The best approach depends on which parameters are given highest priority; single-cell selectivity, high viability or high throughput. The following section will discuss another application of light; optical tweezers, which are a sensitive tool used to manipulate microscopic objects with pN forces.

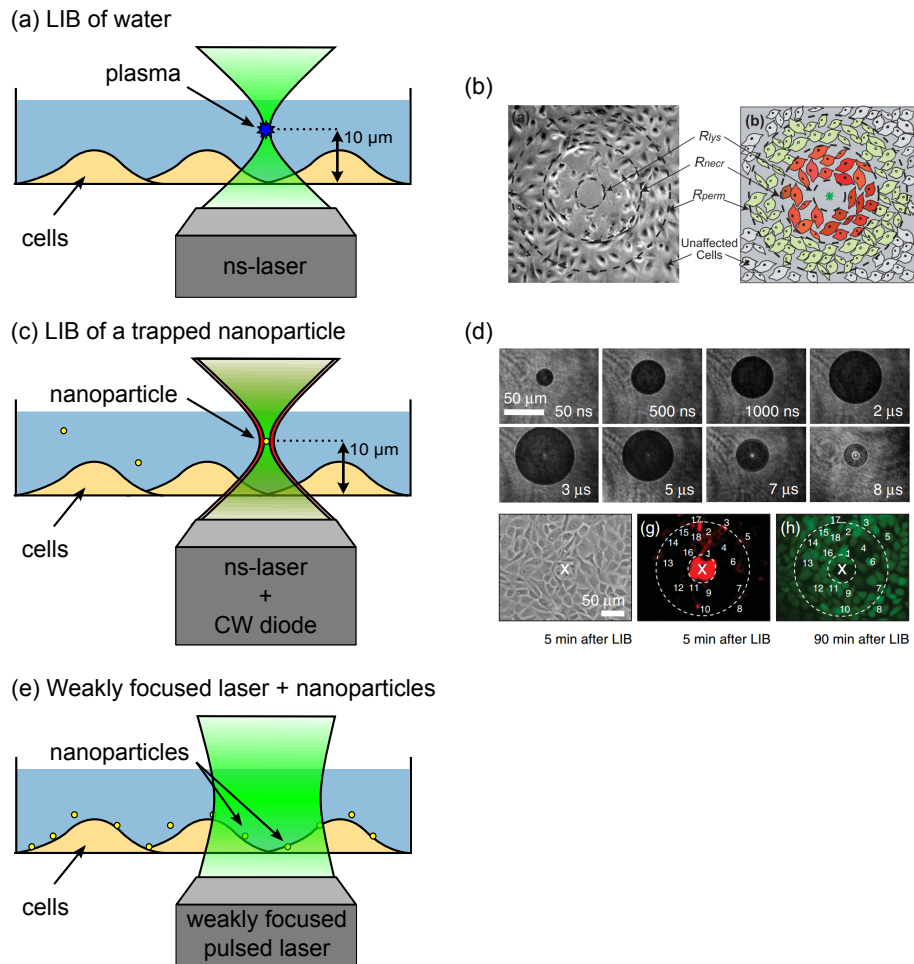


Figure 1.4: Methods of indirect photoporation (a) A ns pulse can be used for laser induced breakdown (LIB) of water to create a cavitation bubble. (b) The cavitation bubble inflicts shear stresses on the cell. Cells which are close to the initiation site are lysed, detach or are non viable (red). Cells beyond this region retain viability and are permeabilised. *Copyright Wiley-VCH Verlag GmbH & Co. KGaA. Reproduced with permission [30].* (c) The size of the cavitation bubble can be reduced by optically breaking down trapped nanoparticles (polystyrene or gold). (d) Example of cells injected with propidium iodide using the breakdown of an optically trapped nanoparticle. *Reprinted figure 1 with permission from Y Arita et al., Phys. Rev. E, 85, 016319 (2012). Copyright 2012 by the American Physical Society [31].* (e) A weakly focused pulsed laser (fs [32] or ps [33, 34]) can be used for gold nanoparticle mediated photoporation

1.5 Optical tweezers for manipulating microscopic particles

Arthur Ashkin first demonstrated controlled manipulation of microscopic particles using laser beams in 1970 [39]. This first experiment used two counter-propagating beams in order to hold particles in the centre where the radiation pressure was balanced. In 1986 Ashkin et al published the first single-beam optical trap which would later be coined “optical tweezers”. Since then optical manipulation has grown hugely as a field with many different applications including sorting [40, 41], measurement of biological forces [42] and even rotation of microscopic particles in vacuum [43].

1.5.1 Trapping in the Mie Regime

Optical trapping depends on the size of the particle. Particles which are much smaller than the wavelength of the trapping laser are said to be in the Rayleigh regime, whilst particles larger than the wavelength of the trapping laser are said to be in the Mie regime. In this thesis the aim is to optically trap cells which are several microns in diameter and hence fall within the Mie regime.

For particles within the Mie regime, a ray-optics approach can be used to model the optical forces. In 1992, Ashkin calculated the forces of a single-beam optical trap [44]. We consider a dielectric particle with a diameter $> \lambda$, a refractive index greater than the surrounding medium and a trapping beam with a Gaussian profile. For a ray-optics approach the incident beam can be decomposed into a series of rays of light each with intensity, direction and polarisation. An illustration of the forces exerted on a particle using a ray-optics approach is shown in Figure 1.6. Each ray

of light incident on the particle at an angle of incident, θ , undergoes a change in momentum. As momentum must be conserved, a force is exerted on the particle.

For light incident on a particle with power P and an angle of incidence θ , it can be shown that the forces acting on the particle are [44]:

$$F_z = F_s = \frac{n_1 P}{c} \left\{ 1 + R \cos 2\theta - \frac{T^2 [\cos(2\theta - 2r) + R \cos 2\theta]}{1 + R^2 + 2R \cos 2r} \right\} \quad (1.2)$$

$$F_Y = F_g = \frac{n_1 P}{c} \left\{ R \sin 2\theta - \frac{T^2 [\sin(2\theta - 2r) + R \sin 2\theta]}{1 + R^2 + 2R \cos 2r} \right\} \quad (1.3)$$

where F_z is the force acting in the direction of the incident ray (a single ray of the scattering force) and F_Y is the component acting perpendicular to the ray (a single ray of the gradient force). R and T are the reflection and transmission coefficients of the surface at angle θ , r is the distance from the beam axis and n_1 is the refractive index of the surrounding medium. This is illustrated in Figure 1.5.

The gradient force is named so due to the gradient of the incoming beam intensity (typically Gaussian in shape). The trapping beam has highest intensity in the centre and so rays in the centre of the beam contribute more toward the net force than rays at the edges of the trapping beam. The net result is a force acting on the particle towards the centre of the trapping beam. This is shown in Figure 1.6 (a). In the case of a highly focused beam (ie using a high NA objective), there is also a gradient force acting in the axial direction which gives rise to 3D trapping. The scattering force, which acts in the direction of propagation, causes slight displacement of the trapped particle in the axial direction from the centre of the focused beam. The scattering force can be used for trapping either by holding a particle against a coverslip or to counter act the drag force in a fluid flow, as is the case in optical chromatography [45].

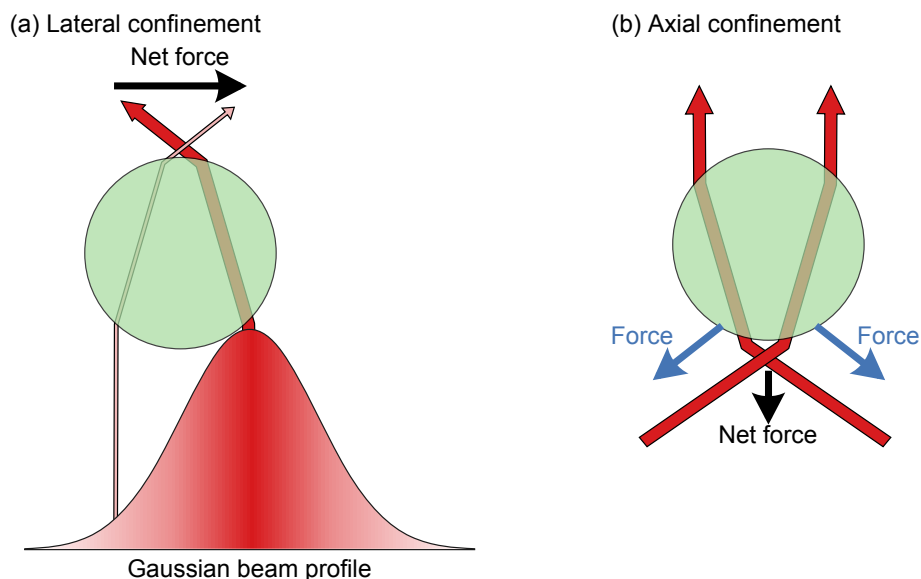


Figure 1.6: Illustration of optical tweezers (a) If the particle is off axis compared to the laser beam (Gaussian profile), the net force will be towards the most intense part at the centre. (b) 3D trapping is obtained by using a tightly focused laser which results in a net force toward the laser focus.

The workstation described in Chapter 3 and Chapter 4 is designed to optically trap cells in 3D. As cells are typically $\sim 20\ \mu\text{m}$ in diameter they fall within the Mie regime and can be trapped in 3D when using a high-NA objective.

1.6 Calibrating optical forces

Precision optical force measurements require well-calibrated optical tweezers. The forces acting on an optically trapped particle are approximate to a Hookean spring with zero rest-length at the centre of the trap. Brownian motion causes small movements of the trapped particle about the centre of the trap. There are three main methods which have been used for calibration which I will now discuss.

The simplest method for calibration is based on the equipartition theorem. The energy of the trapped bead is equal to $\frac{1}{2}k_B T$ whilst the energy stored in the spring

is $\frac{1}{2}k \langle x^2 \rangle$ where k is the spring constant and $\langle x^2 \rangle$ is the variance in the motion of the bead. Equating these two energies yields an expression for the trap stiffness:

$$k = \frac{\langle x^2 \rangle}{k_B T} \quad (1.5)$$

This method does not require a high-bandwidth detector of trap position and so it is possible to implement with a fast CCD camera. Whilst it is simple to implement, an independent temperature measurement must be made and the assumption is made that this remains constant for the duration of the trapping event. Additionally, any drift in the system will affect the calculated variance of particle position.

A more rigorous method based on a particle's Brownian motion is to use a quadrant photodiode (QPD) to detect the bead position and then generate a power spectrum. The power spectrum for a trapped bead is [47]:

$$S_{XX}(f) = \frac{k_B T}{\pi^2 \beta (f_0^2 + f^2)} \quad (1.6)$$

where β is the hydrodynamic drag coefficient ($\beta = 6\pi\eta a$ for Stokes drag coefficient on a bead of radius a in a medium of viscosity η) and f_0 is the rolloff frequency. The trap stiffness can then be calculated using the following [48]:

$$k = 2\pi\beta f_0 \quad (1.7)$$

This method is generally considered the gold standard for trap stiffness measurements. A key requirement is the detector must have a high enough bandwidth in excess of the rolloff frequency to avoid aliasing effects. Trapped particles typically have a rolloff frequency of the order of a few hundred Hz or a few kHz [49], so high-bandwidth detectors like QPDs (placed at the back focal plane) are often used. It is

also important to calibrate the QPD response. The Nature Protocols paper by Lee et al provides a step-by-step guide on building and calibrating an optical tweezer with a QPD [49].

The third method to calibrate an optical trap is based on viscous drag and the particle's escape velocity. If we consider a particle being dragged through a medium at an increasing velocity the drag force will depend on the Stokes drag force. If the bead is close to a boundary such as the glass coverslip, a correction factor (Faxen's law) should be applied to give:

$$F_{drag} = \frac{6\pi\eta av}{\left(1 - \frac{9}{16}\left(\frac{a}{h}\right) + \frac{1}{8}\left(\frac{a}{h}\right)^3 - \frac{45}{256}\left(\frac{a}{h}\right)^4 - \frac{1}{16}\left(\frac{a}{h}\right)^5\right)} \quad (1.8)$$

where v is the velocity h is the distance from the glass coverslip.

By experimentally finding the velocity at which the optically trapped particle falls out of the trap, the escape force (i.e. the trapping force) can be equated to the viscous drag force:

$$F_{drag} \approx F_{escape} \quad (1.9)$$

Hence the Q-value can be obtained:

$$Q = \frac{F_{escape}c}{nP} \approx \frac{F_{drag}c}{nP} \quad (1.10)$$

Another permutation to obtain the escape velocity is to use a stationary particle and a fluid flow. The drag force method is less commonly used as it requires either a motorised stage travelling at a known velocity or a well-controlled fluid flow. Section 2.2 will discuss the properties of microfluidic flows in greater detail.

1.6.1 Comparison of calibration methods

The three methods to calibrate optical traps vary in terms of complexity and the information obtained about the system. Both the equipartition-theorem method and the power-spectrum method rely on observing thermal fluctuations around the centre of the optical trap. Force measurements are often conducted 50 nm to 100 nm from the trap centre and thermal fluctuation calibrations do not give accurate information on the shape of the trapping potential at large displacements from the trap centre [50]. The drag method provides the best way to measure the linearity of the optical trap, provided the viscous drag force can be accurately calculated (Equation 1.8). However, this requires a motorised stage which may not always be possible. Additional benefits of the equipartition-theorem method it is independent of the viscosity of the surrounding medium and does not require the size of the trapped object to be measured.

The power-spectrum method can provide additional information to diagnose problems with an optical trap by observing deviations away from the ideal Lorentzian shape. A sharp rise in the power-spectral density at low frequency is an indication of instrumental drift whilst electrical noise is visible as delta functions [50]. The high bandwidth of the QPD makes it the preferred tool to measure particle position in order to accurately determine the roll-off frequency of a power-spectrum. If the bandwidth of the detector is too low this is observed in the power-spectrum as a decrease of S_{xx} (Equation 1.6) faster than f^{-2} . In Chapter 3 the system does not contain a QPD nor motorised stage so the equipartition-theorem method was used for trap stiffness measurements.

1.7 Combining photoporation with optical trapping

There have been a few studies which make use of optical traps in photoporation experiments. McDougall et al optically injected 100 nm gold nanoparticles into CHO-K1 cells [51]. A NIR femtosecond laser for photoporation and a CW 1064 nm laser for optical tweezing were co-aligned. The gold nanoparticle was optically trapped and held against the cell membrane whilst the cell membrane was irradiated with a 40 ms dose of femtosecond line. Successful injection of the nanoparticles into the cell nucleus was detected using a confocal system.

More recently Waleed et al also combined a NIR fs laser with an optical trapping laser for far larger particles [52]. The focal spots of the trapping and photoporation lasers were separated axially by 1.2 μm . The location of the cell membrane was probed with an optical trapped 1 μm particle using a QPD. The objective was then displaced to place the focus of the fs laser at the cell membrane for the fs dose. Finally the bead was moved into the cell via the hole in the cell membrane. They report successful transfection of MCF-7 cells using a 1 μm plasmid-coated particle. Additionally the effect of exposure time on the size of the punctured hole was reported. Surprisingly hole diameters as large as 3 μm are reported without affecting cell viability [52], which differs greatly from the recommended parameters for viable optical injection [17].

The papers described above both deal with adherent cell cultures and use an optical trap to manipulate a microparticle. Little work has been published on the photoporation of non-adherent cells. Microfluidic systems have achieved optical injection of cells in suspension, as reported by Marchington et al [26] and in Chapter 2.

Transfection of recently trypsinised cells was presented by Praveen et al using the nuclear localisation compound Nupherin-neuron [53]. This study did not use an optical trap. To date, no study has looked at the parameter space and considerations required to optimise photoporation experiments for non-adherent cultures. Chapter 3 in this thesis will outline a system which combines both optical trapping and photoporation in order to enable further investigations on non-adherent cells.

1.8 Conclusion

In this chapter the concept of photoporation was discussed including the mechanisms and methods. The mechanism involved to permeabilise the cell membrane differs depending on the type of laser source. For CW lasers, the effect is linear which leads to localised heating around the laser focus. CW lasers offer a cheap alternative to the pulsed lasers which are more commonly used.

The mechanisms for pulsed lasers can generally be split into two categories, creation of a low-density plasma using a fs laser or optical breakdown of a material using a ns pulse [12]. Fs photoporation is the most popular method for targeting single-cells due to high cell viability. Ns pulses are far more destructive and the optical breakdown of water, which creates a large cavitation bubble. The cavitation bubble exerts shear stresses on nearby cells which is often fatal for those closest to the targeted area [30]. The size of the cavitation bubble can be controlled using the optical breakdown of gold nanoparticles, to the extent that single cells can be targeted [29]. Gold nanoparticles have also been used with a weakly-focused ns laser for photoporation to dose multiple cells simultaneously. The mechanism is not fully understood but is believed to be a combination of photochemical and photothermal

effects [38]. An alternative method for high throughput is to use a microfluidic platform, which will be presented in Chapter 2.

Next, the use of light for optical manipulation was discussed with a focus on single-beam optical trapping of particles in the Mie regime (e.g. cells). Methods of trap calibration were also described. A system combining both photoporation and optical trapping will be developed in Chapter 3, whilst Chapter 4 uses an optical trap to manipulate a trapped cell which is imaged using temporal focusing.

1.9 Synopsis

This thesis will cover different techniques involving light for biophotonic applications; photoporation, optical trapping and imaging. The following three chapters will cover the experimental work which has been conducted.

In Chapter 2, a microfluidic platform is used to improve the throughput of optically injected cells. The properties of low Reynolds fluid flows are exploited to guide cells through a femtosecond Bessel beam which is used for photoporation. The behaviour of fluids at the micron scale and methods of hydrodynamic focusing in 1D and 2D are discussed. Next the generation of the propagation-invariant Bessel beam is discussed prior to developing a system which combines these techniques. Optical injection of two cell lines is demonstrated with throughput increased by up to an order of magnitude compared to other photoporation techniques.

Chapter 3 combines optical trapping and photoporation to create a multimodal workstation. Methods of beam optical beam steering are described with emphasis on the 3D control provided by a SLM. The workstation is presented and a number of considerations are made regarding the user interface. The trapping capabilities of the system are tested and optical injection results of CHO-K1 cells are presented.

In the final experimental chapter, Chapter 4, the workstation outlined in the previous chapter is adapted to combine both optical trapping with temporally focused multiphoton illumination for scanless imaging. The axial resolution of the system was measured prior to imaging both single and a pair of optically trapped cells. The position of the trapped cells was adjusted by using an SLM in order to generate a z-stack of images without adjusting the objective position.

Finally Chapter 5 concludes the results documented in the previous experimental chapters and discusses possible avenues for future work.

1. MANIPULATION AND PORATION OF MICROSCOPIC PARTICLES USING LIGHT

2

Microfluidic photoporation using a Bessel beam

This chapter covers the development of a photoporation system capable of high-throughput, using a microfluidic platform. By exploiting the properties of fluids on the small scale, hydrodynamic focusing is used to concentrate the sample in the region of interest. The channel geometry is designed to include an ‘s’-bend, which allows for ‘end on’ optical access to a 500 μm segment of the channel. When combined with the ‘non-diffracting’ femtosecond Bessel beam, the change to a parallel geometry allows for a greater region of interaction between the Bessel beam and a cell flowing along the channel. This approach means greater flow rates can be used, thus increasing throughput to up to 10 cells per second, an order of magnitude greater than single cell photoporation methods.

2.1 Introduction

Photoporation experiments typically address individually targeted cells growing on a flat substrate such as a glass-bottomed Petri dish. Whilst this approach offers excellent single cell selectivity, the number of cells treated within one experiment is limited by the time taken to position each cell of interest at the focal spot of the photoporating laser. There have been many developments increasing ease of use and throughput of such systems. Novel beam shapes, such as the ‘non-diffracting’

Bessel beam, have alleviated the focusing requirements compared to a tightly focused Gaussian beam as the axial range useful for photoporating is increased [23]. A similar outcome can be achieved by using a spatial light modulator (SLM) to displace a Gaussian beam axially [25]. Furthermore, throughput and ease of use can be improved by combining the properties of the Bessel beam with the positional control of the SLM to create a ‘point-and-shoot’ system [24]. The speed of SLM-based systems depends on the time taken to calculate and generate a new phase mask and the refresh rate of the SLM. For an SLM-based system running with an unassisted raster scan modality, an average photoporating rate of 1 cell per second has been reported. As SLMs are liquid crystal devices, these are inherently slow compared to other methods. These systems can be sped up through the use of a piezo- or galvo-driven mirror for lateral positioning thus negating the requirement for a recalculation of the phase mask. The limited speed of addressing cells in adherent cultures individually renders larger population studies time consuming or impractical. Developing a scanless method for a high-throughput optical approach for injection and/or transfection is potentially useful where other methods perform poorly. A scan-less approach, where the photoporation beam remains in a static position avoids the time lost due to addressing an SLM or the time taken for a motorised stage to move to a new field of view.

By moving away from a static monolayer of cells, other methods of sample manipulation can be incorporated into systems leading to increased sample throughput. Microfluidics provides a platform where small microlitre (μl) volumes of cell suspensions can be readily manipulated using hydrodynamic focusing. Through a combination of femtosecond (fs) pulses at MHz repetition rates with a flow of cells within a microfluidic chip, optical injection at a rate 1 cell per second has been achieved [26]. This first iteration of microfluidic optical injection used a tightly fo-

cused Gaussian beam which was orientated perpendicular to a flow of cells guided in 1-dimension using hydrodynamic focusing. A fast shutter was used to deliver a continuous stream of short, 4 ms doses of 80 MHz fs-pulsed light. At a flow rate of $\sim 1.1 \text{ mm s}^{-1}$, each cell would receive approximately three, 4 ms, doses. A possible limiting factor for throughput arises from the orthogonal geometry. Simply increasing the flow rate of cells reduces the time spent within the photoporation region and the number of received shots.

To increase the potential throughput, a redesign of the geometry is required. Instead of an orthogonal geometry between the fluid flow and the photoporation beam, a parallel approach can be employed. By using a beam with a propagation invariant core, such as a Bessel beam, a parallel geometry allows for a longer interaction region between the cell and the fs-beam. This allows for higher flow rates to be used whilst maintaining an adequate interaction time for successful photoporation.

This chapter first describes some of the properties of fluids flowing at the small scale, when they exhibit laminar flow, and how we can use these properties for controlled confinement of a sample using hydrodynamic focusing. This is followed by a look at the Bessel beam with its ‘non-diffracting’ core and how the quasi-Bessel beam can be generated. These tools are essential to create a microfluidic chip capable of high-throughput optical injection.

2.2 Microfluidics - fluid flow at the micrometre scale

The field of microfluidics concerns fluid flow in channels in the range of a micrometer to hundreds of micrometers in diameter. In this range, the flow behaves in interesting

and unintuitive ways compared to the macroscopic scale. At these small scales, the flow can be described as laminar and moves in linear and predictable paths. This property allows for unique control of small volumes of liquid and particles suspended in these volumes.

The field velocity of a Newtonian fluid can be described by the Navier-Stokes equations [54]:

$$\rho \left(\frac{\partial \mathbf{u}}{\partial t} + \mathbf{u} \cdot \nabla \mathbf{u} \right) = -\nabla p + \eta \nabla^2 \mathbf{u} + \mathbf{f} \quad (2.1)$$

where ρ is the density of the fluid, \mathbf{u} is the fluid velocity, t is time, p is the pressure, η is the fluid viscosity and \mathbf{f} are additional external force densities. Equation 2.1 is essentially Newton's second law with forces per unit volume caused by a pressure gradient ($-\nabla p$) and viscosity ($\eta \nabla^2 \mathbf{u}$). The left hand side gives us a mass per unit volume (density) multiplied by the acceleration of the fluid [55].

In the case where viscous forces dominate over inertial forces, which is typically true in microfluidics, equation 2.1 can be simplified to a linear expression known as the Stokes equation:

$$\nabla p = \eta \nabla^2 \mathbf{u} \quad (2.2)$$

The Stokes equation takes into consideration the constraint that the fluid is incompressible ($\nabla \cdot \mathbf{u} = 0$) and the boundary conditions ($\mathbf{u} = 0$) at the channel walls.

2.2.1 The Reynolds number

There are many dimensionless numbers used to describe properties in microfluidics. These are typically ratios between two dimensions or other properties. The most well-known dimensionless number in the field of microfluidics is the Reynolds number. The Reynolds number is a measure of the ratio between the inertial and viscous forces. It can be shown that this ratio can be expressed as [54]:

$$Re \equiv \frac{\textit{inertial forces}}{\textit{viscous forces}} = \frac{\rho U_0 L_0}{\eta} \quad (2.3)$$

where ρ is the density, η is the fluid viscosity, U_0 is the fluid velocity and L_0 is the characteristic length scale. For a channel of circular cross-section, L_0 is usually defined as the channel diameter. For a rectangular channel, L_0 is equal to the hydraulic diameter and is defined to be:

$$D_h = \frac{4A}{P} \quad (2.4)$$

where A is the cross-section area and P is the cross-section perimeter.

When the Reynolds number for a flow is small, i.e. less than 1, viscous forces dominate over the inertial forces. Hence the non-linear term of the Navier-Stokes equation (Equation 2.1) can be ignored and be described by the simpler Stokes equation (Equation 2.2). The transition between laminar and turbulent flow occurs when the nonlinear inertial term destabilises the flow and leads to turbulence. For a flow through a cylindrical pipe, the transition occurs when the Reynolds number exceeds ~ 2000 [54]. The Reynolds number can thus be used as a guide to whether a flow would be laminar or turbulent. In practice when working with microfluidics,

typically $Re < 1$ and is far away from the transition point between a purely laminar or turbulent flow.

As an example, for a $100\ \mu\text{m}$ by $100\ \mu\text{m}$ channel like the one to be discussed later in this chapter, the characteristic length (using the hydraulic diameter) is $100\ \mu\text{m}$. For a flow driven by a syringe pump at a volumetric rate of Q , the mean flow velocity, \bar{U} , can be calculated using:

$$\bar{U} = \frac{Q}{A} \tag{2.5}$$

Therefore for a microfluidic system running at $240\ \mu\text{l h}^{-1}$ and using $U_0 = \bar{U}$, $Re \approx 0.7$. Thus the flow falls within the low Reynolds regime and the flow can be described as laminar.

2.2.2 Flow profile within microfluidic channels

In order to achieve a consistent laminar flow, microfluidic systems are typically run using a pressure driven flow. This is commonly achieved using either a gravity-driven flow or a syringe pump. In the case of a gravity-driven flow, the relative height between the inlet and outlet reservoirs is adjusted to obtain a steady flow or to stop the flow entirely by equalising the height and thus the pressure. Alternatively, a syringe pump can be used and operated at a programmable volumetric flow rate. These pressure-driven flows do not have a flat flow profile. By imposing the no-slip boundary conditions to the Stokes equation (Equation 2.2), it can be shown that a solution for a rectangular channel can be expressed as [56]:

$$u(x, y) = \frac{4h^2}{\eta\pi^3} \left(-\frac{dp}{dz} \right) \sum_{n=0}^{\infty} \frac{(-1)^n}{(2n+1)^3} \left\{ 1 - \frac{\cosh \left[(2n+1) \frac{\pi x}{h} \right]}{\cosh \left[(2n+1) \frac{\pi w}{2h} \right]} \right\} \cos \left[(2n+1) \frac{\pi y}{h} \right] \quad (2.6)$$

where h is the height of the channel, w is the channel width and x and y are the position within the channel cross-section. For a square channel, i.e. $100 \mu\text{m}$ by $100 \mu\text{m}$ in size, this results in a parabolic shaped profile. This is also known as a Poiseuille velocity profile. The peak velocity lies in the centre of the channel as shown in Figure 2.1. As the ratio between the channel height and width increases the shape of the profile becomes flatter and tends towards a flat velocity profile equal to the mean velocity with a sharp drop in velocity at the boundaries. In order to obtain an entirely flat velocity profile, an alternative method to a pressure-driven flow needs to be employed. Electrokinetic techniques, where the channel walls are fabricated in such a way that an electric charge can be applied, do not require the no-slip boundary conditions of pressure-driven flows. As a result, a uniform velocity flow profile can be created [57]. The microfluidic chip used, described later in this chapter, uses a pressure-driven flow powered by syringe pumps as these provide sufficient control of the flow rate without further complicating the channel design.

2.2.3 The Péclet number

Whilst high- Re fluids mix continuously due to turbulent flows and convection, at low- Re the mixing of two fluid flows occurs only through diffusion. This behaviour can be advantageous or detrimental depending on the application. The lack of turbulent flow allows for precise control over the positioning of a microfluidic sample by using hydrodynamic focusing, a technique where a sample flows alongside buffer

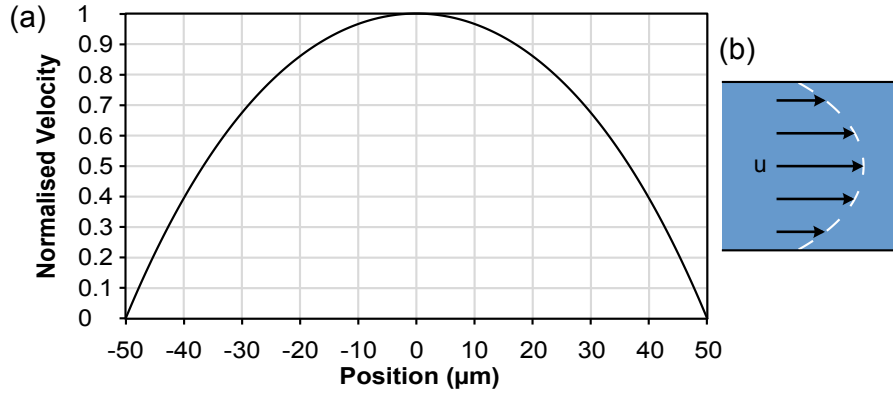


Figure 2.1: Poiseuille velocity flow profile When a flow is driven by a syringe pump a parabolic flow profile is observed. (a) A plot of the flow profile in a $100\ \mu\text{m}$ by $100\ \mu\text{m}$ microfluidic channel in a plane in the middle of the channel. (b) An illustration of the flow velocities, u , within a channel. The peak velocity is observed in the centre and drops off towards the channel walls due to the no-slip boundary condition. The magnitude of the velocities are indicated by the length of the black arrows and the parabolic shape is indicated by the dashed white line.

flows in order to control its position or shape. This technique will be discussed in greater detail in the subsequent sections. The absence of turbulent mixing can however pose a problem where the mixing of reagents is required within the chip. This can be overcome by incorporating micro-structures into the microfluidic channel [58] or by further compartmentalising the reagents into microdroplets [59].

The Péclet number serves as a measurement of the relative importance of convection compared to diffusion. If we consider a T-junction where two fluids flow alongside one another, as illustrated in Figure 2.2; mixing occurs by diffusion. This can be estimated by considering the time taken for the particles or molecules to diffuse across the channel, $\tau_D \approx \frac{w^2}{D}$, relative to the distance travelled downstream during this time, $Z \approx \frac{U_0 w^2}{D}$. The Péclet number can then be defined as the number of channel widths it takes for the two fluid flows to mix [54]:

$$Pe \equiv \frac{U_0 w}{D} \approx \frac{Z}{w} \quad (2.7)$$

where w is the width of the channel, D is the diffusion coefficient and U_0 is the fluid velocity.

The Péclet number can be surprising large. As an example, plasmid DNA such as Mito-DsRed or pCAG-GFP are often used in optical transfection experiments. These plasmids may be of the order of 5 kbp (~ 100 nm) and will have a diffusion constant of around $2 \mu\text{m}^2 \text{s}^{-1}$ in water at room temperature [54]. For a flow rate of $240 \mu\text{l h}^{-1}$ travelling in a $100 \mu\text{m}$ by $100 \mu\text{m}$ channel, which is equal to the total flow rate and the channel dimensions in the experiment outlined in this chapter, the average velocity is $\sim 6700 \mu\text{m s}^{-1}$. This is calculated using Equation 2.5. Therefore using these parameters the calculated Péclet number is 335000 - or alternatively, the fluid would need to travel over 33 m for complete mixing of the plasmid DNA. This should be taken into consideration for microfluidic photoporation experiments when considering how to introduce the molecule or plasmid which is to be injected into the system. Unless the design incorporates a mixing mechanism the molecule or plasmid should be present in all fluid flows rather than in a separate delivery channel.

2.2.4 1D hydrodynamic focusing

As discussed in Section 2.2.2, the velocity flow profile in a pressure-driven microfluidic system has a parabolic shape and so particles or cells travel at a range of speeds depending on their location in the channel relative to the channel walls. For certain applications it can be preferable to guide the sample (e.g. cells) along a single

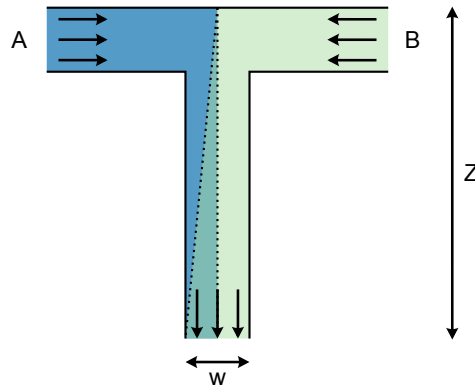


Figure 2.2: Diffusion of two fluid flows An illustration of two fluids mixing with low Reynolds number. When two flows, A and B, meet at a T-junction they mix by diffusion over time as they travel downstream. The direction of fluid flow is indicated by the small black arrows. The area within the dotted lines indicates the region where the fluids have mixed. The Péclet number is a dimensionless number used to describe the distance, Z , it takes for two fluids to mix under these conditions. $Pe \equiv \frac{U_0 w}{D} \approx \frac{Z}{w}$ where U_0 is the fluid velocity, D is the diffusion constant for the particle or molecule, w is the channel width. Quantitative analysis of this mixing was documented by Kamholz et al [60].

trajectory in order to align the sample with an analysis region or to enable sorting with the aid of an additional optical force [41, 61, 62].

There are some discrepancies in the literature for the definition of ‘1D’ and ‘2D’ focusing where in some cases they have been referred to as ‘2D’ and ‘3D’ focusing respectively. This possibly comes down to the dimension of the structures required to achieve sample confinement. In this thesis I will refer to the dimension of hydrodynamic focusing based on the number of degrees of confinement of the sample. This means for ‘1D’ focusing, the sample is confined in either the horizontal or vertical plane whereas ‘2D’ focusing restricts the sample in both directions.

1D hydrodynamic focusing can be achieved using three microfluidic inlet channels, which feed into a single channel. The central channel contains the sample which is to be focused and is sandwiched between two buffer flows. Controlling the relative flow ratios of the inlets allows for controlled confinement on the sample. The benefit of this approach over simply reducing the width of the channel is that the sample is kept clear of the channel walls where cells or particles may stick. There is also a reduced risk of clogging the microfluidic device if the channel is several times larger than the diameter of the sample.

This type of hydrodynamic focusing was employed for the first microfluidic optical injection chip by Marchington et al [26]. Cells were hydrodynamically focused within the centre of the channel and flowed close to the bottom of the channel. In this configuration, a tightly focused Gaussian femtosecond beam could be introduced via the bottom of the chip to target cells as they flow orthogonally to the laser focus. In order to increase the throughput from this design, it is necessary to use a parallel design which will be described in Section 2.4.

2.2.5 2D hydrodynamic focusing

For some purposes 1D hydrodynamic focusing may be insufficient to restrict the location of a sample within the channel. In these cases, 2D hydrodynamic focusing is required. This has been realised with a variety of different channel designs and often require a 3D microfluidic channel structure or high flow speeds. Some examples of 2D hydrodynamic focusing obtained on-chip are shown in Figure 2.3.

A method for surrounding a sample flow was documented by Wolff et al in 2003 with a “smoking chimney” design [63]. As the name suggests, the microfluidic design incorporated a small chimney which allowed for sample insertion within a buffer flow which runs perpendicular to the sample inlet (Figure 2.3 (a)). The chip was created using anisotropic reactive ion etching of a silicon wafer. The sample confinement was controlled by the ratio of buffer to sample flow and provided adequate focusing to be applied to a microfabricated fluorescent-activated cell sorter (μ FACS).

Multilayer polydimethylsiloxane (PDMS) chips have been made which allow for 2D focusing. Sundararajan et al fabricated such a chip which resembles a standard planar 1D design sandwiched between two additional layers with additional sheath flow inlets [64]. A few different designs were simulated in order to improve the symmetry of the focused sample. However, the optimal design proved challenging to fabricate due to only a thin membrane layer separating channels vertically which was susceptible to rupture. To alleviate laborious assembly, Simonnet et al proposed a design that could be created from a single cast of PDMS sealed with a microscope cover glass [65]. The design used a combination of tall and narrow channels with two pairs of shallow channels to focus the sample (Figure 2.3 (b)).

As an alternative to using several sheath flow inlets, microfluidic chips have been designed which have an uneven base such as a row of grooves or chevrons which wrap

the sample flow with the sheath flow [66, 67]. The chevrons or stripes are present on both the top and bottom surfaces of the channel whilst additional inlets can be used to focus the sample into the centre of the channel. These designs have been made using PDMS cast from SU-8 moulds.

On-chip 2D focusing has also been achieved using a planar design, which simplifies the fabrication procedure. Two different designs have been reported by Mao et al in 2007 [68] and Lee et al in 2009 [69]. These are shown in Figure 2.3 (c) and (f) respectively. Both of these designs rely on the use of Dean flow or Dean vortices. The flow in a curved channel is expressed by the Dean number [70]:

$$k = Re\sqrt{\frac{w}{2R}} \quad (2.8)$$

where Re is the Reynolds number, w is the width of the channel and R is the radius of curvature for the curved channel. Dean flow is characterised by two counter-rotating vortices which form in the upper and lower planes of the channel, forcing the sample into the centre. The higher the velocity of the fluid, the greater the Reynolds number and thus the greater the induced Dean flow. Whilst this method provides a solution with a simple microfluidic structure, the high flow rates required are too great for photoporation applications.

A variety of methods for 2D hydrodynamic focusing have been outlined above, which vary in degrees of complexity during either mould fabrication or construction of the chip. In each of these cases the focusing has occurred on-chip. Section 2.4 will discuss a method of 2D focusing off-chip. This approach greatly simplifies the microfluidic chip and so the channel geometry can be designed for optimal optical access.

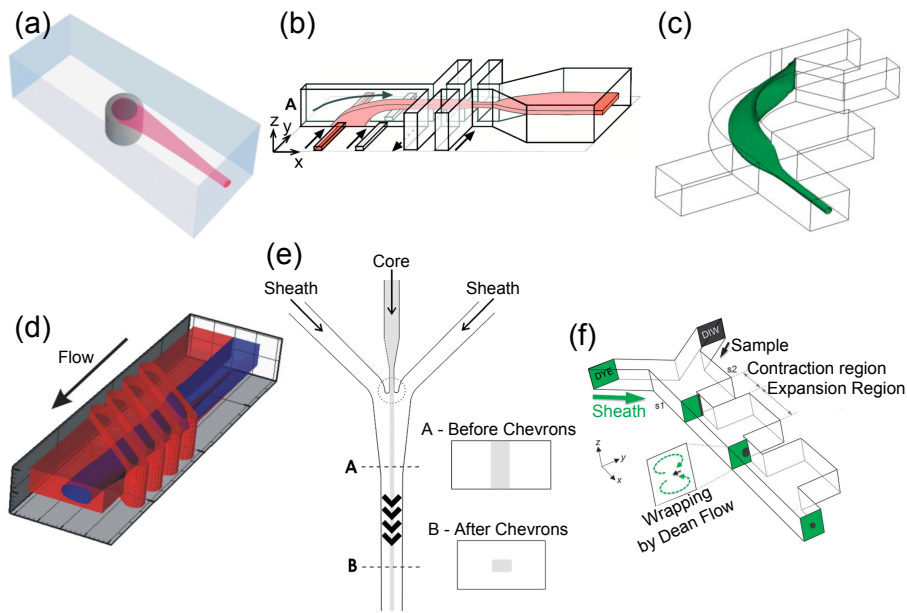


Figure 2.3: Examples of On-chip 2D hydrodynamic focusing (a) Focusing of cells using a “smoking chimney” [63]. (b) Multiple sheath inlets and high aspect ratio channels [65]. (c) Using Dean vortices and 1D focusing [68]. (d) Using striped channels [66] and (e) chevrons in order to wrap the sample in the sheath flow [67]. (f) A planar design using Dean vortices with only a single sheath flow inlet [69]. (a), (c), (d), (e) and (f) adapted from [63, 68, 66, 67, 69] with permission of The Royal Society of Chemistry. (b) Reprinted with permission from Ref [65]. Copyright 2005, AIP Publishing LLC.

2.3 The Bessel beam

The Bessel beam was first proposed by Durnin in 1987 where he noted that particular solutions of the Helmholtz equation yield a ‘non-diffracting beam’ whose intensity profile is invariant along the axis of propagation [71]. The term ‘Bessel beam’ originates from the Bessel function used to describe it. In the case of a zeroth-order Bessel beam, there is a central core surrounded by a series of concentric rings. The central core retains its size as the light propagates and hence the term ‘non-diffracting’ is often used to describe the Bessel beam. It is this central core which garners the most interest for applications of optical manipulation such as trapping [72], sorting [73], imaging [74] and photoporation [23].

The solutions which describe the ideal Bessel beam can be written as:

$$E(r, \phi, z) = A_0 e^{ik_z z} J_n(k_r r) e^{\pm in\phi} \quad (2.9)$$

where $E(r, \phi, z)$ is the electric field of an n th-order Bessel beam, J_n is the n th-order Bessel function, k_z and k_r are components of the wavevectors with $k = \sqrt{k_z^2 + k_r^2} = \frac{2\pi}{\lambda}$, r , ϕ and z are the radial, azimuthal and longitudinal components.

The ideal Bessel beam consists of an infinite number of concentric rings and consequently would contain infinite power. Such a construct is clearly unfeasible experimentally and so compromises are made in regard to the distance over which the central core remains invariant in size.

The Fourier transform of a Bessel beam is a ring [75]. The angle from the axis to the ring can be described as:

$$\theta = \tan^{-1} \frac{k_r}{k_z} \quad (2.10)$$

The size of the core of the Bessel beam can be described as:

$$r_0 = \frac{2.405}{k_r} \quad (2.11)$$

where r_0 is the distance from the centre of the core to the first intensity minimum and the value 2.405 arises from properties of the zeroth-order Bessel function, J_0 .

We now progress onto describing methods of Bessel beam generation, which is best suited for the microfluidic photoporation experiment.

2.3.1 Bessel beam generation using an annular slit

Taking the Fourier transform of a ring will result in a Bessel beam. Durnin et al first experimentally created a Bessel beam by observing the pattern generated by illuminating an annular slit placed one focal length away from a lens [76]. This is illustrated in Figure 2.4.

When an annular slit is illuminated with a plane wave and placed one focal length away from a lens, a zeroth-order Bessel beam is generated. The propagation length of the resultant Bessel beam can be described by the following:

$$Z_{max} \approx \frac{2fR}{D} \quad (2.12)$$

where f is the focal length of the lens, D is the diameter of the annular slit and R is the radius of the lens or the effective radius of the diffraction pattern [77].

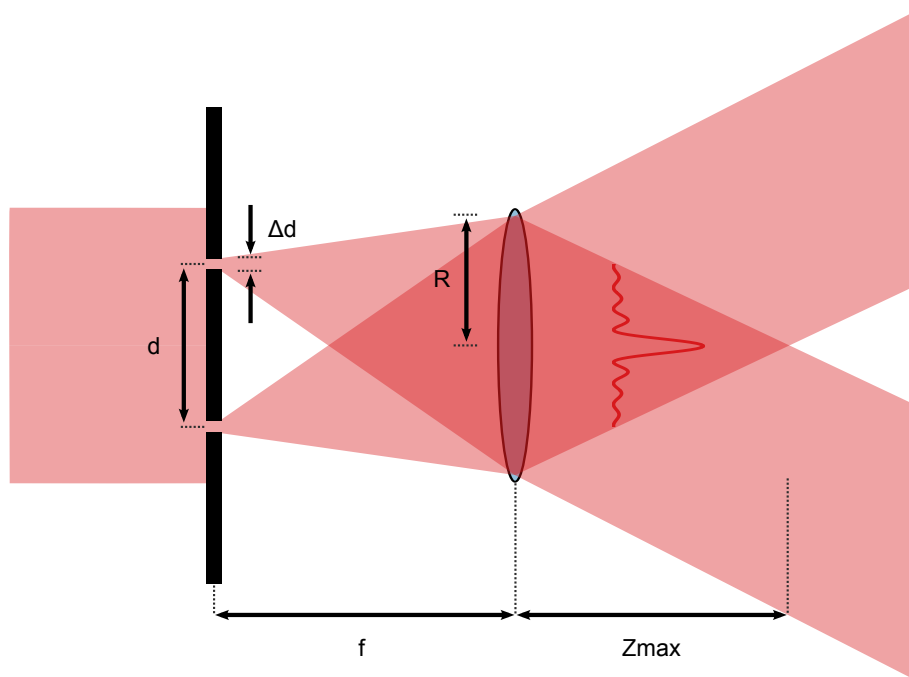


Figure 2.4: Generation of a quasi-Bessel beam using an annular slit When a plane wave is incident on an annular slit, of diameter d and placed at the back focal plane of a lens of focal length f a quasi-Bessel beam is generated. The propagation of the Bessel beam can be described by $Z_{max} \approx \frac{2fR}{D}$, where R is either the radius of the lens or effective radius of the diffraction pattern cast onto the lens [77].

2.3.2 Bessel beam generation using an axicon

Bessel beam generation through Fourier transform of an illuminated annular slit is not the most power-efficient method as the majority of the incoming power is blocked by the centre of the slit and thus does not contribute to the resultant Bessel beam. A more efficient way of generating a Bessel beam without blocking parts of the incoming beam is to use a conical lens - an axicon [78].

The Bessel beam, created as a set of waves, propagate on a cone. This is illustrated in Figure 2.5. The angle of the cone can be derived by Snell's law:

$$\theta = (n_{ax} - 1)\gamma \quad (2.13)$$

where n_{ax} is the refractive index of the axicon and γ is the angle of the axicon. As a result, the propagation length of the Bessel beam can then be found geometrically and described by:

$$Z_{max} = \frac{k}{k_r}\omega_0 \approx \frac{\omega_0}{\theta} \quad (2.14)$$

This is significantly longer than the confocal parameter, b , or depth of focus achieved with a Gaussian beam:

$$b = 2Z_R = \frac{2\pi\omega_0^2}{\lambda} = \frac{2\omega_0}{\text{NA}} \quad (2.15)$$

where Z_R is the Rayleigh range and NA is the numerical aperture.

In Section 2.6 an axicon-generated Bessel beam is used due to the high power efficiency and as there is no requirement to reconfigure the position or shape.

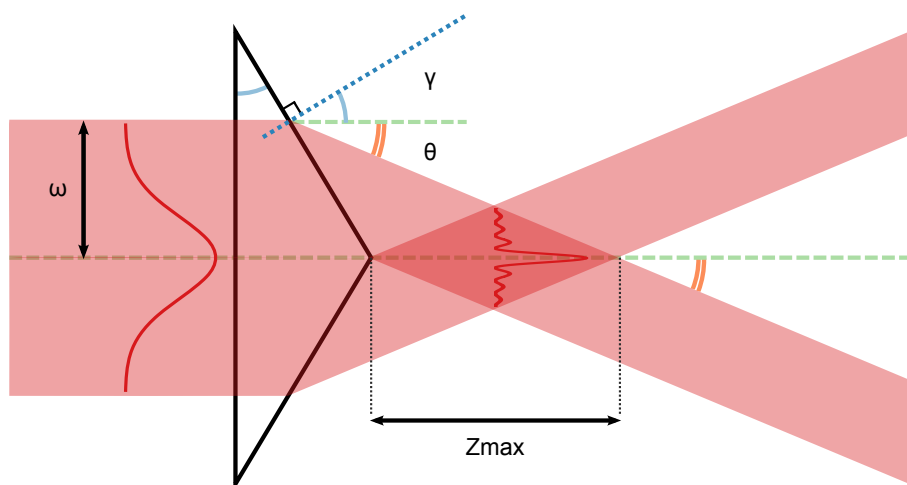


Figure 2.5: Generation of a quasi-Bessel beam using an axicon A method of generating a Bessel beam is by illuminating a conical lens known as an axicon. The generation of the Bessel beam can be considered as the resultant interference between two plane waves. For an axicon of angle γ , the length of propagation can be defined as $Z_{max} \approx \frac{\omega_0}{\theta}$ where ω_0 is the beam width of the incident beam, n_{ax} is the refractive index of the axicon and $\theta \approx \gamma(n_{ax} - 1)$, the angle of the emitted cone which produces a ring in the far field.

2.3.3 Bessel beam generation and control using a spatial light modulator

Bessel beams can also be created using computer-generated holograms on SLMs. Phase-only SLMs allow for control of the phase of light incident on them. By mimicking the phase profile of an axicon, Bessel beams arrays have been generated as demonstrated by Tao et al [79]. Alternatively, SLMs can be used in tandem with an axicon [24]. The benefit of this approach is that the SLM, placed in the far-field of the Bessel beam, can be used to split the original Bessel beam into multiple Bessel beams, change the order of the resultant Bessel beam or perform spatial filtering. As the pattern on the SLM can be readily controlled using a computer, systems incorporating these elements can provide much greater flexibility compared to a single axicon. This has been applied to optical transfection to control the position

of a Bessel beam over a field of view. The use of SLMs for beam control will be discussed in more depth in the next chapter.

2.3.4 ‘Self-reconstruction’ properties of the Bessel beam

In addition to the propagation invariant core, an interesting property of the Bessel beam is its ability of reconstruction or ‘self-healing’ [80, 81]. When an obstruction is placed at the centre of the Bessel beam it casts a shadow in front of it for a distance, before the characteristic Bessel beam profile reforms. The distance it takes for the beam to reconstruct after the obstruction can be calculated by:

$$Z_{min} \approx \frac{ak}{2k_r} \quad (2.16)$$

where a is the width of the obstruction from the centre of the beam. Therefore, an object such as a cell of $a = 10 \mu\text{m}$ obstructing a Bessel beam generated by an axicon with an opening angle (γ) of 5° , will cast a shadow $Z_{min} \approx 115 \mu\text{m}$ long. The Bessel beam described in Section 2.6 and used for the subsequent experiment has a $Z_{max} = 170 \mu\text{m}$. This means that two cells can traverse along the core of the Bessel beam as long as there is sufficient spacing between them. There is therefore an upper limit to the concentration of the cell sample to ensure a cell, which is correctly positioned along the core of the Bessel beam, is photoporated.

2.3.5 Power distribution

A characteristic of Bessel beams is that the energy contained within the central core and each of the concentric rings is approximately the same [77, 82]. Greater propagation length of the central core can be obtained at the expense of power and results in a Bessel beam with a greater number of rings [82]. Lin et al showed ex-

perimentally that the power distribution was approximately equal however reported low central core intensity [77]. They note several possible sources for this including phase-front distortions, distortions in the phase mask used to generate the Bessel beam or intensity modulation. When the power contained within the core is of particular interest, it is more accurate to calculate the percentage of the power within the central spot compared to the whole Bessel beam. This is because it can be difficult to count the outer rings which have a far lower intensity and due the previously mentioned experimental discrepancies. This method was used to calculate the power within the central spot rather than dividing the laser power by the number of rings plus the central core.

2.4 Design of the microfluidic chip

The design of the microfluidic chip must meet three main criteria: (a) the ability to flow biological samples without clogging (b) an inlet and outlet port to insert and collect the photoporated sample and (c) provide an optically flat surface which acts as a window parallel to the flowing fluid. Additionally, the microfluidic chip should provide some degree of sample focusing or have the ability to accept a pre-focused sample.

The key optical requirement is optical access to a section of channel running parallel to the direction of propagation. This requires a microfluidic channel to include a right angle in an ‘S’, ‘L’ or ‘U’ shape as shown in Figure 2.6. Of these designs, the ‘s’-shaped bend is most suitable. It allows for optical access and easy spatial separation of the inlet and outlet. The photoporation region lies at the kink in the ‘S’. As the channel design was in 3 dimensions rather than 2, it was fabricated in quartz glass. Whilst 3-dimensional designs have been constructed using soft

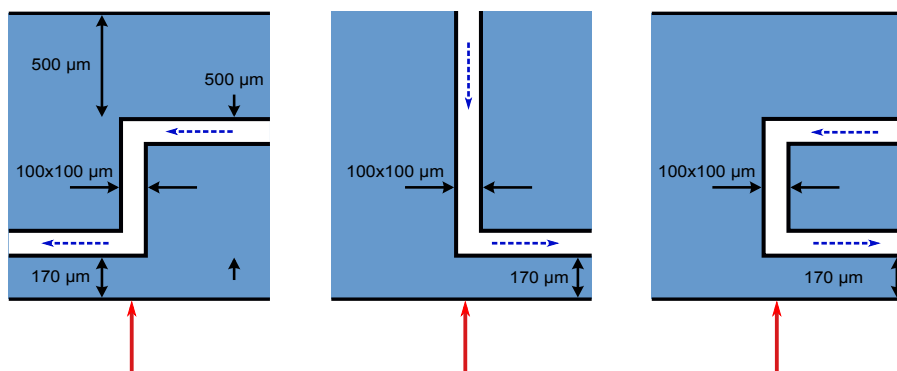


Figure 2.6: Possible channel shapes. Possible permutations of channel geometry which allow for ‘end on’ optical access. The key requirement is a straight segment running perpendicular to the optical window. This requires a right angle in the microfluidic channel. The bottom layer where the Bessel beam enters (red arrow) matches the typical thickness of glass-bottomed Petri dishes used in other photoporation experiments ($170\ \mu\text{m}$). The segment of channel which lies parallel to the propagation axis of the Bessel beam should be long enough to accommodate the full length of the Bessel beam and in this case was designed to be $500\ \mu\text{m}$ in length. The top layer should be thick enough to strengthen the microfluidic chip and to accommodate the indentations at the inlet and outlet used to guide the connected tubing. The microfluidic channel has a square cross-section and is $100\ \mu\text{m}$ by $100\ \mu\text{m}$ in size.

lithography techniques, these can be more difficult to fabricate and align. With this in mind, a reusable 3D quartz-glass chip was fabricated out of house (Translume).

The ‘S’-bend includes a $500\ \mu\text{m}$ segment where a propagation invariant beam can be aligned. The base of the microfluidic chip has been thinned to $170\ \mu\text{m}$, to match the thickness of glass-bottomed Petri dishes used in traditional photoporation experiments. The channel has a square cross-sectional shape and is $100\ \mu\text{m}$ by $100\ \mu\text{m}$ throughout the chip, which is several cell diameters to reduce the chance of clogging. Circular indentations are located at the inlet and outlet of the chip. These are $250\ \mu\text{m}$ deep and are designed to accommodate the diameter of polyether ether ketone (PEEK) tubing (Upchurch 1/16” outer diameter (OD), $100\ \mu\text{m}$ inner diameter (ID)) used to deliver and collect cells from the chip. Nanoports (Upchurch)

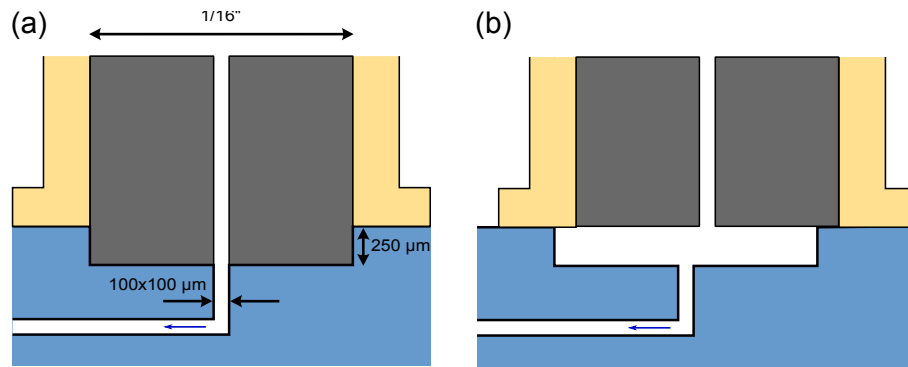


Figure 2.7: Nanoport alignment. Diagram of (a) a well aligned Nanoport compared to (b) a misaligned Nanoport. A misaligned Nanoport leads to an increased chance of trapped bubbles which severely hamper the sample flow and destroy the effect of any hydrodynamic focusing. In order to aid alignment of the Nanoports, a small segment of tubing was inserted into the 250 μm indentation and used to guide the Nanoport whilst fixing it to the chip. This kept the Nanoport concentric to the indentation designed to accommodate the tubing (PEEK, 1/16" OD, 100 μm ID) and this provided a good interface between the tubing and the microfluidic channel.

were fixed to the inlet and outlet to allow external microfluidics whilst minimising dead volume. Small cut-offs of 1/16" OD tubing were used to guide the position of the Nanoports before being permanently fixed to the glass chip. This was necessary as poor placement leads to misalignment of the incoming microfluidic tubing and the channel in the chip. This was particularly critical for the inlet as pre-focused samples were delivered to the chip. Poor alignment or an ill-fitted port destroyed or severely hampered the confinement of the incoming sample or increased the likelihood of trapped air-bubbles. A schematic of the effects of misalignment of the connecting Nanoports on tubing position is shown in Figure 2.7.

2.5 Off-chip 2D hydrodynamic focusing

As the core of the Bessel beam lies in the centre of the channel, a means of confining the sample to this region is required to maximise the interaction between the cells

and the femtosecond beam. In the previous microfluidic optical injection chip, one-dimensional flow focusing was sufficient to guide cells into the focal region of the femtosecond beam as due to the slow flow rates involved, the cells remained ~ 2 microns away from the bottom of the channel. This form of hydrodynamic focusing would be insufficient to guide cells solely in the centre of the channel. In order to meet this requirement, an off-chip approach was employed to localise cells in both the x and y directions.

2.5.1 ‘Off the shelf’ 2D hydrodynamic focusing

There have been several methods for on-chip two-dimensional hydrodynamic focusing reported as described in Section 2.2.5. However, these can prove difficult to fabricate or require strict flow regimes. To maintain the simple microfluidic channel design, an ‘off-chip’ solution was used to provide sample confinement. A three-dimensional nozzle was constructed using ‘off the shelf’ commercially available parts [83]. Its construction was similar to those seen in flow cytometry systems. The core flow, containing the sample, is confined within an outer sheath flow. By adjusting the relative flow rates of these two flows, the degree of sample confinement can be controlled. The velocity of particles can be controlled by changing the combined flow rate. The device was constructed first by fixing a silica capillary (360 μm OD, 50 μm ID) within a microferrule (Upchurch, F-152) using a two-part epoxy. Terray and Hart state the tip of this sample capillary was sharpened to a point. However, we found it sufficient to forego this step and fix the cleaved edge ~ 0.5 mm from the tip of the microferrule. The mounted capillary was then housed within the T-junction from a micro-metering valve assembly (Upchurch, P-446). A cut away view of the flow focusing device is shown in Figure 2.8. A small amount of PDMS

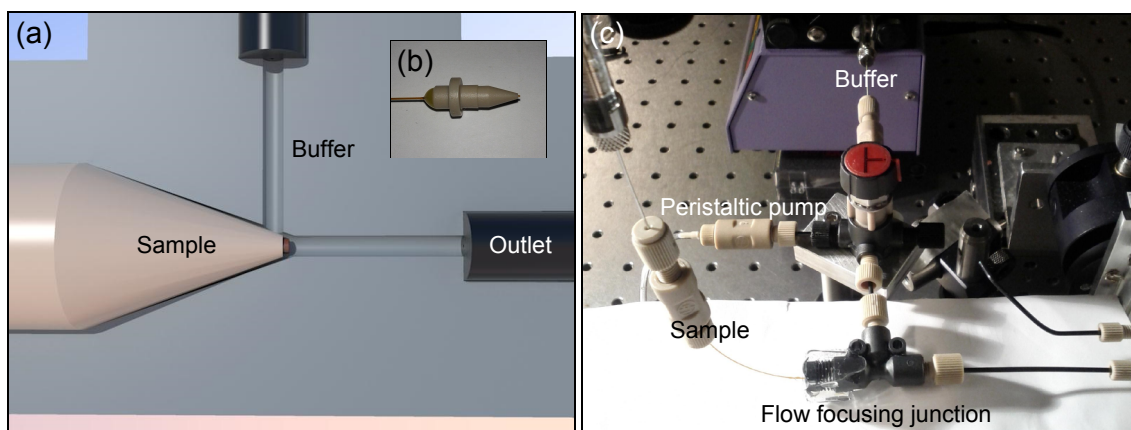


Figure 2.8: Off-chip flow focusing device. (a) A cut away view of the ‘off chip’ flow focusing device (inside the flow focusing junction). The sample is contained with a 50 μm ID capillary and is permanently fixed in position within the microferrule. (b) A photo of a capillary glued into position with the cleaved tip 0.5 mm from the tip of the microferrule. (c) A photo of the flow focusing device integrated into the microfluidic system. The microfluidic chip is out of shot to the right of the flow focusing junction

was used to create a semi-permanent seal of the T-junction. This allowed for the device to be dissembled should a breakage of the sample capillary occur.

The core and sheath flows were controlled using two syringe pumps (Harvard Apparatus, Pico Plus). A 25 μl and a 100 μl gastight syringe (Hamilton) were used with the syringe pumps to control the sample and buffer flow respectively. The accompanying microfluidics included an additional T-junction (Upchurch) to allow a peristaltic pump to be connected to the system for cleaning purposes. A diagram of the overall microfluidic system is shown in Figure 2.9 and is partially shown in Figure 2.8 (c).

The device was initially tested using 4 μm polystyrene beads suspended in water. A range of flow ratios were tested whilst keeping the total flow rate constant. Short segments of video were captured at the photoporation region using a high-speed camera (Fastec Imaging). These videos were analysed in a custom built LabVIEW

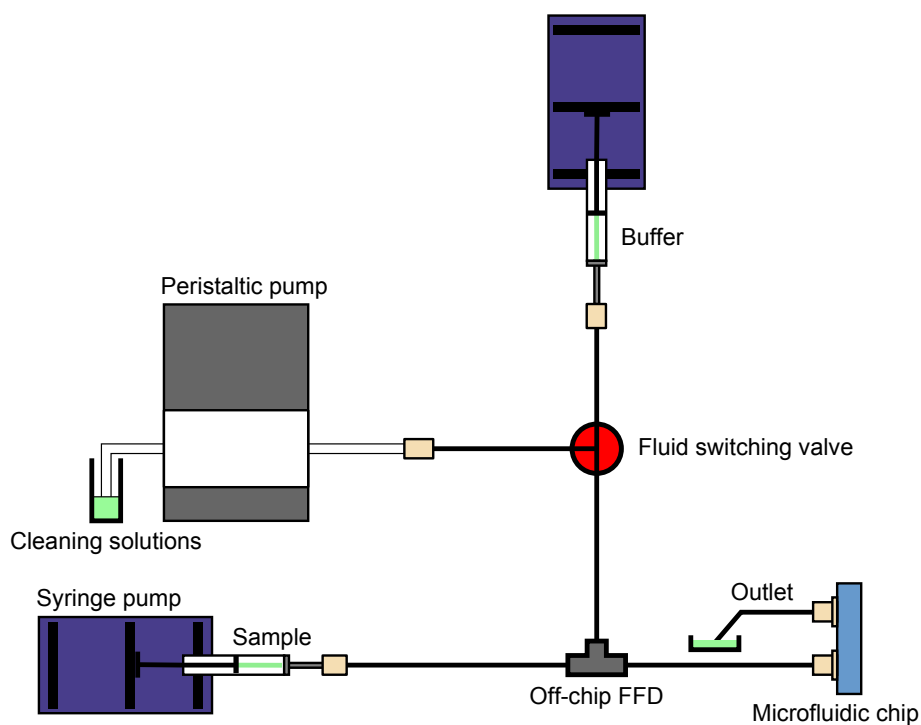


Figure 2.9: Microfluidics for microfluidic optical injection. An overview of the attached microfluidic system. The peristaltic pump was used for cleaning purposes. Two syringe pumps were used to drive the sample and buffer flow. Sample focusing occurred within the flow focusing device (Off-chip FFD) before being loaded onto the microfluidic chip. Cells were collected via the outlet. The additional T-junction (red top) and peristaltic pump were used to flush the system with larger volumes of liquid for cleaning purposes.

virtual instrument (VI) (See Appendix A). The VI analysed each frame of the video sequentially and recorded the position of the centre of mass for each particle. Image processing parameters were chosen such that out of focus beads were not included which could otherwise lead to counting a particle multiple times. This data was then used to calculate the fraction of particles which fell within a defined central region and thus infer the likelihood of a cell flowing through the Bessel beam core. In the absence of a buffer flow, i.e. no hydrodynamic focusing, 20% of the beads flowed within 18 μm of the channel centre. Increasing the ‘buffer to core flow’ to 7:1 showed a significant improvement on sample confinement with 95.6% of particles passing through the same region. This shows the off-chip device was sufficient to focus suspensions despite being located several centimetres away from the photoporation area. It should be noted that it was imperative that good seals were maintained throughout the microfluidic system. Partial clogs or trapped bubbles resulted in the quality of sample focusing plummeting. Additionally poor placement of the sample capillary with respect to the microferrule tip would cause focusing in a non-central region, such as a corner, suggesting that the end of the capillary was touching an inner wall of the T-junction. Fixing the capillary tip close to the microferrule (~ 0.5 mm) avoided this problem. The results from testing the ‘off-chip’ hydrodynamic focusing device at the region of interest are shown in Figure 2.10. As 95.6% of particles fell within 18 μm of the centre and assuming a cell diameter of 20 μm , we infer that the same percentage of cells would pass through the Bessel beam core. Figure 2.10 (d) shows a cell focused to the centre of the channel using the ‘off-chip’ device.

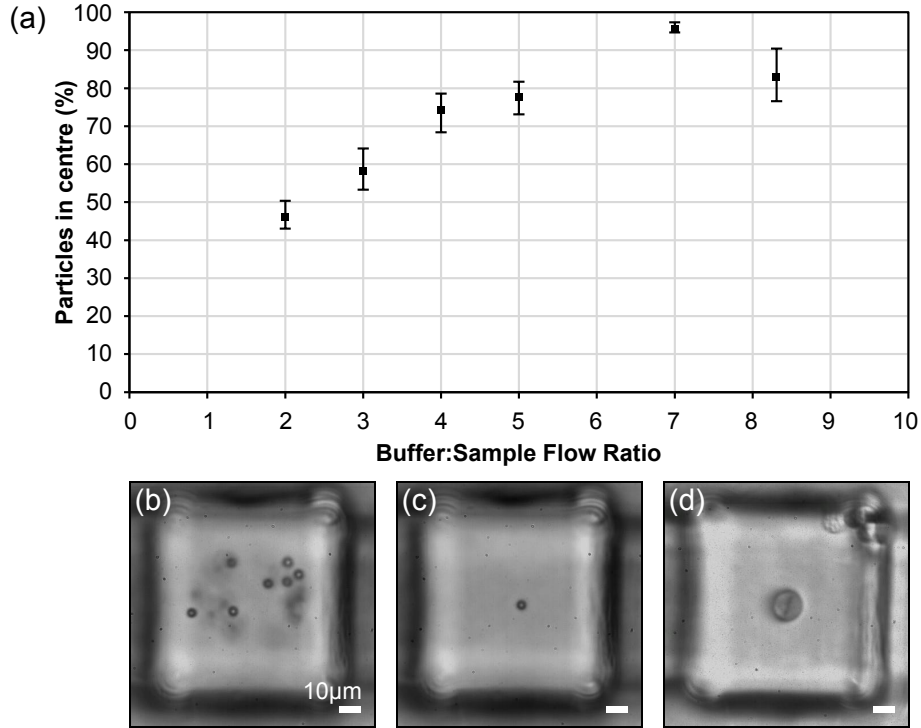


Figure 2.10: Hydrodynamic focusing performance. Data showing the results of the hydrodynamic focusing achieved using the ‘off-chip’ device. A video was recorded of the 100 μm by 100 μm microfluidic channel at the region of photoporation and analysed using LabVIEW (See Appendix A). 4 μm beads were used as test samples. (a) A plot of the percentage of beads passing through the central region (within 18 μm of the centre) of the channel. The total flow rate was kept constant at 240 μl h⁻¹. (b) Beads with no buffer flow, (c) at a buffer to sample flow of 7:1 and (d) focusing a cell sample. As 95.6% of beads fell within 18 μm of the centre of the channel and the central core of the Bessel beam has a diameter ($2r_0$) of 1.9 μm, we estimate that approximately the same percentage of cells, 20 μm in diameter, would pass along the Bessel beam core.

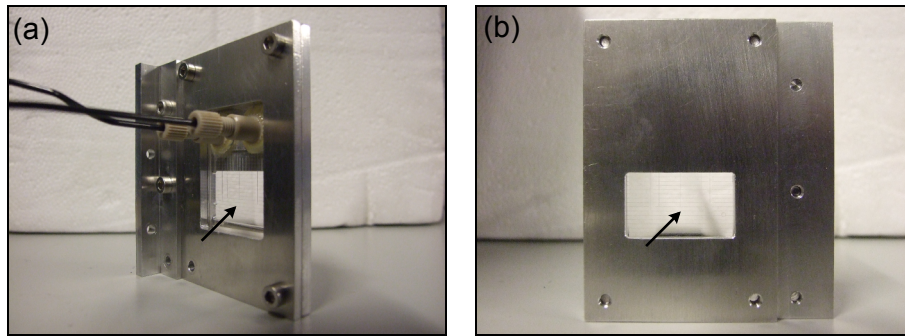


Figure 2.11: Holder for the microfluidic chip (a) Front view of the holder (b) Rear view of the holder. The holder consisted of two aluminium plates with an indent in the lower plate to accommodate the quartz glass chip. An additional piece of aluminium was used to attach the holder to an appropriate positioning stage. Thin layers of PDMS were used to cushion the chip within the holder. The black arrows indicate the location of the ‘s’-bend in the channel.

2.5.2 Holder for the microfluidic chip

The off-chip sample focusing added additional weight onto the microfluidic chip. In order to reduce the chances of the chip breaking a metal holder was designed to hold the chip securely in a vertical position. The holder consisted of two aluminium plates as pictured in Figure 2.11. The bottom plate has an indent to accommodate the microfluidic chip. Access windows were created in both plates to give optical access to the ‘s’-bend in the channel and to the nanoports. The holder provided greater support to the chip compared to clamping the device from the lower part alone. Thin layers of PDMS were inserted between the aluminium plates and the quartz-glass chip to provide additional cushioning.

2.6 Optical setup - construction of a Bessel beam

A ‘non-diffracting’ Bessel beam was used for photoporation. The optical setup is shown in Figure 2.12. The laser used was a mode-locked Ti:sapphire femtosecond

laser (Chameleon, Coherent, Inc. $\lambda = 800$ nm, 140 fs pulse duration at a 80 MHz repetition rate). A half-wave plate was used in conjunction with a polarising beam splitter to attenuate the laser beam to the desired power (1.8 W measured before the first telescope). An axicon with an opening angle of 5° was used to generate the Bessel beam due to the high power efficiency of this method (Section 2.3.2). By using an x8 demagnifying telescope, a Bessel beam was generated with a central core width, $2r_0$, of $1.9 \mu\text{m}$ and a propagation length of $170 \mu\text{m}$. A plot of the measured resultant core radius and peak intensity with distance is shown in Figure 2.13. These measurements were obtained using Matlab (See Appendix A). The core size was chosen to match previous optical transfection experiments which used a Bessel beam [23] and the propagation length was chosen to fit within the 's'-bend of the microfluidic channel (Section 2.4). Initially the power inside the Bessel beam core was estimated by dividing the total power by the number of concentric rings. This was found to be a poor estimation. Subsequently, the fraction of the power contained within the core was calculated by dividing the sum of pixel values inside the core by the sum of the pixels outside of this region. This was found to be 5% after image analysis in ImageJ. An initial power of 1.8 W was used for optical injection experiments. The transmission efficiency was measured to be 80% from before the first telescope to the sample plane. As the core attributed to 5% of the total power at the peak, it is estimated that 72 mW was contained within the Bessel beam core and used for photoporation. This falls within the typical power range for photoporation experiments [17]. As the propagation length increases, the number of visible rings increases and subsequently the fraction of the power contained within the core decreases. Over the propagation length, the power within the core is estimated to fall in line with the powers used in previous optical injection studies such that

cells receive the required laser dose for the creation of a free-electron plasma and subsequent pore formation.

The microfluidic chip was positioned such that the resultant Bessel beam was formed along the channel with the core position in the centre of the flow. This is shown in Figure 2.12 (b) where the two-photon excitation of fluorescein is observed.

2.7 Cell culture and sample preparation

Both human promyelocytic leukemia (HL-60) cells and Chinese hamster ovary (CHO-K1) cells were optically injected using the microfluidic system. These cells lines were chosen to show the system worked for both cells which had been trypsinised (CHO-K1 cells) and with cells which normally grow in suspension (HL-60 cells). CHO-K1 cells were chosen as an adherent cell line as they have often been used in optical injection and transfection studies. The HL-60 cells were cultured in RPMI-1640 (Sigma Aldrich) and CHO-K1 cells were cultured in Modified Eagle's Medium (MEM). In addition to culturing medium, both cell lines were cultured with 10% foetal calf serum (FCS, Globepharm), $20 \mu\text{g ml}^{-1}$ streptomycin and $20 \mu\text{g ml}^{-1}$ penicillin (Sigma Aldrich). These cells were cultured in T25 flasks and incubated in a humidified atmosphere of 5% CO_2 at 37°C . These cells were routinely sub-cultured three times per week.

Propidium iodide (PI) is a nucleic acid stain and is membrane impermeable for living, viable cells. It is taken up by cells where the membrane has been compromised due to cell death or otherwise and subsequently binds to DNA where upon it exhibits a 20-30 fold increase in fluorescence with an emission maximum at 617 nm. It was used to test the optical injection capabilities of the system. As PI uptake is present in both optically injected cells and otherwise compromised cells, calcein-AM

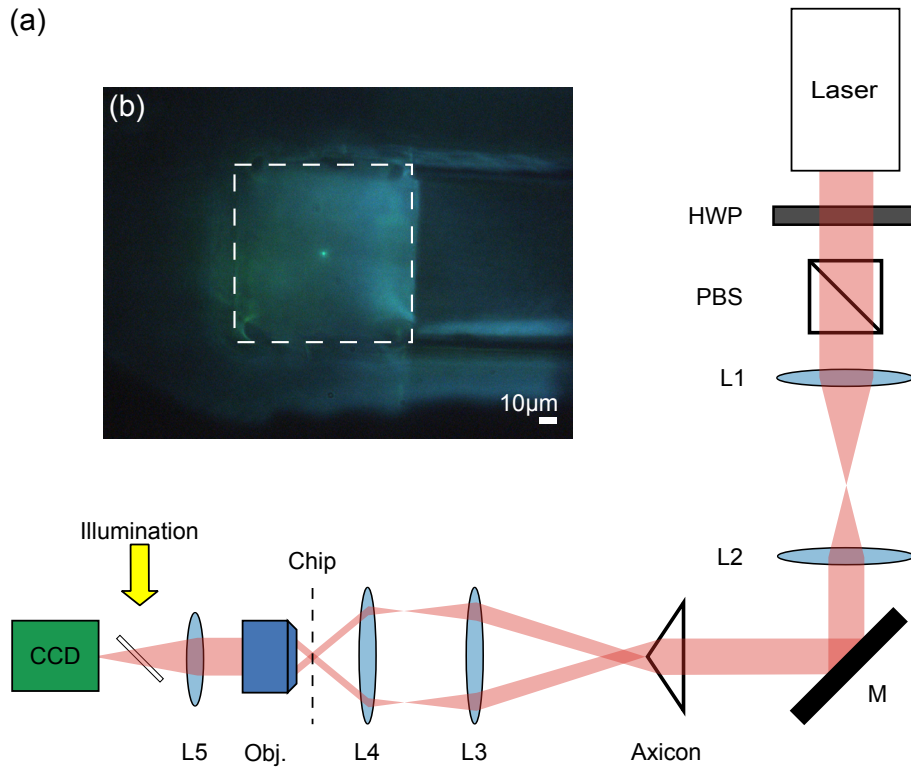


Figure 2.12: Bessel beam setup. (a) A schematic of the optical setup employed in the system. Using a femtosecond laser (Chameleon, Coherent. $\lambda = 800$ nm, 140 fs pulse duration and a 80 MHz repetition rate), the beam is first expanded (L_1 , $f_1 = 200$ mm and L_2 , $f_2 = 100$ mm) before being incident upon an axicon (5° opening angle) to generate a Bessel beam. The Bessel beam is then demagnified by a second telescope consisting of an achromatic doublet (L_3 , $f_3 = 50$ mm) and an aspheric lens (L_4 , $f_4 = 6.24$ mm). The power is attenuated using a combination of a half-wave plate (HWP) and a polarising beamsplitter (PBS). The channel was observed using a Mitutoyo 50x long-working distance objective with an appropriate tube lens (L_5). (b) An end-on view of two-photon induced fluorescence of fluorescein at the Bessel beam core. The white dashed line indicates the location of the channel walls.

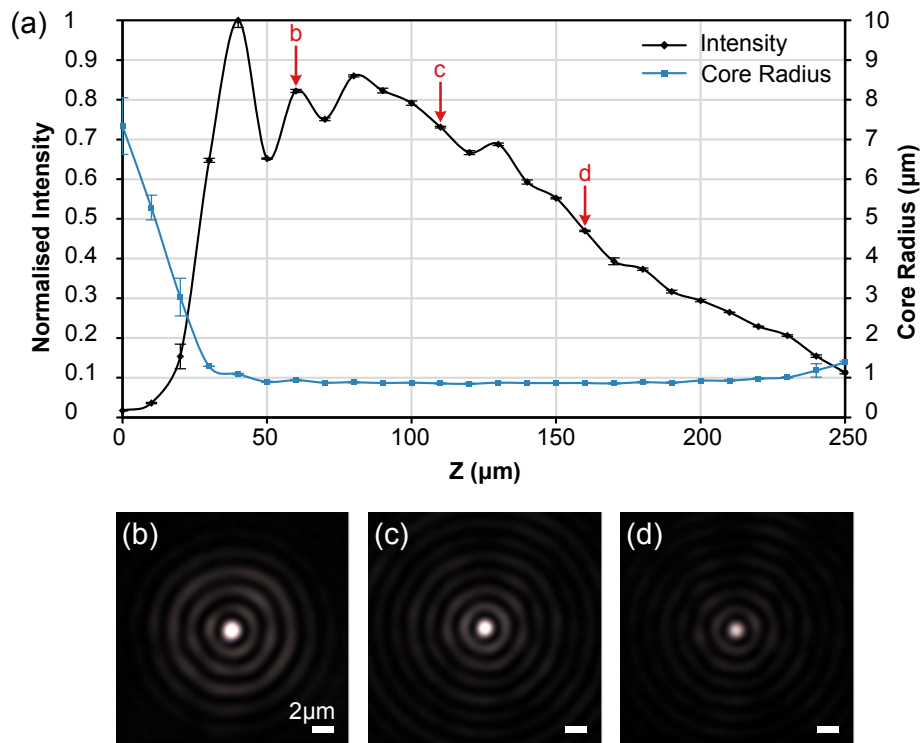


Figure 2.13: Resultant Bessel beam. (a) Plot of the peak intensity and core radius (using the $\frac{1}{e^2}$ intensity criterion) with propagation distance. (b)-(d) Bessel beam profiles at different z positions. Images of the beam were obtained and analysed using Matlab (see Appendix A). The core size remains propagation invariant whilst the peak intensity drops as the Bessel beam propagates. The position of the profiles is indicated by the red arrows and spatially separated by $50 \mu\text{m}$ along the propagation axis. The error bars are the standard error of the mean for 3 data sets which are too small to see for most data points.

(CAM) was used to test cell viability. CAM is a membrane permeable strain which is converted to calcein after acetoxymethyl (AM) ester hydrolysis by intracellular esterases. Viable cells fluoresce with an emission peak at 530 nm whilst the calcein leaks out of dead cells. The microfluidic system was filled with Opti-MEM (Invitrogen) containing the injectant, PI, at a concentration of 1.5 μM . The Opti-MEM was warmed to 37°C before use in the chip to lower the chances of bubble formation.

In the case of HL-60 cells, which grow in suspension, a 100 μl to 400 μl aliquot of cells was taken from the stock culture and placed in a 1.5 ml micro-centrifuge tube. The micro-centrifuge tube was topped up with Opti-MEM and centrifuged in a micro-centrifuge at 500 relative centrifugal force (rcf) for 5 min. The cells were washed in fresh Opti-MEM before being suspended finally in Opti-MEM containing PI (1.5 μM). The cell concentration was measured at this point using a haemocytometer before being loaded into a 25 μl syringe. A typical cell concentration of 1.2×10^6 cells ml^{-1} was used for each run. Two cell culture dishes (FluoroDish, World of Precision Instruments, Inc.) containing 400 μl of Opti-MEM were prepared. 7.5 μl of the final cell suspension was added to one dish for the ‘bench’ control that did not pass through the microfluidic chip. The other dish was used to collect cells from the outlet of the microfluidic system.

2.8 Microfluidic optical injection

Before each experiment, the microfluidic system was flushed with solutions of 5% Decon 90, milli-Q filtered water at 70% ethanol before it was dried with filtered air using the peristaltic pump. The chip and all tubing were filled with Opti-MEM solution containing PI using the peristaltic pump. This pump was then disconnected and replaced with a syringe port and a 100 μl syringe containing additional Opti-

MEM and PI solution for the buffer flow. Care was taken not to introduce air bubbles into the system. Once the sample syringe containing cells was in position, the syringe pumps ran at a fixed rate ($30 \mu\text{l h}^{-1}$ for the sample and $210 \mu\text{l h}^{-1}$ for the buffer flow) and the chip was exposed to the Bessel beam. Typically one minute after starting the syringe pump, cells were visible flowing through the photoporation region of the chip with good localisation in the centre of the channel. A glass-bottomed cell culture dish containing Opti-MEM was used as a collection vessel at the outlet. After a further 15 min, the pumps and laser were turned off.

Once cells had passed through the microfluidic system for 15 min, they were collected and checked for a positive PI signal. The fluorescence of the cells was observed using a mercury lamp with a TRITC filter cube (Nikon). Approximately 200 cells per dish were counted. To check the viability of the cells, CAM was added to each dish at a concentration of $1 \mu\text{M}$. The cells were returned to the incubator for 20 min before checking cell viability using a FITC filter cube (Nikon). It was necessary to assess the percentage of PI positive cells and the percentage of viable cells in two stages because there was a small amount of crosstalk of the calcein fluorescence when using the TRITC filter. This made it very difficult to accurately distinguish PI fluorescence which is quite low for viably optically injected cells. Assessing the number of optically injected cells before incubating the cells with CAM avoids this issue at the expense of the ability to assess specific cells for the presence of both PI and calcein.

2.9 Results and discussion

In addition to a control dish on the bench, experimental runs were conducted in the absence of the Bessel beam to confirm the injection of PI was an optical effect

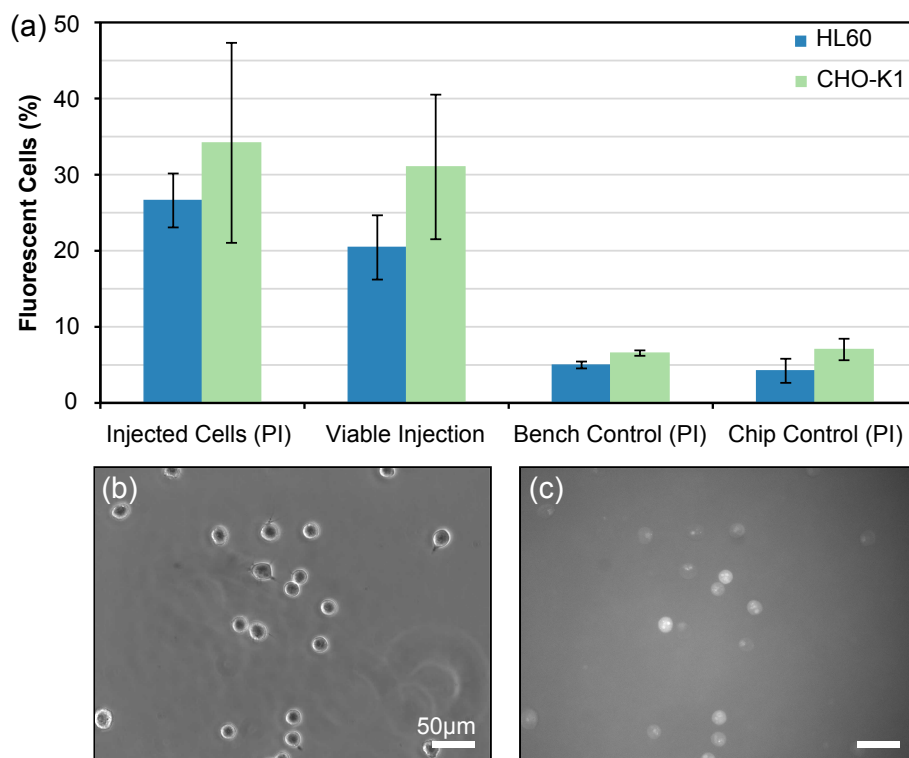


Figure 2.14: Microfluidic photoporation results. (a) Optical injection efficiencies of HL-60 (dark blue) and CHO-K1 (light green) cells with PI. Approximately 200 cells were counted in each sample to obtain the percentage of cells expressing PI. The viability of the cells was then tested using CAM as an additional assay. Viable injection is the injection efficiency corrected for cell viability. The error bars are the standard error of the mean ($N = 10$ for HL-60, $N = 3$ for CHO-K1). (b) Phase contrast image of treated HL-60 cells (c) PI fluorescence observed from the same cells.

rather than due to shear stresses inflicted by the microfluidic system. A graph of the results along with phase contrast and fluorescence images are shown in Figure 2.14.

At a constant flow rate ($30 \mu\text{l h}^{-1}$ for the sample flow and $240 \mu\text{l h}^{-1}$ for the buffer flow), cell velocity was measured to be 7.4 mm s^{-1} in a straight segment of channel using video acquired by a high speed camera (Fastec Imaging). This is less than the theoretical value for the peak velocity in a parabolic flow and a little faster than the average velocity calculated in Section 2.2.3. For the HL-60 cells, typically in the region of 9000 cells were collected which agreed well with the volume of the

sample processed at the measured cell concentration, giving an average throughput of 10 cells s^{-1} . Cell counting was performed via image analysis of pictures taken of the collected cells. The cell velocity corresponds to a potential dose time, the time taken to traverse the propagation length of the Bessel beam, of approximately 23 ms. Under these conditions, $26.6 \pm 3.6\%$ of cells exhibited PI fluorescence compared to $5.0 \pm 0.5\%$ of the bench control. There was no significant difference observed between the bench control and cells which flowed through the chip in the absence of the Bessel beam. This was assessed using an unpaired two-tailed t-test. After correcting for the viability of the cells that flowed through the chip, the viable injection efficiency was found to be $20.4 \pm 4.2\%$.

CHO-K1 cells were also successfully optically injected using this microfluidic device. As the CHO-K1 cells are an adherent cell line, an additional step in cell preparation is required to create a cell suspension. Cells were suspended by adding 1 ml of Trypsin-EDTA and incubated for 5 min. Medium was added to inhibit the trypsin before the cells were rinsed with Opti-MEM through centrifugation as previously described. Under the same microfluidic flow and laser conditions, $34.2 \pm 13.1\%$ injection efficiency was achieved with a corrected efficiency of $31.0 \pm 9.5\%$. It should be noted that the ability to run adherent cell lines in the system relies heavily on the cells remaining largely mono-dispersed over the course of the experiment. Cells which are liable to clump together shortly after cell dissociation would not experience the full effect of the Bessel beam. More crucially, clumps of cells were liable to clog the microfluidic system. This was found to be the case for the adherent cell line, human embryonic kidney (HEK293) cells.

2.9.1 Attempts at microfluidic optical transfection

Attempts were made to obtain optical transfection of HL-60 cells using the microfluidic system. The sample preparation was similar to the method outlined in Section 2.7. Rather than using PI, Mito-DsRed DNA plasmid was added to Opti-MEM at a concentration of $10 \mu\text{g ml}^{-1}$. As with the optical injection experiments, the plasmid was added to the buffer solution in addition to the sample solution to ensure sufficient plasmid surrounded the cells. The microfluidic flow rates were kept consistent with the rates used for optical injection ($30 \mu\text{l h}^{-1}$ for the sample and $210 \mu\text{l h}^{-1}$ for the buffer flow). Transfection requires less power than optical injection and so the power was reduced by to give 65 mW in the core of the Bessel beam at its peak. Cells were passed through the microfluidic chip for 15 min. 2 ml of RMPI-1640 was added to the dish before it was returned to the incubator. A control dish was prepared in the same way with cells added directly to the dish without passing through the microfluidic system. The dishes were observed 24 and 48 hours after the experiment to check for the presence of gene expression. No transfected cells were observed in either the dish of dosed cells or in the control dish.

Troubleshooting optical transfection experiments is difficult when no transfection is observed. As there are multiple parameters which can be changed including the power and the dose time, conducting a wide sweep of the parameter space is not practical due to the quantity of DNA required for each experimental run. It is more sensible to look at the important parameters for transfecting non-adherent and trypsinised cells in a better understood environment, i.e. in a Petri dish. Gaining a better understanding of how these parameters differ compared to transfection of adherent cells will be important if microfluidic optical transfection is to be achieved.

2.10 Conclusions and future work

In this chapter the area of microfluidics was introduced as a platform for manipulating the position of small sample volumes. The laminar behaviour of fluids at low Reynolds numbers allows for excellent control of fluids including particle and cell suspensions by using hydrodynamic focusing. The ‘non-diffracting’ Bessel beam was introduced as a means of increasing the interaction region between cells flowing along the propagation length compared to a Gaussian beam. Next a microfluidic system which combined two-dimensional hydrodynamic focusing of a cell suspension with a fs Bessel light beam for optical injection was presented. The approach uses a counter-propagating geometry where cells flow along the ‘non-diffracting’ core combined with a self-healing property allowing for higher flow speeds to be used whilst maintaining an adequate dose for the optical injection of cell membrane impermeable substances.

The ‘off chip’ approach to focus the cell sample in two-dimensions is straight forward to fabricate as it comprises of readily available commercial parts often used in microfluidic systems. This allows it to be readily implemented within any microfluidic system where ‘off chip’ sample focusing is desired. For this device to function well, a key consideration is the means with which the external microfluidics are connected to the chip. A solution is the use of nanoports in order to align the incoming flow with the channel on the chip. PDMS was used to form a semi-permanent seal around the T-junction of the device. This could be improved by designing an appropriately sized washer between the micro ferrule containing the sample capillary and the screw holding it in position. Clogging can be an issue for trypsinised adherent cells, as was found to be the case for HEK293 cells.

Moving to a parallel geometry between the flow of cells and the photoporation beam allows for greater control of effective dose time. Using a beam shape, such as the Bessel beam used in this design, with a propagation invariant core allows a greater interaction distance between the cell and the fs-beam. In the case of optical injection, this allows for higher flow rates to be used successfully. The dose time can be readily adjusted by altering the velocity of the cells within the microfluidic channel. This is achieved by changing the total flow rate whilst the degree of confinement is controlled via the ratio of buffer flow to sample flow. This could be a needed feature for successful microfluidic optical transfection which has not yet been achieved. The axial profile of the Bessel beam could be improved to lessen the oscillations in intensity by using spatial filtering. These oscillations are the result of an imperfect axicon tip. Using a spatial filter in the Fourier plane to the generated axicon has been shown to improve the quality of the Bessel beam at the expense of some power. Brzobohatý et al studied the spatial intensity distribution of an imperfect axicon both theoretically and experimentally in 2008 [84].

Development of the device outlined in this chapter has led to an order of magnitude increase in throughput compared to the previous orthogonal approach for microfluidic photoporation [26]. As the dose time is governed by the velocity of the cell through the channel, it can be readily changed by altering the overall flow rates whilst maintaining good confinement within the central region of the channel. Such flexibility could be a key feature for future studies including injection of other cell lines with other biologically relevant material. Currently, no optical transfection has been obtained using a microfluidic platform. Due to the large parameter space, it may be beneficial to focus on gaining a better understanding of the differences in parameters for optical transfection of adherent cells compared to non-adherent or

recently trypsinised cells. The next chapter will describe a system designed with this purpose in mind.

Part of this work was published in *Lab on a Chip*, vol. 12, 2012 [27].

2.11 Contributions

H. Rendall conducted all the experiments and data analysis. The microfluidic chip was designed by R. Marchington and fabricated by Translume, Inc. The chip holder was designed by H. Rendall and fabricated by the workshop. H. Rendall and R. Marchington jointly attached the nanoports to the microfluidic chip. This required two people as the chip had to be transported into the clean room. H. Rendall developed the fluidic setup including fabrication and testing of the ‘off-chip’ hydrodynamic focusing. R. Marchington and Y. Arita provided useful discussions in regards to cell preparation.

3

Developing a multimodal workstation for photoporation and optical trapping

This chapter provides a detailed look at the issues arising in the development of a user-friendly workstation for photoporation with optical trapping capabilities. The workstation brings together a number of elements to aid ease of use and is controlled primarily through a custom-made user interface. A femtosecond laser is used for photoporation experiments and a 1070 nm continuous-wave laser is included for optical trapping. The overall aim is to provide a system capable of photoporation of both adherent and non-adherent cells. The ability to trap allows the manipulation and movement of individual non-adherent cells. Studying the parameters required for photoporation of non-adherent cells may give insight on optimising a microfluidic system.

3.1 Introduction

In the previous chapter a microfluidic system was developed to photoporate non-adherent cells and trypsinised adherent cells. Whilst optical injection was achieved, transfection was not obtained using the device. A wide study of the parameter space for optical transfection is impractical due to the relatively large quantity of plasmid DNA required (i.e. over 20 μg for a microfluidic experiment compared to 3 μg for a 35 mm diameter Petri dish) without a better understanding of how it may differ

using adherent cells. A system capable of optical trapping and photoporation allows for new single cell photoporation studies, not possible using the previous microfluidic system.

First we will look at methods of controlling light for lateral positioning which can be readily interfaced with a computer. This will include the phase-only spatial light modulator (SLM) for 3D control of a focused beam. The presence of aberrations in a system can degrade image quality or reduce the ability to produce a diffraction limited focal spot. The latter is of particular importance for femtosecond photoporation as it relies on a multiphoton mechanism. Methods which use SLMs correct these aberrations will be described.

Next the optical design of the workstation will be presented as a system capable of simultaneous optical trapping and femtosecond photoporation. The steps taken to calibrate the system will be discussed both in terms of user interface (UI) elements and how to obtain uniform power over the field of view.

Finally, the system is used for optical injection of adherent Chinese hamster ovary (CHO-K1) cells and attempts are made to achieve optical transfection. These results provide the groundwork for exploration of the parameters required for photoporation of non-adherent cells.

3.2 Methods of optical beam steering

Photoporation experiments can be difficult to execute as they require precise focusing of the femtosecond laser on the cell membrane. As described in Chapter 2, the use of Bessel beams can help relax this focusing requirement due to the propagation invariant core [23]. Power constraints may preclude the use of a Bessel beam, so different shot modalities have been employed to improve transfection efficiency

either by administering multiple shots spaced axially or by employing an array of laterally displaced shots over the targeted cell [19].

The most common method for lateral steering of a focal spot is to place a mirror in the Fourier plane, i.e. conjugate to the back aperture of the objective lens. The displacement of the focal spot is proportional to the angle of reflection from this steering mirror. This angle can be electronically controlled using a piezo- or galvo-driven mirror. The time taken to displace the focal spot is of the order of milliseconds for piezo-driven mirrors and of the order of microseconds for galvo-driven mirrors. However these mirrors only provide lateral displacement of the focal spot and not axial displacement. We will now look at other methods of optical beam steering, both in the context of photoporation experiments and for optical trapping.

3.2.1 Acousto-optic deflectors (AODs)

Fast deflection of an incoming beam, at rates of ~ 10 kHz, can be achieved using a dual-axis acousto-optic deflector (AOD) [85]. A dual-axis AOD consists of two Bragg cells which lie orthogonally to each other. An example is depicted in Figure 3.1 (a). A Bragg cell consists of a crystal, typically tellurium dioxide (TeO_2), with a piezo-transducer on one end and an acoustic absorber on the other. The piezo-transducer is driven by an RF voltage which induces an acoustic wave that travels through the crystal. This acoustic wave induces a refractive index modulation of the crystal. This refractive index modulation means that the crystal acts as a tunable diffraction grating for the incoming laser beam. Optimal transmission into the first order occurs at the Bragg angle which can be described as [86]:

$$\sin\theta_B = \frac{\lambda_0}{2n\Lambda} \quad (3.1)$$

where λ_0 is the wavelength of the incoming light in a vacuum, n is the refractive index of the crystal and Λ is the wavelength of the acoustic wave in the crystal. The wavelength of the acoustic wave depends on the applied RF frequency where $\Lambda = \frac{f}{v}$, f is the RF frequency and v is the acoustic velocity.

By changing the applied RF frequency, the position of the first order beam can readily be changed. The speed at which the position of the beam can be changed has allowed for AODs to be used for time-shared optical trapping [87], where the applied RF frequency cycles through a set of frequencies which correspond to a set of optical trap positions. An example of time-shared optical trapping is shown in Figure 3.1 (b). The applied RF frequency cycles through 9 different frequencies to generate 9 optical traps. Whilst the laser spot is only present at one position at a time, this position changes fast enough that trapped particles do not move significantly whilst the beam is absent.

Generally, AODs only allow for control of the beam in the x and y directions and not axially. Duemani Reddy et al have demonstrated that 3D control of the laser focus can be obtained using a unique arrangement of AODs [88]. This came at the expense of pulse duration which broadened from 200 fs to 1.8 ps. As a result this approach is less suitable for 3D control of a femtosecond photoporation beam. However for optical trapping AODs are versatile devices which can be used to creating multiple traps or customisable optical landscapes [89].

A drawback of AODs is that they do create aberrations in the optical system. These aberrations can be corrected using a SLM, as reported by Čižmár et al [90]. The use of SLMs for aberration correction will be discussed in Section 3.5.

It was initially planned to include an AOD in the system to allow for a broader range of optical trapping experiments. Unfortunately, the digital frequency synthesiser used to drive the AOD failed and was not repaired in time to be included. The

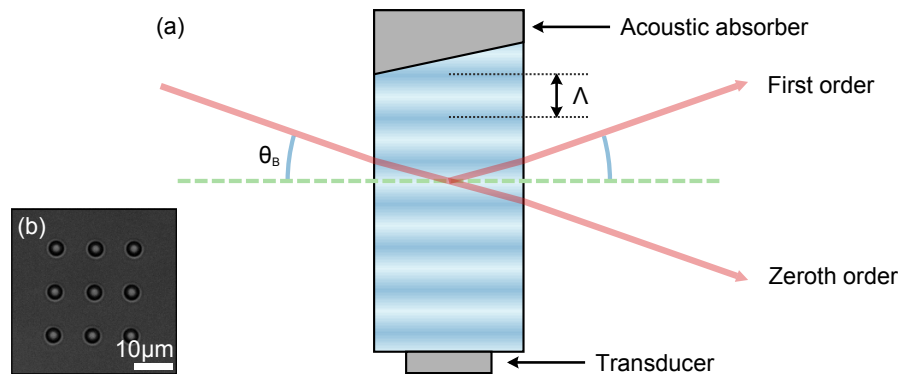


Figure 3.1: Acousto-optic deflector and time-shared optical traps (a) A diagram of a Bragg cell used in AODs. The piezo-transducer is driven by an RF voltage which induces an acoustic wave in the crystal. The acoustic wave causes a refractive-index modulation. As a result, the crystal acts as a tunable diffraction grating for the incoming beam. The response time of the AOD is very fast which allows it to be used to generate arrays of traps by quickly deflecting the beam between trap positions. (b) An example of an array of polystyrene beads trapped using an AOD.

control hardware, including the field programmable gate array (FPGA) card, has been installed for an AOD to be added to the system at a later date.

3.2.2 Spatial light modulators (SLMs)

Phase-only liquid-crystal SLMs are powerful devices for real-time phase modulation of light. Liquid-crystal SLMs use either nematic or ferroelectric liquid crystals. In the case of nematic liquid crystals the number of phase levels is typically equivalent to an 8-bit image - 256 levels covering a phase range of 0 to 2π . Ferroelectric SLMs have only two possible phases corresponding to a phase shift of 0 or π . The limited number of phase levels affects the efficiency of ferroelectric SLMs compared to nematic SLMs. The advantage of ferroelectric SLMs is that they operate at a much higher refresh rate compared to nematic SLMs (of the order of tens of kHz rather than tens of Hz) [91].

SLMs can either be optically-addressed or electrically-addressed. Optically-addressed SLMs are less common and work using a photoconductive effect. They have some key properties which are useful for optical processing. Optically-addressed SLMs can convert incoherent images into coherent images, provide image amplification or be used for wavelength conversion [92].

Electrically-addressed SLMs are more common and consist of a 2D array of pixels. These SLMs are used in the experiments presented in this thesis. An illustration of a nematic liquid crystal SLM is depicted in Figure 3.2. When a voltage is applied to a pixel an electric-field is generated through the nematic liquid crystal. The rod-shaped molecules are polar and thus try to align themselves with the applied electric field. When no electric field is applied these molecules relax to their original orientation. The phase of light incident upon the SLM can therefore be altered by adjusting the voltage applied across the liquid crystal. The SLM is connected to a computer via a control box usually using a convenient DVI connection. As a result these devices can be treated as an additional monitor where 8-bit greyscale images can easily be displayed.

Calculating computer-generated holograms

The fastest way to calculate the appropriate phase hologram for the SLM is to use a superposition of phases associated with the desired elements. Moving the focal spot laterally requires applying a blazed grating to the SLM. The phase is given by [93]:

$$\Phi(u, v) = \frac{2\pi}{\Lambda_x}u + \frac{2\pi}{\Lambda_y}v \pmod{2\pi} \quad (3.2)$$

where Λ_u and Λ_v are the period of the grating in the u and v directions respectively. The grating periods can be expressed as $\Lambda_u = \frac{\lambda f}{\Delta x}$ and $\Lambda_v = \frac{\lambda f}{\Delta y}$ where Δx

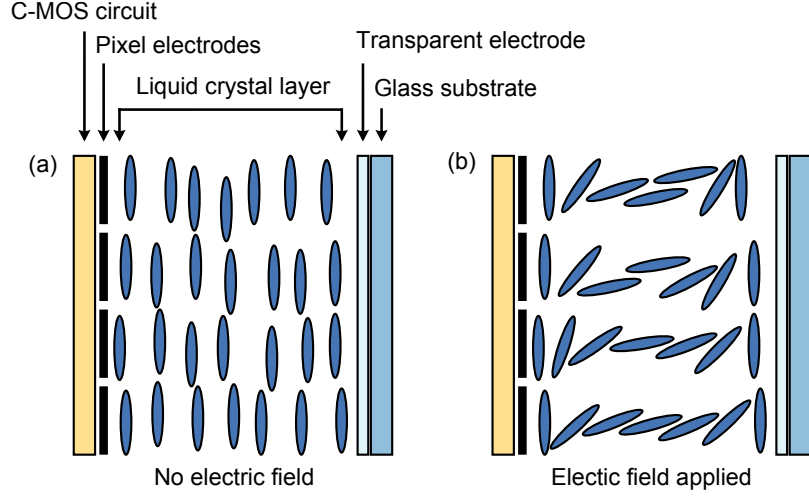


Figure 3.2: Illustration of a liquid crystal spatial light modulator (a) For an SLM using nematic liquid crystals the molecules align roughly parallel to the electrodes in a nematic phase when no voltage is applied. (b) When a voltage is applied across the electrodes the polar liquid crystal molecules align themselves with the generated electric field. Thus the phase of light incident upon the SLM via the glass substrate can be controlled by applying the appropriate voltage to the 2D array of pixels in the device.

and Δy are the desired translation, λ is the wavelength and f depends on the lenses and objective used [91].

In order to displace the focal spot axially a quadratic phase mask, which mimics a Fresnel lens, can be used to shift the focus a distance, Δz . This phase can be expressed by [93]:

$$\Phi(u, v) = \Gamma (u^2 + v^2) \pmod{2\pi} \quad (3.3)$$

where $\Gamma = \frac{\pi \Delta z}{\lambda f^2}$ [91].

The focal spot can be moved both laterally and axially by displaying a linear combination of a blazed grating and Fresnel lens pattern on the SLM:

$$\Phi(u, v) = \frac{2\pi}{\Lambda_x} u + \frac{2\pi}{\Lambda_y} v + \Gamma (u^2 + v^2) \pmod{2\pi} \quad (3.4)$$

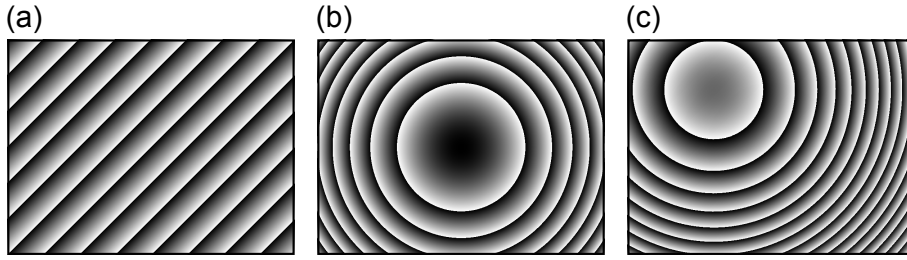


Figure 3.3: Computer-generated holograms Examples of computer-generated holograms which can be displayed on an SLM for beam displacement. (a) By changing the period of a blazed grating the focal spot can be laterally displaced. (b) A Fresnel lens is used for axial displacement of the focal spot (c) A combination of blazed grating and Fresnel lens allows for the position of the focal spot to be controlled in three-dimensions

An example of a blazed grating, Fresnel lens and a combination of these is shown in Figure 3.3.

3.2.3 Comparison between AODs and SLMs for beam steering

Both AODs and SLMs have been widely used for beam steering and the best method depends on the application, as each method has advantages and disadvantages. AODs are more suitable for time-shared optical trapping compared to SLMs, as they can provide time-shared rates of ~ 10 kHz rather than tens of Hz [85, 91]. Trapping multiple particles with an SLM is generally done with multiple simultaneous trapping sites rather than using a time-shared approach. If the position of these traps is to be dynamic then the SLM requires additional computation time to generate the required hologram. Beam steering with an SLM often generates unwanted spots from higher orders (a result from the blazed grating) or other ghost spots (depending on the method used to generate the hologram). Multiple particle trap-

ping is simpler with an AOD as generating multiple traps simply requires rotating through an array of driving frequencies.

For full 3D control of a focal spot, an SLM is the best choice as simply applying adding a Fresnel lens to the hologram controls the axial position. Although a single 2-axis AOD can only deflect the beam in two dimensions, a unique arrangement of multiple AODs has been reported which steered an ultra-fast laser beam in 3D [88]. The pulse duration suffered using this configuration and so therefore an SLM is more suitable to control a fs laser for photoporation.

Regardless of the method used aberrations will be introduced into the system. An SLM can however be used to correct these aberrations as discussed in the previous section. It has been demonstrated that an SLM can be used in tandem with an AOD to correct aberrations [90].

Overall SLMs provide a broader toolset for beam control with the added benefit of their uses for aberration correction. If an experiment prioritises a fast response over other parameters (i.e. trapping several particles in 2D) then an AOD is more suitable, otherwise SLMs provide an adequate response rate for 3D control.

3.3 Optical setup of a workstation

The optical setup for the workstation is depicted in Figure 3.4 and Figure 3.5. The workstation combines two lasers, the fs laser used for photoporation (Mira, Coherent) and a continuous wave (CW) fibre laser for optical trapping (IPG). The fs laser was tuned to 800 nm and had a repetition rate of 80 MHz. The pulse duration was measured to be 150 fs after the first polarising beam splitter using an autocorrelator. The trapping laser is a CW laser operating at 1070 nm. Two spatial light modulators are used to control the position of each focal spot in three dimensions and for

aberration correction. In each optical arm, the lasers are expanded to fill the SLM which lies conjugate to the back aperture of the objective. The beams are combined using a long-pass dichroic mirror which reflects 800 nm whilst transmitting 1070 nm. Each optical arm has a second telescope after the SLM which relays the plane of the SLM to the back aperture which is within a Nikon Eclipse Ti microscope. The beam overfills the back aperture of the objective in each case. A half-wave plate and polarising beam splitter are used to attenuate the laser power whilst the second half-wave plate is used to align the polarisation for maximum efficiency from the SLM. Only the first-order spot generated by the SLM is used for trapping and photoporation. Additional orders are blocked using an iris positioned at the bottom of the periscope leading to the microscope. This iris lies in a conjugate plane to the sample. Two different cameras are attached to the microscope body: a CCD camera (Basler piA640-210gm) is used during experiments and is interfaced within a LabVIEW environment and a cooled CCD camera (Clara, Andor) is used for fluorescence imaging.

3.4 Pulse Broadening

The role of pulse duration and the effect of dispersion on ultrafast pulses were discussed in Chapter 1. For the workstation presented in this chapter the pulse duration of the femtosecond laser was measured to be 150 fs after the first polarising beam-splitter. Between this point and the sample plane the laser pulses pass through four lenses, a second polarising beam splitter, are reflected by a SLM and passes through the microscope objective (Nikon 60x air objective, $NA = 0.8$). The lenses used are made from N-BK7 glass which shows little broadening of femtosecond pulses above 100 fs [94]. The effect of the objective lens on pulse duration was measured previ-

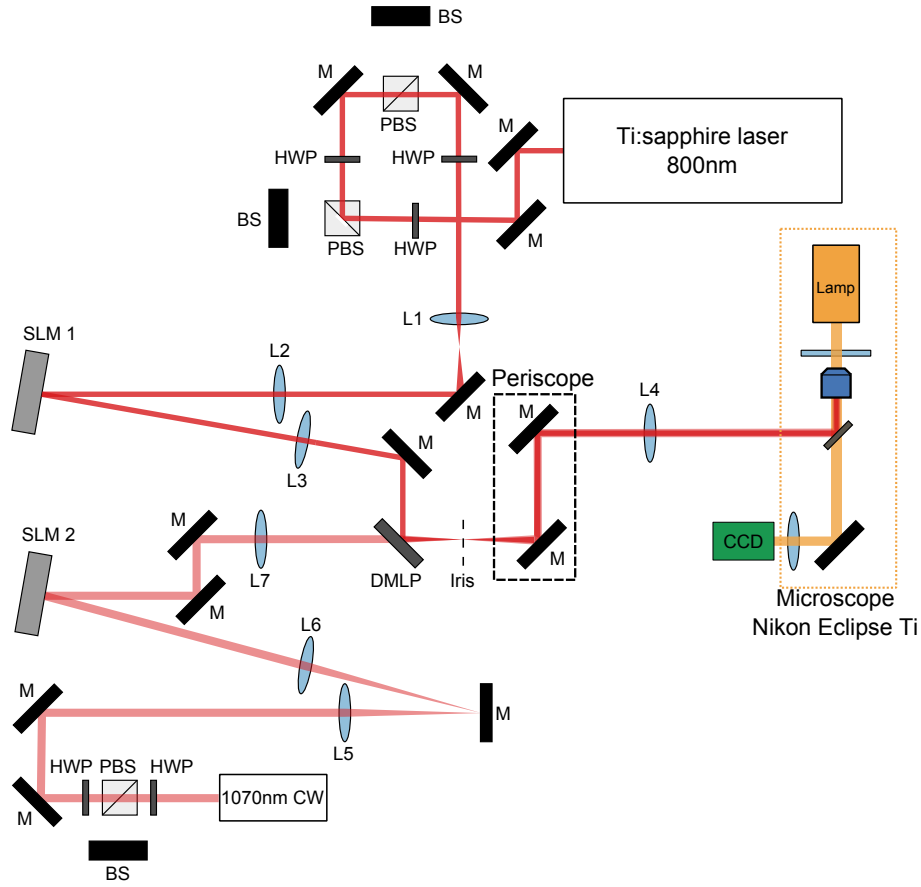


Figure 3.4: Optical setup for a workstation for photoporation and trapping. A Ti:sapphire laser (Mira, Coherent, Inc. $\lambda = 800$ nm, 150 fs pulse duration at a 80 MHz repetition rate) is used for photoporation. The power and polarisation are controlled through a combination of half-wave plates (HWP) and a polarising beam splitter (PBS). The first PBS is used to control power to a separate experiment. The beam is then expanded (L_1 , $f_1 = 50$ mm and L_2 , $f_2 = 400$ mm) to fill the spatial light modulator (SLM1 Hamamatsu X10468-02). The SLM lies on the conjugate plane to the back aperture of the objective. The femtosecond beam is slightly demagnified by a second telescope between the SLM and the back aperture (L_3 , $f_3 = 500$ mm and L_4 , $f_4 = 400$ mm). The trapping arm is similar to the photoporation arm. The beam of a 1070 nm continuous-wave fibre laser (IPG Photonics) is expanded (L_5 , $f_5 = 150$ mm and L_6 , $f_6 = 400$ mm) before the second SLM (SLM2 Hamamatsu X10468-03). The plane of the trapping SLM is relayed by a second telescope consisting of L_7 , $f_7 = 400$ mm and L_4 . The two lasers are combined by a long-pass dichroic mirror (DMLP900). A commercial Nikon microscope is used with an appropriate dichroic to reflect both the 800 nm and 1070 nm lasers to the microscope objective (Either an air (NA = 0.8) or a water immersion (NA = 1.2) Nikon 60x objective).

3. DEVELOPING A MULTIMODAL WORKSTATION FOR PHOTOPORATION AND OPTICAL TRAPPING

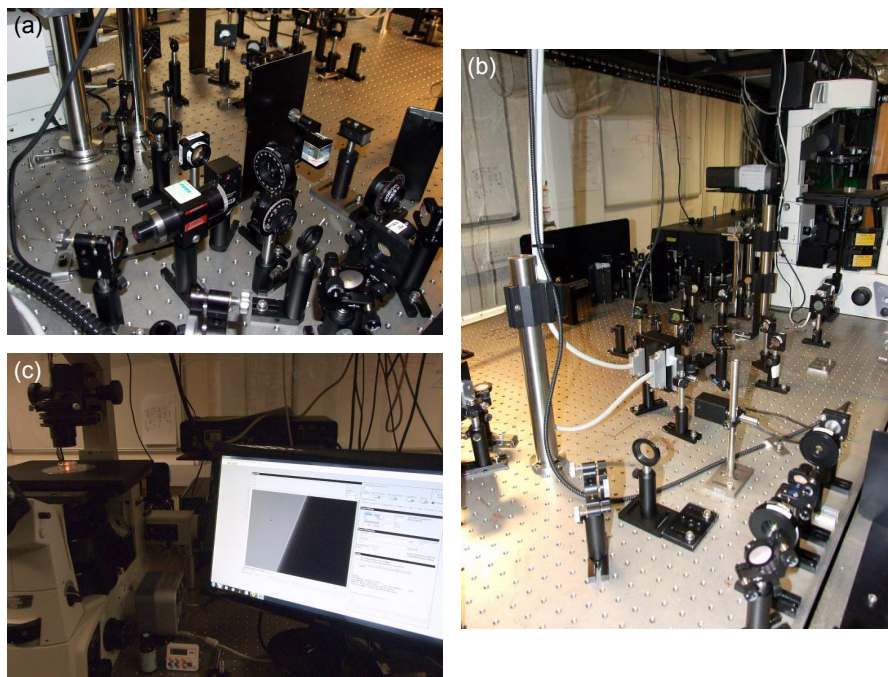


Figure 3.5: Optical setup for a workstation for photoporation and trapping. (a) + (b) Views of the optical setup for the workstation (c) Photo of the microscope and LabVIEW front panel

ously by Patience Mthunzi who measured broadening of the femtosecond laser to be ~ 10 fs leading to a measured pulse duration of ~ 196 fs at the sample plane [95]. The photoporation section of the workstation presented here is very similar to the workstation presented in 2010 [25] and later used for the transfection of single neurons [19] which had initially 200 fs pulses. While the pulse duration at the sample plane has not been explicitly measured, pulse broadening is not expected to affect the system significantly. When working with much shorter pulses (ie less than 20 fs) dispersion has a far greater effect and it is necessary to compensate for this dispersion however this is not required when using 100 fs to 200 fs pulses [17].

3.5 Aberration correction

Optical aberrations are present in all optical systems which cause deviations from ideal imaging. Instead of the ideal diffraction-limited spot, aberrations cause a reduction of the intensity at the focus and a spread of the optical power outside of the focal volume. These aberrations are detrimental to the performance of imaging, optical manipulation and photoporation.

Adaptive optics such as the SLM can be used to eliminate the effect of aberrations in the system. However, the inclusion of the SLM itself can create aberrations due to imperfect flatness of the device.

We will now look at methods to generate a hologram, to display on the SLM, which corrects aberrations in the system. We will make the assumption that these aberrations occur far away from the sample and are time-independent. These assumptions mean that once the hologram has been generated it can readily be applied to correct the aberrations throughout the field of view.

3.5.1 Zernike polynomials

One method of correcting aberrations in a system is to use Zernike polynomials. The Zernike polynomials are a set of polynomials defined on a circle and have been used for a number of decades to correct for atmospheric turbulence [96]. More recently, they have been generated using SLMs for aberration correction [97]. This has led to applications in optical trapping [98], microscopy [99, 100] and photoporation [25]. The different radial orders of Zernike polynomials correspond to different types of aberration such as astigmatism, coma and spherical aberrations. Whilst aberrations can be measured using a wavefront sensor [97], indirect measurement can be conducted for a sensorless approach. In these cases the aberration correction is optimised by applying a set of aberrations (ie different Zernike modes) and then measure an image-quality metric for each aberration. Débarre et al, who used a deformable mirror to correct aberrations within a two-photon microscope, used the mean image intensity as the image-quality metric [100]. This metric reaches a maximum when no aberration is present.

The biophotonics workstation presented in 2010 made use of the first six radial orders (24 modes) for aberration correction [25]. The coefficients for these modes were found through visual inspection rather than a predefined algorithm.

3.5.2 In situ wavefront correction

An alternative approach for aberration correction was published in 2010 by Čižmár et al [101]. The technique is based on orthogonal mode decomposition where the SLM is placed at the Fourier plane to the sample. Instead of using Zernike polynomials the SLM is split into a set of non-overlapping segments (ie. regions 10x10 pixels in size). One segment is kept on throughout the aberration measurement and is used

as a reference mode. The remaining modes are turned on individually to interfere with the reference mode. A number of phase shifts are applied to each mode whilst observing the intensity at a set point in the sample. From this the appropriate phase shift can be determined for constructive interference. After repeating this process for each orthogonal mode, a complete hologram can be generated which corrects the effect of aberrations in the system.

While this method uses a set of point sources on the SLM, the same principle can be applied using an orthogonal set of plane waves. This method is described in the supplementary information of the Nature Photonics paper cited earlier [101]. The benefit of this approach is that the whole SLM is used during the probing process and so a large fraction of the light can be detected. This method was used to correct aberrations in the system using a LabVIEW VI written by Tom Vettenburg. The result from performing aberration correction on the femtosecond beam using a Nikon 60x air objective ($NA = 0.8$) is shown in Figure 3.6. The aberrations were measured whilst focusing on the top reflection of a glass-bottomed dish (170 μm thick). As the subsequent experiments did not include a turbid layer near the sample plane, the generated phase hologram could be generated ahead of time and was valid over the field of view.

3.6 Developing a user interface

The workstation user interface had to controls a variety of instruments including a camera, mechanical shutter and two SLMs. In addition to controlling hardware, additional elements are included to record data or provide information beneficial for photoporation experiments. The following sections describe elements or features which have been incorporated into the main LabVIEW VI (See also Appendix A).

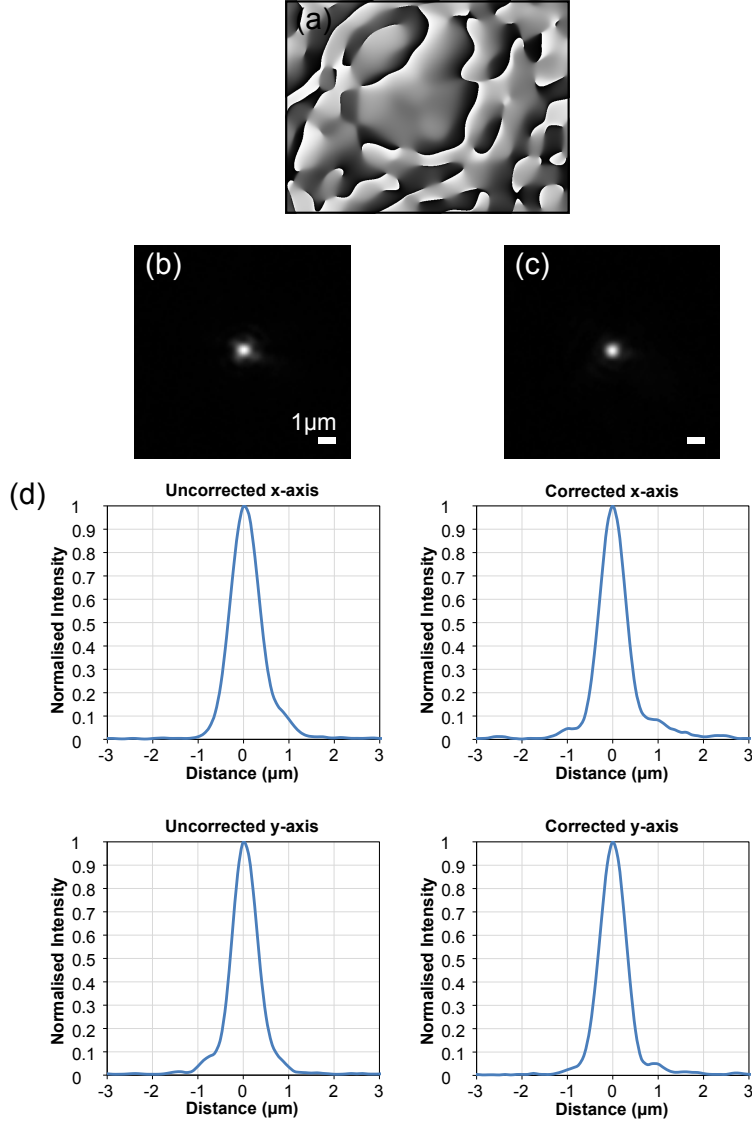


Figure 3.6: Aberration correction using a spatial light modulator (a) The generated phase hologram used for aberration correction. Images of the femtosecond focal spot using a Nikon 60x air objective ($NA = 0.8$) (b) without aberration correction and (c) with aberration correction. (d) Profiles of the uncorrected and corrected beam. The corrected beam profile exhibits better rotational symmetry compared to the uncorrected beam. This is most apparent when comparing the beam diameter (using the $\frac{1}{e^2}$ criterion) along one of the beam diagonals. The beam diameter along the XY diagonal was measured to be $1.25\mu\text{m} \pm 0.13\mu\text{m}$ for the uncorrected beam and $1.00\mu\text{m} \pm 0.13\mu\text{m}$ for the corrected beam.

3.6.1 Camera Control

A fast camera (Basler piA640-210gm) was integrated into the front panel of the workstation. The camera is capable of acquiring at up to 200 Hz enabling the ability to record fast events such as capturing small bubbles during optical injection.

In order to ensure frames were not dropped when lossless time-critical acquisition was required a ‘Producer - Consumer’ architecture was employed within the LabVIEW program. In its simplest form, ‘the producer’ consists of a loop structure that runs quickly and acquires data at a rate faster than can be processed in real-time. The second ‘consumer’ loop has the job of processing data collected by the producer at a slower rate and with lower priority. The benefit of this architecture is that the producer loop is given priority over other processes so frames are not dropped. As the consumer runs with a lower priority, often slower than the producer, it is necessary to buffer or ‘queue’ data to be processed.

During lossless video acquisition (e.g. recording a video of optical injection), when the ‘shoot’ event is triggered, the queue (typically a few hundred frames) is first emptied. The subsequent frames are then added to this queue. Next the ‘consumer’ loop is triggered, which removes elements from the queue and adds them to an .avi file. The rest of the ‘shoot’ event is triggered as usual and is described in subsequent sections. In order to confirm the recorded video is lossless, a corresponding .csv file is generated listing the frame number associated with each frame.

Whilst acquiring video at 200 fps, it is unnecessary and impractical to display each frame live to the user. Without dropping frames, the view on the UI would quickly fall behind the ‘live’ image. To counter this, the displayed image is a preview of the most recent queued element. With previewing, the frame remains in the queue and so is still available to the ‘consumer’ loop when required. The speed of this loop

is controlled using a timed loop and can be set to a more sensible refresh rate such as 30 fps. Video can be acquired from this stream using the ‘lossy’ record setting when longer acquisitions are desired.

A ‘snapshot’ feature has been included to quickly grab and save the latest frame as a single .bmp image file and is triggered by a single click from the user.

3.6.2 Shutter Control

In order to control the femtosecond laser it is necessary to control the time the laser focus remains in one position. This could be controlled either by deflecting it to another position or to physically block the beam. In this experimental setup a phase-only SLM was used for beam control. In theory, the SLM can be updated at video rate (60 Hz) which would correspond to a ramp up and ramp down time of just under 17 ms each way. As a typical dose time may be of the order of 40 ms, relying on the SLM alone to control the laser dose is insufficient. We opted to use a mechanical shutter (Newport 845HP Digital Shutter System) in order to control the femtosecond dose. In order to interface the shutter with the UI, a field programmable gate array (FPGA) card was used. The FPGA card provides far greater control than is required for the currently implemented application, however it provides a potential interface for an AOD to be included in the system at a later date. A simple DAQ card would be sufficient for this application.

The FPGA card requires an interface to be first compiled which then runs on the card continuously. Control signals are sent from within the main VI to the FPGA interface. In essence, the interface provides a high or low voltage signal to open and close the mechanical shutter. The user can define the time the shutter is open, the dose time and set the ramp up delay. The ramp up delay is to account for the

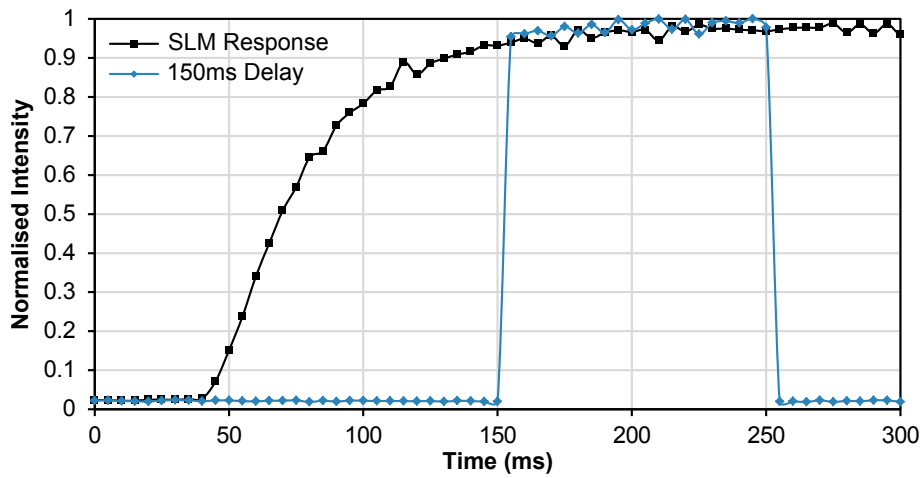


Figure 3.7: SLM response. The graph shows the observed intensity (normalised) as a function of time. The black data points are when no delay between displaying the SLM image and opening the shutter has been included. The blue data points correspond to when a 150 ms delay has been included. When the SLM is initially blank, a noticeable delay of 150 ms is observed before reaching a steady-state position.

relative slowness of the SLM as previously mentioned. In practice, it takes longer for the image to be displayed on the SLM and for the intensity of the spot to reach a steady state. Monitoring the peak intensity of the spot without a delay shows it takes as long as 100 ms to reach a steady state. This was observed by recording lossless video at 200 fps using the CCD camera. In addition to the time taken for the SLM image to be properly displayed, there are some delays within the software. It was found that adding a 150 ms delay between displaying an image on the SLM and issuing a ‘high’ signal to the FPGA card was sufficient. The response time of the mechanical shutter reported by the manufacturer is less than 3 ms. The observed results agree with this, with our limited resolution of 5 ms. A graph of the peak intensity observed with and without a delay between displaying an image on the SLM and opening the shutter is shown in Figure 3.7.

3.6.3 Creating a ‘point and shoot’ and ‘drag and trap’ interface

The lateral position of the laser spot can be readily shifted by adjusting the frequency of the blazed grating on the SLM as previously described. For both the photoporation and trapping lasers we use the first-order spot generated by the blazed grating. Allowing the user to click on a point on the live image and move the first-order spot around the field of view requires a mapping between pixel position and grating frequency. Generating the mapping between pixel position and blazed grating frequency was achieved by measuring the position of the focal spot for several different frequencies. A linear fit was generated from these measurements to give a gradient and intercept. This approach was used to create a fit in both the x and y directions. These values were then incorporated into the main VI.

In the main LabVIEW program user events are generated by chosen interactions between the user and the front panel. Holding ‘shift’ and releasing the left mouse button (LMB) whilst over the live image generates a user event. The mouse position at the time the event was triggered (i.e. the pixel position) is fed through the previously generated mapping to generate the required blazed grating frequencies. The ‘shoot’ event is then subsequently triggered automatically. A red marker is generated on screen at the location where the user generated the event.

Similarly, as user events are generated whilst the user holds ‘control’ and the LMB and drags the mouse cursor across the live image. This controls the location of the trapping beam. Its location is indicated by a coloured square overlay.

3.6.4 Calibrating Z positioning

Positioning the focal spot of the femtosecond beam on the cell membrane is critical for successful photoporation experiments. The position of the focal spot can be adjusted either by moving one of the lenses in the final telescope or by applying a Fresnel lens to the SLM. As both the trapping and photoporation lasers pass through the same final lens, a Fresnel lens on the SLM was used to manipulate the location of the focus. It was necessary to calibrate two parameters in order to translate the power of the Fresnel lens to a shift in Z position: the Z offset and the Z gradient. The offset required to bring the position of the focus to match the imaging plane of the microscope was obtained by focusing on a pen mark on the top surface of a 170 μm cover glass. A video of the laser was then taken whilst displaying a series of Fresnel lenses. Using Matlab code, this video was analysed to determine the strength of the Fresnel lens required to bring the beam into focus. Figure 3.8 plots the peak pixel intensity versus the strength of the Fresnel lens. The units are arbitrary as the amplitude of the Fresnel lens depends on the size of the SLM. Here, a negative Fresnel lens is required to bring the laser focus closer and match the imaging plane.

Calibrating the gradient to map the strength of the Fresnel lens to a Z-shift in microns was trickier to implement. The Nikon Eclipse Ti microscope used in these experiments did not have motorised z-positioning or a digital readout. In order to obtain a reasonable mapping between the manual fine focus and the Fresnel lens, several static images were taken moving the manual fine focus in increments of 1 μm . A video was taken from the starting position which cycled through a series of Fresnel lenses. The value of the Fresnel lens which best matched each image acquired using the fine focus were evaluated. This was achieved by comparing each fine focal image to each Fresnel lens value. Two images can be compared by multiplying their

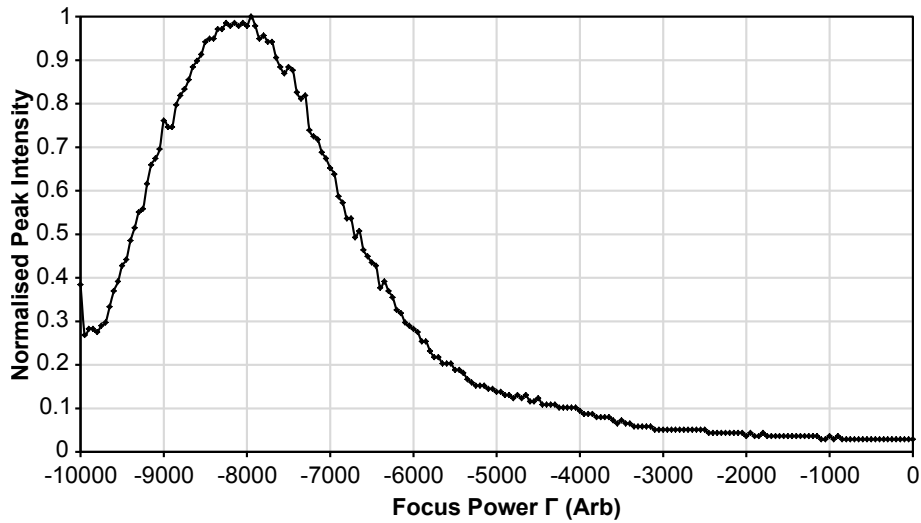


Figure 3.8: Z-offset of femtosecond beam. Determining the Z-offset required to bring the femtosecond laser spot in line with the imaging plane. Whilst focusing on the top surface of a 170 μm microscope slide the peak pixel intensity was acquired for a range of Fresnel lenses. The peak intensity corresponds to the point where the laser was focused and thus the strength of the Fresnel lens (Γ) required for the offset value.

matrices together and summing the components. Two well correlated images will yield a greater value than two dissimilar ones. Therefore each Fresnel lens can be scored against each manual fine focus reference image to obtain the value which produces the best match. These values were then plotted to obtain the gradient.

After obtaining the offset and gradient, it is then possible to control the Z-axis positioning of the focal spot relative to the top of the cover class.

3.6.5 Shot modalities

The ability to employ different shot modalities easily is important to improve the chances to successfully target the cell membrane with the femtosecond laser. Three different shot modalities were included: single shot, triple axial and lateral array. In each case, the dose time was set which controlled the timing of the mechanical

shutter. The triple axial approach uses three shots equally spaced in the z -axis by adjusting the strength of the Fresnel lens. For the lateral array, the number of shots and spacing can easily be changed. The Fresnel lens is not changed in this instance and the appropriate blazed grating is applied to displace the focal spot. In both cases, the timing between shots could be changed independently of the chosen dose time. A simple selection button allows users to quickly change between these different modes.

3.6.6 Amplitude correction

Whilst the position of the first-order focal spot can be readily controlled by changing the frequency of the blazed grating, the power decreases as the distance from the zeroth-order increases. As power is a crucial parameter to control in photoporation experiments, it is imperative to obtain a uniform response over the desired field of view. In order to characterise the efficiency of the blazed grating, an array of power measurements were made at the back aperture whilst the zeroth-order spot was blocked spatially. A LabVIEW virtual instrument (VI) was created which cycled through an array of blazed gratings whilst measuring the power using a power meter (Coherent). This array was then used to generate a map of pixel positions to normalised power. Figure 3.9 shows several threshold values generated from this map. The circular shape is a result of the iris that is used to block the zeroth-order. For small deflections from the origin, a small contribution from the second-order was also picked up during power measurements. Subsequent photoporation experiments were limited to the region where only the first-order remained unblocked by the iris. The diffraction efficiency decreases as distance from the zeroth-order increases. To correct this power discrepancy, it is necessary to generate a second spot

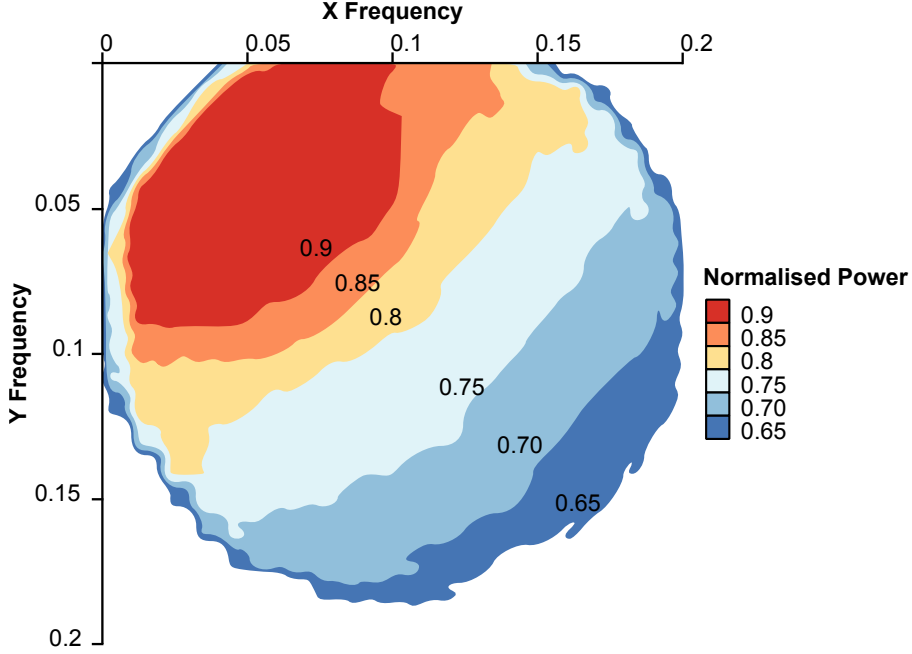


Figure 3.9: Diffraction efficiency using a SLM. A contour plot of back aperture power measurements shows the decrease in measured power as we move away from the 0th order (the origin). The circular shape arises from the iris used to block higher order terms. Close to the origin, the second order is still not blocked by the iris and so contributes to the measured power.

to use a dump for unwanted power. The complex field for the primary photoporation spot and the unwanted secondary spot can be described as [25]:

$$M(u, v) = A e^{\frac{2\pi i}{\lambda f}(u\Delta x + v\Delta y)} \cdot e^{\frac{-\pi i \Delta z}{\lambda f^2}(u^2 + v^2)} + (1 - A) e^{\frac{2\pi i}{\lambda f}(u\Delta x_0 + v\Delta y_0)} \quad (3.5)$$

Using this method generated additional ghost spots so it is necessary to place the secondary spot in a position that is blocked by the iris, therefore no ghost images are visible within the chosen photoporation region.

The relationship between the output power and the amplitude coefficient, A , was obtained experimentally and is shown in Figure 3.10.

By combining the power measurement map and the relationship between power and coefficient A it is then possible to reduce the power in the photoporation spot

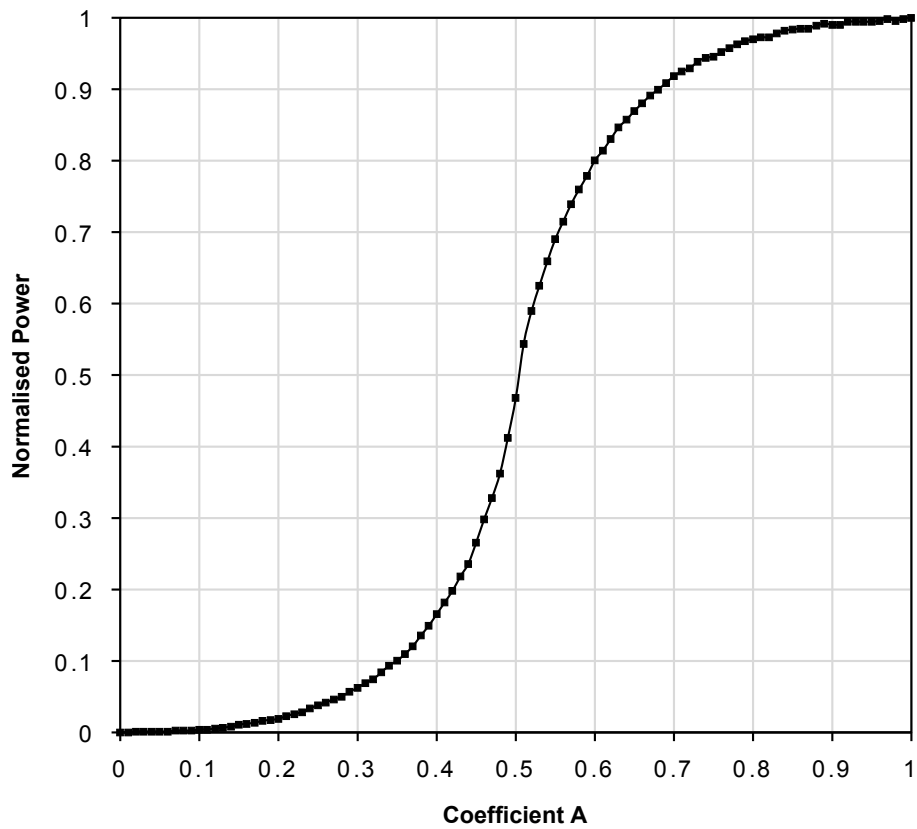


Figure 3.10: Experimentally obtained coefficient A. The measured power left within the photoporation spot when dumping power into a secondary spot by alternating the value of coefficient A.

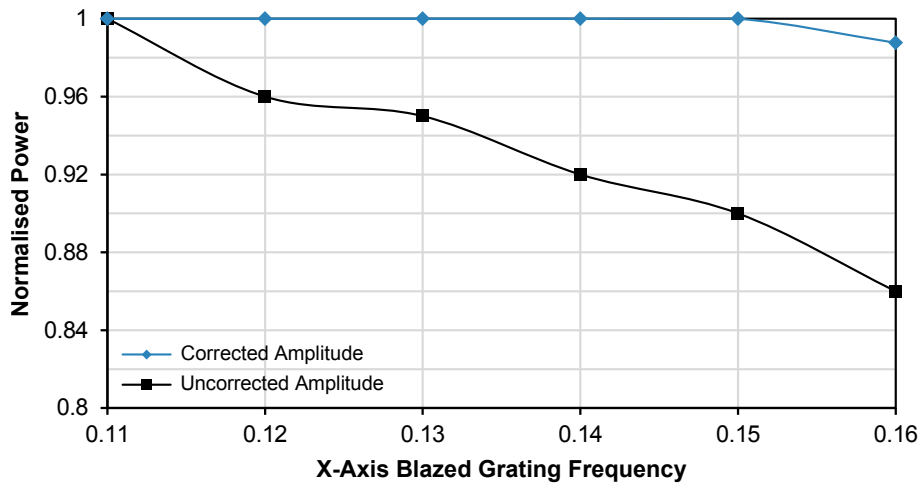


Figure 3.11: Amplitude correction. A plot of the back aperture power before and after correction along a $12\ \mu\text{m}$ line. These were conducted in the region where only the first-order spot is visible, all higher orders having been blocked. Over a $12\ \mu\text{m}$ by $12\ \mu\text{m}$ area there was a 15% drop when amplitude is uncorrected for. With amplitude correction there is at most a 2.5% variation in the measured power overall.

down to a chosen threshold. Lowering the threshold increases the area of uniform power at the expense of unused power.

The result of including amplitude correction is shown in Figure 3.11. This shows power measurements over a $12\ \mu\text{m}$ distance at a fixed Y position. Without amplitude correction there is a 15% decrease from the initial power. By implementing amplitude correction, in this case setting the threshold to 0.72, a far flatter response was obtained. Over a $12\ \mu\text{m}$ by $12\ \mu\text{m}$ region the correct amplitude never deviated by more than 2.5% between all points. No additional ghost spots were visible over this region suggesting good uniformity for photoporation.

3.6.7 Additional UI elements

Several additional elements have been added to the UI to improve ease of use and/or make small quality of life changes for users. A screenshot is shown in Figure 3.12.

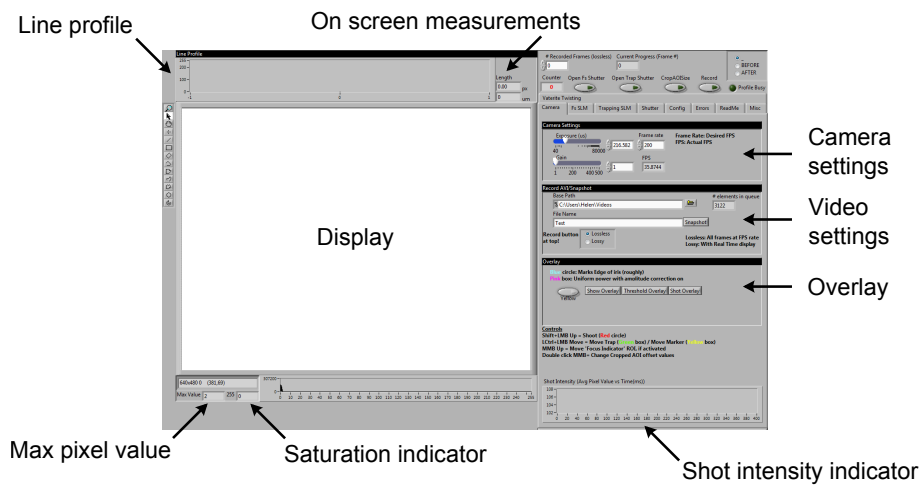


Figure 3.12: UI Screenshot The user interface has been designed with the aim of photoporation and trapping experiments. The majority of the space is devoted to a real time display from the CCD camera. Through a combination of keyboard and mouse commands, the position of an optical trap can be dragged across the screen or a range of femtosecond shot modalities can be triggered. The max pixel value and saturation indicator can be useful when looking at beam profiles as the background of the saturation indicator turns red when a pixel value of 255 is detected. Other settings on the front panel control the camera, recorded video or the display of overlays. Additional tabs contain controls for each SLM, including the application of aberration and amplitude correction.

On-screen measurement

When looking at a new sample, it can be useful to have a rough way to measure objects within the field of view. To do this, the front panel includes an indicator which shows the dimensions of a region of interest marked using the straight line tool. This reports as a number of pixels and an additional indicator displays this distance in microns. The scaling between these measurements was obtained using a graticule and was included as a constant within the workstation VI. It would be possible to include a selection of scaling factors if multiple objectives of differing magnifications were to be used routinely. A line profile is also produced along the region of interest to give a rough idea of beam profile.

Shot counter

Often in photoporation experiments, it is desired to target a pre-defined number of cells. The shot counter is a simple display which tracks the number of shots taken (triggered via Shift+LMB). The shot counter increments by one regardless of the shot modality employed, so the number of cells targeted is tracked rather than the number of femtosecond doses.

Saturation indicator

The saturation indicator offers a quick indication of whether the camera is saturated. It is designed so that if any pixels in the field of view are at the maximum value (255), the background of the indicator changes from white to red. This strong visual cue is helpful when inspecting the beam profile as it is easier to avoid saving saturated images. A second indicator indicates the current maximum pixel value.

Focus Indicator

A key requirement for successful photoporation experiments is correct positioning of the laser focus. With the motivation of improving the reproducibility of photoporation experiments between users, a ‘focus indicator’ was tested. The idea was to give a measurement to ensure cells were consistently shot in the plane and to reduce human error. The focus indicator was based on edge detection within a region of interest. It was found this was too weak when focusing on the cell edge for adherent cells due to the low contrast. It may however be something to revisit for spherical non-adherent cells, which have a more pronounced outline enabling edge detection.

Bubble detection

While optimising the power or beam position in photoporation experiments, noting the production of small bubbles can be helpful as an indication of success. The bubbles are short lived (of the order of milliseconds) and as a result, could be easily missed depending on the refresh rate of the ‘live’ camera view. The ‘shot intensity indicator’ displays the average pixel value for a small region of interest around the point which has received a femtosecond laser dose. When a bubble forms, it is detected by a small decrease in the intensity. An example of this is shown in Figure 3.13.

3.7 Optical Trapping

The trapping part of the system was tested using a variety of sizes of polystyrene and silica beads. Good 3D trapping was obtained when using a Nikon 60x WI objective (NA = 1.2). The system does not contain a motorised stage so ‘Q values’

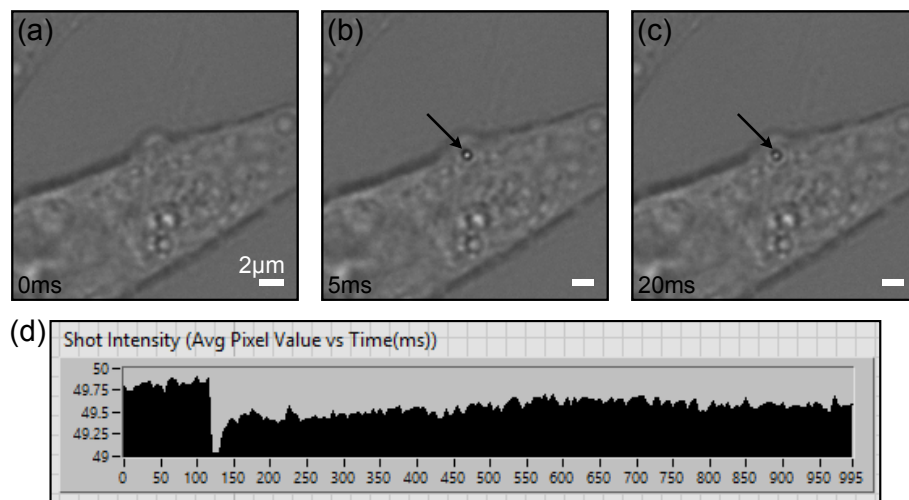


Figure 3.13: Bubble formation indicator One element of the user interface is a ‘shot intensity’. The display is useful when optimising the power and/or z-positioning for photoporation experiments. It displays the average intensity in a small region of interest around the targeted area. As the ‘live’ display updates at a slow rate compared to the maximum capture rate, it is easy to miss small bubble formation events. The ‘shot intensity’ indicator will analyse the event at 200 Hz regardless of the refresh rate of the ‘live’ display. Examples of a small bubble after exposure to the femtosecond laser is shown at (a) 0 ms, (b) 5 ms and (c) 20 ms. The black arrows show the location of the bubble. (d) An example of the generated shot intensity over 1 s

could not be measured. As the system is not equipped with a quadrant photodiode (QPD), position measurements were recorded using the CCD camera running at 200 Hz. This acquisition rate is too small to provide accurate power spectra which can be used to quantify the trap stiffness. As an alternative, we resorted to using the equipartition-theorem to obtain the trap stiffness constant, k . The method for trap calibration was described previously in Section 1.6. The results obtained for k_x and k_y for a range of polystyrene and silica particles are shown in Figure 3.14 and Figure 3.15. In both cases, a sparse suspension of particles in filter sterilised water was sealed between two 170 μm cover glasses separated by a vinyl spacer. In each case particles were trapped $\sim 5 \mu\text{m}$ above the bottom of the chamber. This was determined by trapping a particle, bringing it into contact with the bottom cover glass (to show visible displacement of the particle) before moving it away using the microscope fine focus. The power was measured at the back aperture with an iris in place set to match the back aperture of the objective. It was not possible to measure the transmission of the objective using the two objective method as there was only one objective of this type. Instead the transmission of the Nikon objective at 1070 nm was found to be equivalent to the Olympus 60x WI objective by experiments conducted by Matthieu de Saint Vincent. This transmission value, 64%, was used to calculate the approximate power at the sample.

Videos were captured at 200 Hz and analysed using a Matlab script written by Martin Kristensen. The Matlab script first applied a binary threshold to each frame on the video. Holes were filled to create a circular silhouette of the trapped particle. A circle was drawn around the particle and the centre of this was used as a centre of mass of the particle. For each data point, four 10000 segments of video were used to calculate the trap stiffness in the x and y directions (k_x and k_y). The error bars are

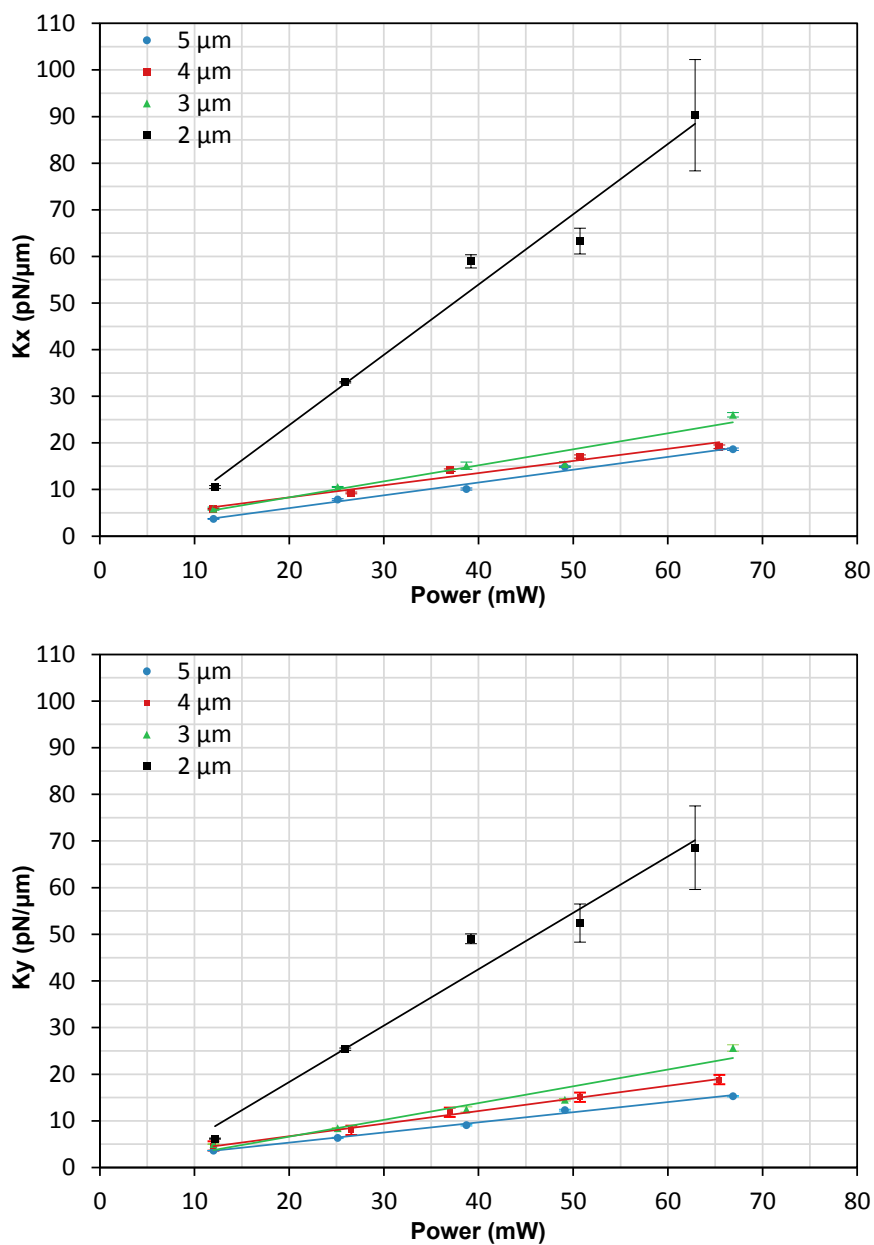


Figure 3.14: Trap stiffness measurements of polystyrene beads Polystyrene beads were optically trapped in filter-sterilised water 5 μm above the cover glass. The trapped particles were recorded at 200 Hz using the CCD camera. Each data point is an average of four 10000 frame segments of video. The error bars are the standard error of the mean. The power at the sample was calculated from the measured power at the back aperture using the transmission of the objective (Nikon 60x WI NA = 1.2).

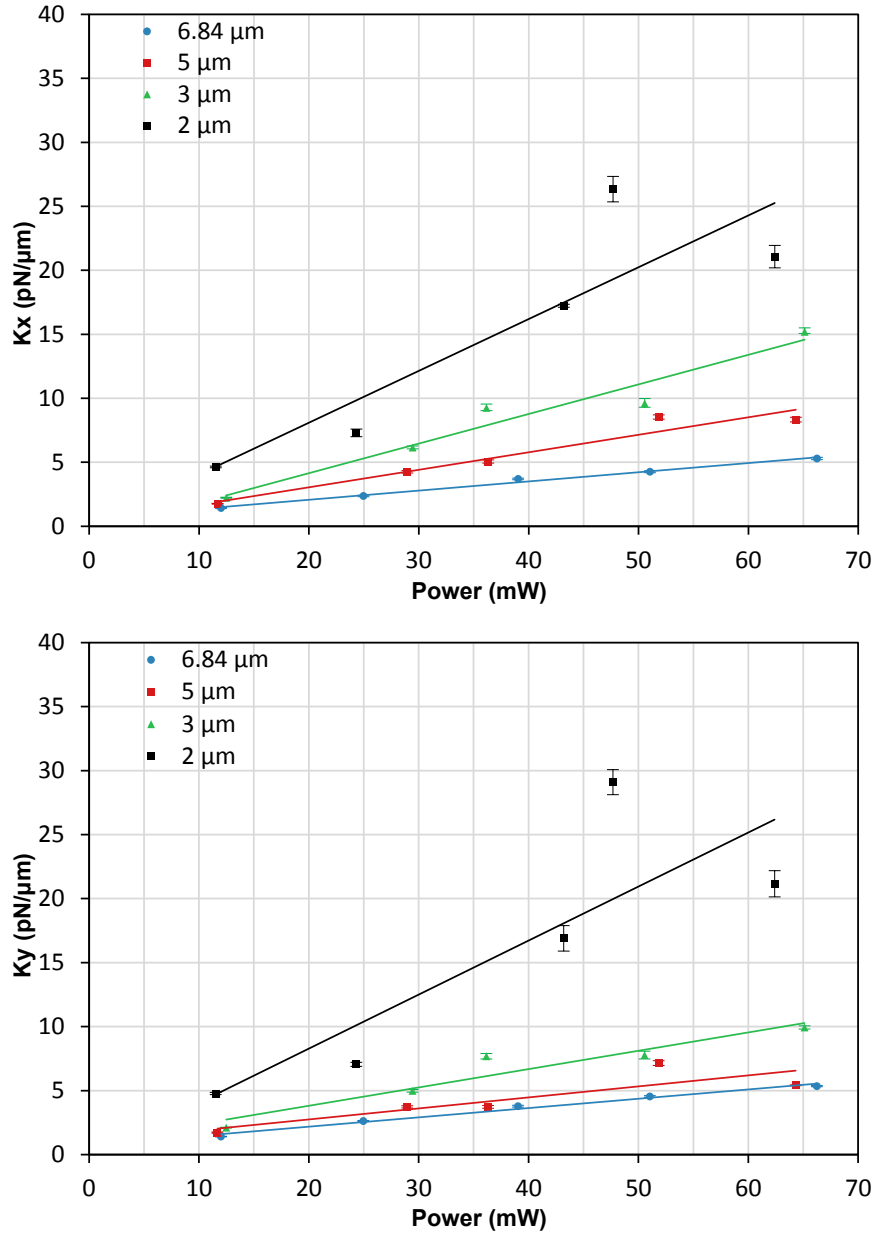


Figure 3.15: Trap stiffness measurements of silica beads Silica beads were optically trapped in filter-sterilised water 5 μm above the cover glass. The trapped particles were recorded at 200 Hz using the CCD camera. Each data point is an average of four 10000 frame segments of video. The error bars are the standard error of the mean. The power at the sample was calculated from the measured power at the back aperture using the transmission of the objective (Nikon 60x WI NA = 1.2).

the standard error of the mean. The temperature was assumed to remain constant at 293.15 K when calculating the trap stiffness.

As expected, the trap stiffness improved as the power was increased and smaller particles were more strongly trapped compared to larger particles. Cells could also be trapped in 3D using the water immersion objective which will be demonstrated in the next chapter. The ‘drag and trap’ interface described in Section 3.6.3 means that trapped particles or cells can readily be manipulated around the field of view.

3.8 Photoporation of adherent CHO-K1 cells

To test how well the system worked for photoporation, several optical injection experiments were performed on adherent CHO-K1 cells, a cell line which has commonly been used in other photoporation experiments. The different shot modalities were tested; a single shot, three axially spaced shots and a lateral array of shots. These were tested by the optical injection of propidium iodide (PI) and a subsequent viability test using calcein-AM (CAM).

3.8.1 Sample preparation for optical injection experiments

The CHO-K1 cells were cultured as described in the previous chapter (Section 2.7). 48 hours prior to experiments, CHO-K1 cells were plated onto 35 mm diameter glass bottomed dishes (WPI, Matek). Before each experiment, the cell monolayer was washed twice with 1 ml pre-warmed OptiMEM (Invitrogen). After washing, 300 μ l of 3 μ M PI solution in OptiMEM was added to the glass-bottomed dish. A brightfield and a fluorescence image were taken prior to laser irradiation for reference purposes using the cooled CCD camera (Clara, Andor). In the region of 40-50 cells were shot per dish. It can be helpful to mark targeted cells on the brightfield image to

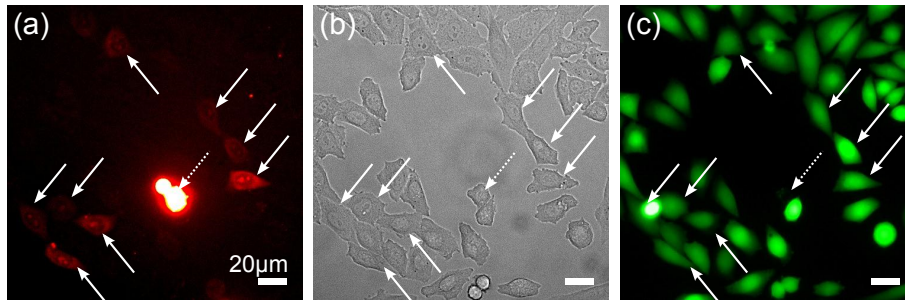


Figure 3.16: Images of optical injection. (a) Fluorescence images of propidium iodide. Propidium iodide is taken up by cells with compromised cellular membranes. Optically injected cells exhibit low levels of PI fluorescence (solid arrow). Cells which have died as a result of laser irradiation show strong PI fluorescence (dotted arrow)(b) Brightfield image taken before laser irradiation. The brightfield image was used as a reference so that cells not targeted multiple times. (c) Cells stained with calcein-AM, 90 minutes after laser irradiation. Non-viable cells do not retain the fluorescent calcein.

avoid targeting the same cell multiple times. 5 minutes after laser irradiation, a second brightfield and fluorescence image were taken to evaluate successful optical injection. After the cells had been treated, the dish was washed once with 1 ml of OptiMEM before the addition of 2 ml of pre-warmed cell culture medium. The dish was then returned to the incubator for 90 min before testing for cell viability.

To test for cell viability, the cells were washed once in 1 ml of D-PBS before adding 300 μ l of 2 μ M CAM solution in D-PBS. The dish was then incubated for a further 20 min before a subsequent wash in D-PBS. 1 ml of D-PBS was added to the dish before checking for calcein fluorescence.

An example of the images obtained are shown in Figure 3.16. Cells are targeted with reference to the brightfield image so as not to target the same cells multiple times. Cells which are successfully optically injected show an increase in fluorescence. Cells which die as a result of laser irradiation exhibit a strong fluorescence signal whilst optically injected cells which remain viable show low levels of PI. Viability is quantified using CAM.

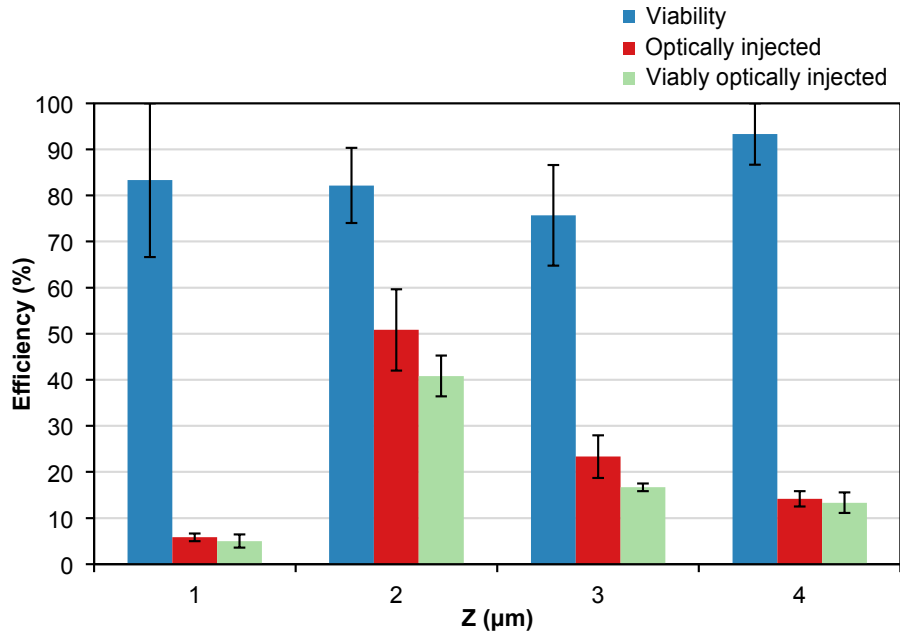


Figure 3.17: Optical injection using a single shot. To optimise the z positioning for the photoporation experiments, a series of dishes were optically injected with PI using a single 40 ms shot. The z position was adjusted using the Fresnel lens on the SLM. In each case, the top surface of the dish was used as a reference point by focusing on the thin edge of the chosen cell. The optimal position was found to be $2\ \mu\text{m}$ with significantly lower success away from this position. The graph shows results of optically injected adherent CHO-K1 cells with PI. Viability was assessed using Calcein-AM. The error bars are the standard error of the mean with $N = 3$

3.8.2 Optical injection results for adherent CHO-K1

The z -position of the femtosecond beam was optimised to hit the cell membrane. This was achieved by performing optical injection experiments using a single 40 ms dose. The power measured at the back aperture was 80 mW. In each dish 40 cells were targeted for optical injection of PI. As shown in Figure 3.17, the optimal position for the system was found to be for $Z = 2\ \mu\text{m}$ relative to the top surface of the glass dish (i.e. including the previously calculated offset). This position was used as the base position for all subsequent optical poration experiments.

After optimising the z -position of the laser focus, optical injection experiments

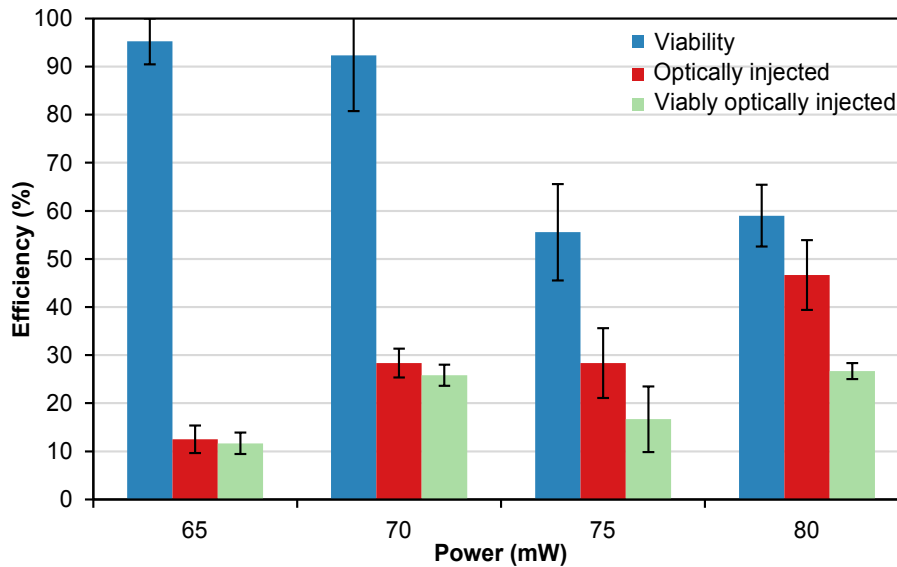


Figure 3.18: Optical injection using a triple Z shot. Optical injection of adherent CHO-K1 cells with PI using the triple Z shot modality. In this case, 3 40 ms shots were made sequentially with 1 μm vertical spacing. In this case, the two additional shots are made 1 μm above and below the nominal z position of 2 μm . The error bars are the standard error of the mean with $N = 3$

were carried out on adherent CHO-K1 cells to test the additional shot modalities incorporated into the system. These modes are a 4x4 array of shots and three axially separated shots. For three axially spaced shots ('triple Z' mode), the shots were spaced axially $\pm 1 \mu\text{m}$ from the nominal z-position of 2 μm . This mode was tested at a range of powers as shown in Figure 3.18. There was no significant difference of the percentage of optically injected cells between powers $P = 70 \text{ mW}$ and $P = 75 \text{ mW}$. However, cell viability was significantly reduced at $P = 75 \text{ mW}$. A power equal to $P = 70 \text{ mW}$ appears to be the optimal point for viable optical injection.

For the array approach, sixteen 40 ms doses were administered to each cell with 3 μm spacing. The Fresnel lens was set at $Z = 2 \mu\text{m}$ for each shot. The benefit of this approach is that by covering an area which largely covered a cell, axial displacement of shots relative to the membrane will occur naturally due to the curved topology of the cell body. This approach was used at different powers, measured at the back

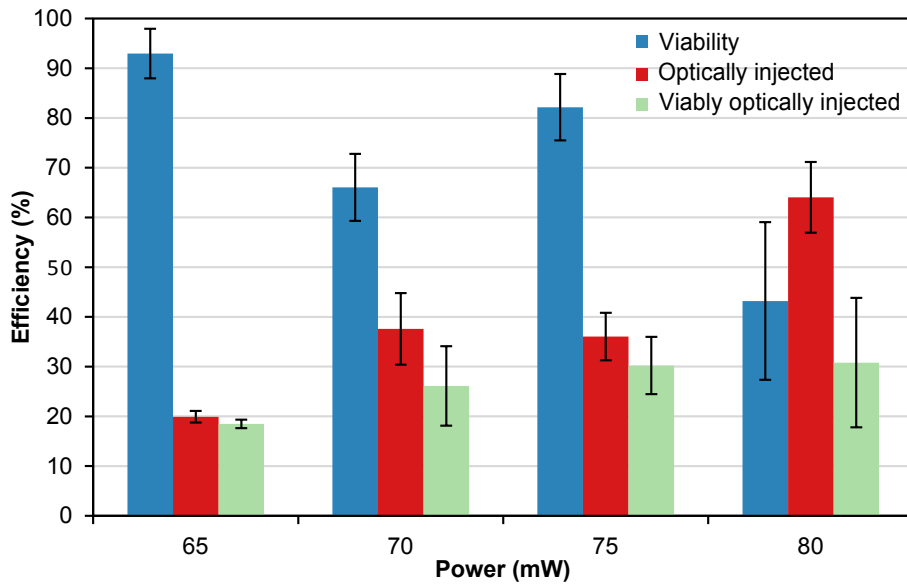


Figure 3.19: Optical injection using 4x4 grid of shots. Optical injection data for adherent CHO-K1 cells shot using a series of 40 ms shots arranged in a 4 by 4 grid. The spacing between each shot was 3 μm . Cell viability significantly deteriorates at 80 mW where often multiple bubbles or very large destructive bubbles were produced. The error bars are the standard error of the mean with $N = 4$

aperture, as shown in Figure 3.19. As with the triple axial approach there was no significant difference of optical injection observed between $P = 70 \text{ mW}$ and $P = 75 \text{ mW}$. However, there was a significant difference between $P = 65 \text{ mW}$ and $P = 80 \text{ mW}$. The increased optical injection at $P = 80 \text{ mW}$ comes at the expense of viability, reducing the number of viable optically injected cells. It should be noted that during the experiments conducted at $P = 80 \text{ mW}$, often multiple bubbles or large destructive bubbles were observed. From these experiments, a power $P = 70 \text{ mW}$ to 75 mW appears to be the optimal power for viable optical injection using the 4x4 grid of shots.

3.8.3 Attempts at optical transfection

Additional biological considerations

As noted in Section 1.2 there is a defined difference between optical injection and optical transfection. Optical transfection is more specialised than optical injection and describes the technique of delivering genetic material into cells. This means that the photoporation event is not only based on a physical response of the cell to the laser, but attentionally requires a biological response to the new genetic material. The 2013 Nature Protocols paper by Antkowiak et al states that optical injection of small molecules can be achieved with a single irradiation whilst optical transfection is more efficient when using multiple irradiations at lower powers [17].

There are a number of biological considerations which should be observed during optical transfection experiments which are not relevant or are less critical for optical injection experiments. Cell density is important as cells which are allowed to become 100% confluent exhibit lower metabolic rates and a decreased rate of cell division after being sub-cultured. Cell division rate is also reduced as the cell passage number increases (the number of times cell have been sub-cultured) which has been shown to affect the optical transfection efficiency of CHO-K1 cells [102]. Furthermore contaminations in the cell culture such as mycoplasma affect cell division rates.

Transfection efficiencies have also been shown to be affected by the phase of cells within the cell cycle. Cells transfected during the G1 phase show lower expression compared to cells transfected in either the S or G2 phases [103]. It is thought that this is due to DNA in the cytoplasm being degraded by nucleases before it can be transcribed [104]. For this reason it is important to ensure cell division is not hindered.

During all transfection experiments attempted in this thesis, care was taken to ensure cell did not become 100% confluent and cell passage number was monitored to ensure normal proliferation rates. Additionally mycoplasma testing was performed periodically.

Transfection of adherent CHO-K1 cells

Before moving on to experiments on non-adherent cells, it is important to test the system using ‘traditional’ adherent cells as a comparison. CHO-K1 cells were cultured and plated onto glass-bottomed dishes as described for the optical injection experiments. The plasmid, pCAG-GFP, was added to pre-warmed opti-MEM at a concentration of $10\ \mu\text{g ml}^{-1}$ before each experiment. The dish was washed twice with 1 ml of pre-warmed OptiMEM before adding 300 μl of $10\ \mu\text{g ml}^{-1}$ pCAG-GFP solution in OptiMEM.

40 cells were targeted in each dish within a region of interest in the centre of the dish. This was marked using a permanent marker on the base of the dish. After dosing the targeted cells, the dish was washed twice with 1 ml of pre-warmed OptiMEM before adding 2 ml of MEM and returning the dish to the incubator. Care was taken to ensure that each dish spent less than 30 minutes outside of the incubator. The dishes were observed for signs of transfection 24 hours and 48 hours after the experiment. Control dishes were also prepared in the same way but without exposure to the femtosecond laser.

A range of powers and dose times were tried. Transfection experiments typically require less power compared to optical injection experiments [17]. From the optical injection results conducted in Section 3.8.2, a power of 65 mW was initially used for transfection attempts as this power showed higher viability and lower optical injection compared to higher powers. Using the 4x4 array of shots, at least 4 dishes

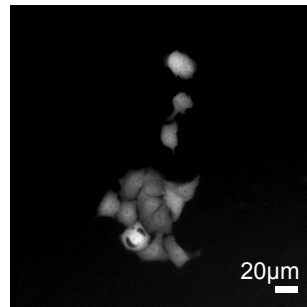


Figure 3.20: Optical transfection of CHO-K1 cells The result of optical transfection of CHO-K1 cells with pCAG-GFP. 40 cells were treated in the dish with each cell targeted by a 4x4 array of shots with $P = 65$ mW and a dose time of 200 ms. An additional six dishes were treated using these parameters, however the result was not reproducible.

were tried at three different dose times. The dose times used were 40 ms, 100 ms and 200 ms. Of these dishes, including control dishes, transfected cells were only observed in one dish as shown in Figure 3.20. This dish was treated using $P = 65$ mW and a dose time of 200 ms. An additional 6 dishes were treated using these parameters, however no further transfection was observed. Transfection was also attempted using a lower power of 55 mW and dose times of 100 ms and 200 ms which were also unsuccessful. In addition to the 4x4 shot mode, 6 dishes were tried using the ‘triple Z’ approach using a dose time of 40 ms and powers $P = 55$ mW and $P = 65$ mW. No transfection was observed using these parameters.

The lack of transfection whilst obtaining good optical injection results suggests a biological problem. The plasmid was tested using Lipofectamine 2000 to transfect the CHO-K1 cells. Lipofectamine is a common transfection agent. The Lipofectamine 2000 was administered following the manufacturer’s protocol (Invitrogen). Cells were successfully transfected 24 hours after administering the Lipofectamine. This suggests that the stock plasmid is ok as are the cell cultures.

Another possibility is that the plasmid is deteriorating in quality in the Opti-MEM solution over the course of the experiment. To test this, a Western blot was

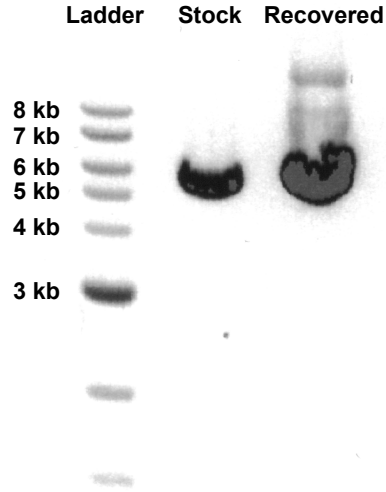


Figure 3.21: Western blot of pCAG-GFP. A Western blot of the pCAG-GFP plasmid to be used for optical transfection experiments. ‘Stock’ refers to DNA taken from the original stock stored in TE buffer and at -20°C . ‘Recovered’ refers to DNA recovered from a $10\ \mu\text{g ml}^{-1}$ solution in OptiMEM stored at 37°C for several hours. The pCAG-GFP plasmid is 4.8 kb in size.

run on both the stock plasmid (stored in TE buffer) and from plasmid recovered from a Opti-MEM solution kept in a water bath for 6 hours. The results are shown in Figure 3.21. As expected the main band lies at ~ 5 kb. The size of the plasmid is 4.8 kb as reported on addgene [105]. Elaine Campbell provided assistance with running the Western blot.

Comparison of parameters with published results

The laser parameters required can vary between cell lines [17]. The CHO-K1 cell line was used as it has often been used in previous studies [106]. A table of comparison of the reported parameters used for successful optical transfection of CHO-K1 cells using a femtosecond laser. For the sake of comparison, Table 3.1 focuses on cases

Power (mW)	Dose (ms)	Method	Plasmid	Efficiency	Ref.
60-70	40	3 shots	pDsRed2-Mito 10 $\mu\text{g mL}^{-1}$	20%	[53]
60	40	3 shots	pDsRed2-Mito 10 $\mu\text{g mL}^{-1}$	40-60%	[102]
60	40	untargeted raster 1 shot per cell	Mito-DsRed 10 $\mu\text{g mL}^{-1}$	20%	[25]
70	40	3 shots	Mito-DsRed	50%	[23]

Table 3.1: Comparison of parameters for successful optical transfection of CHO-K1 cells using a femtosecond laser.

where a Gaussian beam has been used and no additional transfection agents have been added. Typically a laser power of 60 mW to 70 mW is used and 3 sequential 40 ms shots have been used. These powers fall in line with the powers used during attempts outlined in this chapter. The 4x4 array of doses was used rather than 3 sequential doses as it has been shown to result in better transfection efficiencies compared to a single dose or three axially-spaced doses [19]. Hence it can be concluded that the parameters used during transfection attempts are sensible when comparing them to previously published work.

3.9 Conclusions and future work

In this chapter the use of AODs and SLMs for beam steering was discussed. Whilst the AOD provides superior speed compared to the SLM, it is more suitable for 2D deflections rather than providing full 3D control of the focal spot. AODs are more suitable for optically trapping as they increase the pulse duration of femtosecond pulses which is not ideal for photoporation. The SLM has the additional benefit that it can be used for aberration correction.

A workstation was designed and built with both photoporation and trapping

capabilities. The aim is to have a system designed to investigate the important experimental parameters required for transfection of non-adherent cells and adherent cells in a suspension. Probing these parameters could provide useful information to aid microfluidic optical transfection using the system outlined in Chapter 2. In order to create a user-friendly system, a user interface was created in LabVIEW. This controlled a number of elements including two SLMs, a mechanical shutter and a fast camera. Calibration of the blazed grating frequency to pixel position allows for a ‘point and shoot’ and ‘drag and trap’ interface. Additional calibration was implemented to ensure the power contained within the photoporation spot was uniform across the field of view.

Optical trapping was tested for a variety of polystyrene and silica beads. Good 3D confinement was obtained when using a Nikon 60x WI objective lens ($NA = 1.2$). Optical injection of PI was tested on adherent cells to optimise the z-position of the focal spot and to test two different shot modalities. These modalities were a 4x4 array of shots with $3\ \mu\text{m}$ spacing and three axially spaced shots.

The results from the optical injection experiments were used to choose reasonable starting parameters for attempts to optically transfect adherent CHO-K1 cells with the pCAG-GFP plasmid. Despite trying a range of different powers and exposure times, only one dish showed any signs of transfection (4x4 grid, $P = 65\ \text{mW}$, dose time of 200 ms). Repeating experiments using these parameters did not provide reproducible results. The plasmid was tested using the transfection agent Lipofectamine 2000 which did successfully transfect the cells. The plasmid was also tested for degradation after several hours in a OptiMEM solution. No noticeable degradation was observed. It is currently unknown what is preventing optical transfection using the system.

Immediate future work would be to resolve the current issues of optical trans-

fection. I suggest returning to plasmids which have been used more frequently in optical transfection experiments such as mito-dsRed which uses the CMV promoter. If this plasmid works, it suggests there is something wrong with the pCAG-GFP for optical transfection.

Once transfection of adherent cells has been achieved, future work would look at the parameters required for non-adherent cells and adherent cells in suspension. In the case of adherent cells in suspension, a possible avenue to explore is the effect of the method of dissociating cells from the culture flask. This would include comparing cells detached using Trypsin-EDTA and Accutase. Accutase is reportedly gentler compared to Trypsin-EDTA and so may have a positive impact for optical transfection. In addition to methods of detaching cells, future studies could include how experimental parameters (e.g. power and dose time) compare to adherent cells. The method used to shoot cells (i.e. a lateral array or axially displaced shots) could play an important role in producing reliable photoporation of cells in suspension due to the difference in shape. Suspension cells naturally take on a spherical shape whilst adherent cells are flatter and ‘egg-shaped’. The inclusion of the optical trap would allow for targeted cells to be moved away from the untreated cells. This could be achieved using a microfluidic chip with multiple reservoirs. Separating treated cells spatially would give a better idea of the efficiencies achieved as they would not be lost among the rest of the cell population.

Whilst transfection has not yet been achieved using the system, a large amount of the ground work has been done to provide the tools required for these experiments. The combination of the femtosecond laser for photoporation and an additional laser for trapping should give good flexibility to move and photoporate cells in suspension. This will hopefully provide new information of which parameters are important for dealing with these types of cells.

3.10 Contributions

The system was designed by H. Rendall and built with assistance from M. Kristensen. The LabVIEW interface was designed and implemented by H. Rendall, with the exception of the VI used to generate the aberration correction hologram which was created by T. Vettenburg. M. Kristensen provided the Matlab code used to calibrate the z-axis of the Fresnel lens and analyse trapping data. T. Čížmár provided assistance troubleshooting the faulty digital frequency synthesizer. E. Campbell provided assistance running the western blot on the pCAG-GFP plasmid. Measurement of the pulse duration was conducted with assistance from A. McDonald. J. MacIntyre provided the pCAG-GFP plasmid used for optical transfection experiments. All experiments and subsequent data analysis were conducted by H. Rendall.

4

Temporal focusing for multiphoton imaging of optically trapped cells

In the last decade there has been a number of advances in the area of optical manipulation, combining imaging with trapping modalities. In this chapter a microscope system is presented which combines temporal focusing for multiphoton illumination with optical trapping for the micro-manipulation of cells. Temporal focusing is achieved using a Ti:sapphire femtosecond laser combined with a grating. This produces a plane at the sample where the pulsed light is focused temporally rather than spatially. Axial sectioning is achieved by either moving the objective relative to the sample or by moving the sample, held in an optical trap, through application of an appropriate Fresnel lens to a spatial light modulator.

4.1 Introduction

Over 50 years ago the confocal microscope, created by Minsky, which revolutionised microscopy by overcoming the limitations of wide-field fluorescence microscopy and enabling optical sectioning [107]. The technique has advanced tremendously over the years. However, it relies on scanning a single point across a sample or moving the sample in order to create an image. Multiphoton techniques, such as two-photon laser scanning fluorescence microscopy developed by Denk et al in 1990, capitalise

on the benefits of using a non-linear process for excitation [108]. As two-photon absorption is non-linear, it requires the high peak powers from a pulsed laser source in order to excite the sample at the laser focus. The benefit of multiphoton imaging over standard single-photon microscopy is the reduction of photo-damage and photo-bleaching and lower scattering due to the longer excitation wavelengths used. Like confocal microscopy, multiphoton techniques generally require scanning of this focal spot in order to generate an image. The time taken to acquire an image will depend on the area which is to be imaged thus acquisition times can range from seconds to minutes. There is inevitably a time delay scanning each point of the image which may prevent imaging fast events.

This chapter will first look at an alternative to confocal and two-photon scanning techniques known as temporal focusing. The technique focuses pulsed temporally at the sample plane rather than spatially. The benefit of this is that a larger sample area can be simultaneously imaged without the need for scanning.

Next the optical system, which is a modification of the workstation in the previous chapter, will be described.

Finally, the microscope system will be tested using both adherent and non-adherent Chinese hamster ovary (CHO-K1) cells and temporal focusing is combined with optical trapping for the first time. This allows us to acquire a series of axially spaced images without moving the objective or sample stage.

4.2 Temporal Focusing

Temporal focusing of the excitation pulse for scanless depth-resolved microscopy was first realised by Oron et al in 2005 [109]. Figure 4.1 depicts the principle difference between spatial focusing and temporal focusing. Multiphoton microscopy

typically combines ultrashort pulses with spatial focusing to generate a high intensity at the focus. The pulse duration remains unchanged as it propagates through the sample [109]. Temporal focusing differs from spatial focusing in that the excitation beam is weakly focused spatially and thus excites a far larger area. The high peak intensity is achieved by controlling the temporal profile as the light travels through the sample. The pulse is compressed as it travels through the sample and is shortest at the focal plane. The benefit of this approach is that a far larger area can be simultaneously excited whilst retaining depth resolution. Additionally, high illumination uniformity is achieved over the excitation region as it is dependent on the spatial uniformity of the excitation pulse.

Temporal focusing can be achieved experimentally in two different ways, by illuminating a diffuser placed conjugate to the imaging plane of a 4f-telescope or by using a blazed diffraction grating. The axial resolution of the former has been shown to be linearly dependent on pulse duration requiring ultrashort pulses to achieve similar axial resolution to line scanning [109, 110]. The blazed grating approach is valid for longer pulses (100 fs) and is thus easier to incorporate into microscopy systems. In this arrangement the spatially separated spectral components in the pulse meet again at the sample plane. The sample is effectively scanned by the pulse itself which allows for fast acquisition times compared to a typical point scanning method.

The Rayleigh range, Z_R , for a temporally focused beam can be expressed as [111, 112]:

$$Z_R \approx \frac{2f^2}{k}(s^2 + \alpha^2\Omega^2) = \frac{\lambda}{\text{NA}_{obj}^2} \quad (4.1)$$

where f is the objective focal length, k is the mean magnitude of the excitation

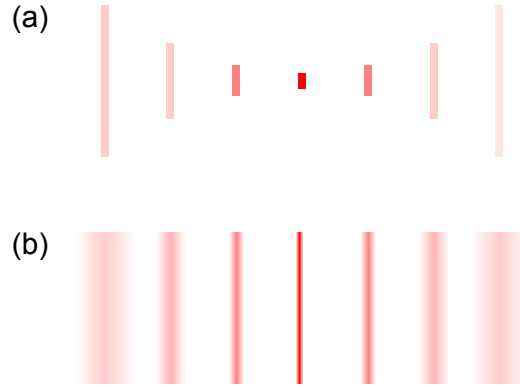


Figure 4.1: Cartoon of spatially focused light compared to temporally focused light (a) Techniques such as confocal microscopy use spatially focused light where a high peak intensity is achieved at the focus of the objective lens. This illuminates only a small volume of the sample and requires scanning of the focus to image large areas. (b) Temporally focused light uses a pulsed laser source and the beam is not tightly focused, thus illuminating a larger sample area. A high intensity is achieved at the sample plane by modifying the temporal profile of the incoming light which is shortest at the focus of the objective lens.

wavevector, s and $\alpha\Omega$ are the spot sizes at the back aperture in the direction orthogonal and parallel to the grating dispersion, λ is the laser wavelength and NA_{obj} is the numerical aperture of the objective lens. The diffraction grating causes a spread of the spectral components so that in one direction, the objective back aperture is always filled (i.e. $\alpha\Omega > \text{diameter of the back aperture}$).

As the axial resolution depends only on the objective NA, the area of excitation can be increased without compromising the axial resolution. This would be the case for a typical Gaussian beam as increasing the focal spot size involves underfilling the back aperture of the microscope objective, reducing the effective NA, and thus degrading the axial resolution. A table of comparison between typical Gaussian excitation and temporally focused illumination is shown in Table 4.1.

Illumination	Z_R	Max excitation density	Additional losses
Conventional Gaussian	$\frac{\lambda}{\text{NA}^2}$	$\frac{P}{w_0}$	-
Temporal focusing	$\frac{\lambda}{\text{NA}_{obj}^2}$	$\frac{P}{A_{spot}}$	15-20% at grating

Table 4.1: Comparison of Conventional 2-photon microscopy with temporal focusing. Scanless temporal focusing provides an axial resolution which is independent of the illuminated area (A_{spot}). This allows for a greater area to be excited as long as there is sufficient laser power, P , to provide the necessary illumination intensity [111].

4.2.1 Developments and applications of temporal focusing

There have been several papers published in recently years which utilise temporally focused light. The technique was first described by Oron et al [109] and separately by Zhu et al in 2005 [113] as a method for scanless multiphoton imaging. Shortly after, Durst et al demonstrated control of the axial position of the temporal focal plane by adjusting the dispersion in the system [112]. They report that when the group velocity dispersion is small, the shift of the temporal focal plane has a linear relationship with the dispersion. As a result, by adjusting the group velocity dispersion the position of this plane could be controlled. They demonstrated that this property is suitable for a fibre-based delivery system.

Tal et al included line-scanning into their temporal focusing system using a cylindrical lens combined with a 1D scanning mirror [110]. Using line temporal focusing it was possible to obtain axial resolutions similar to single-point multiphoton scanning techniques whilst scanning only in 1D. This resulted in an axial resolution of 1.5 μm with video-rate acquisition.

Other studies have looked at the characteristics of temporal focusing in scattering media. Dana et al investigated the performance of temporal focusing in both trans-

parent and scattering media [114]. Their results suggested that the axial sectioning deteriorates at a much faster rate compared with standard two-photon microscopy as the propagation depth is increased. The following paper looked at the efficiency of line temporal focusing [115] (using a cylindrical lens, as seen earlier in a paper by Tal et al [110]). This hybrid between scanless temporal focusing and standard two-photon microscopy showed improved performance at depth compared to standard temporal focusing systems. Thus deep tissue studies may benefit by using line temporal focusing over temporal focusing alone.

The effect of aberrations in temporal focusing systems has also been investigated, as reported by Sun et al [116]. They modelled the effects of different Zernike polynomials (previously mentioned in Section 3.5.1) on both line and wide-field temporal focusing with line spatial focusing. Wide-field temporal focusing was found to be more robust to Zernike modes compared line focusing. They state the next stage of their model is to look at more complex temporal focusing systems such as those involving patterned illumination. The results of these studies may be incorporated into a system using spatial light modulator (SLM)-generated patterned illumination for improved performance.

Perhaps the most interesting biophotonics application thus far has been using beam shaping for patterned two-photon excitation of channelrhodopsin-2, published in 2010 [117]. The Nature Methods paper builds on previous work also published by Papagiakoumou et al which demonstrated how an SLM could be incorporated into a temporal focusing system for patterned illumination without compromising the axial resolution [118, 119]. In their investigation, single neuron cells expressing channelrhodopsin-2 were selectively illuminated to evoke action potentials which could lead to further studies on neural networks[117].

4.3 Experimental Setup

The workstation for photoporation and trapping, outlined in chapter 3 was modified as depicted in Figure 4.2 and Figure 4.3. The aim of the system is to allow for both temporal focused illumination with simultaneous trapping capabilities. The optical arm responsible for trapping remains largely unchanged and is described in more detail in section 3.3. A femtosecond laser (Mira, Coherent. $\lambda = 800$ nm, 150 fs pulse duration, measured after the polarising beam splitter, at a 80 MHz repetition rate) was used for temporal focusing. The laser output is expanded (L_1 , $f_1 = 75$ mm and L_2 , $f_2 = 250$ mm) before impinging on a blazed diffraction grating (600 lines/mm). The grating was aligned perpendicular to the optical axis and lies on a conjugate plane to the sample. A relay telescope was required due to space requirements. The final telescope consists of L_5 ($f_5 = 400$ mm) and the objective lens. The objective lens was changed depending on the experiment. A Nikon 60x objective (NA = 1.2) was used for experiments involving both temporal focusing and optical trapping. The femtosecond laser and trapping laser are combined before entering the microscope body. The trap position(s) was/were controlled using the custom LabVIEW program described in the previous chapter (See also Appendix A). Fluorescence images were acquired using a cooled CCD camera (Clara, Andor).

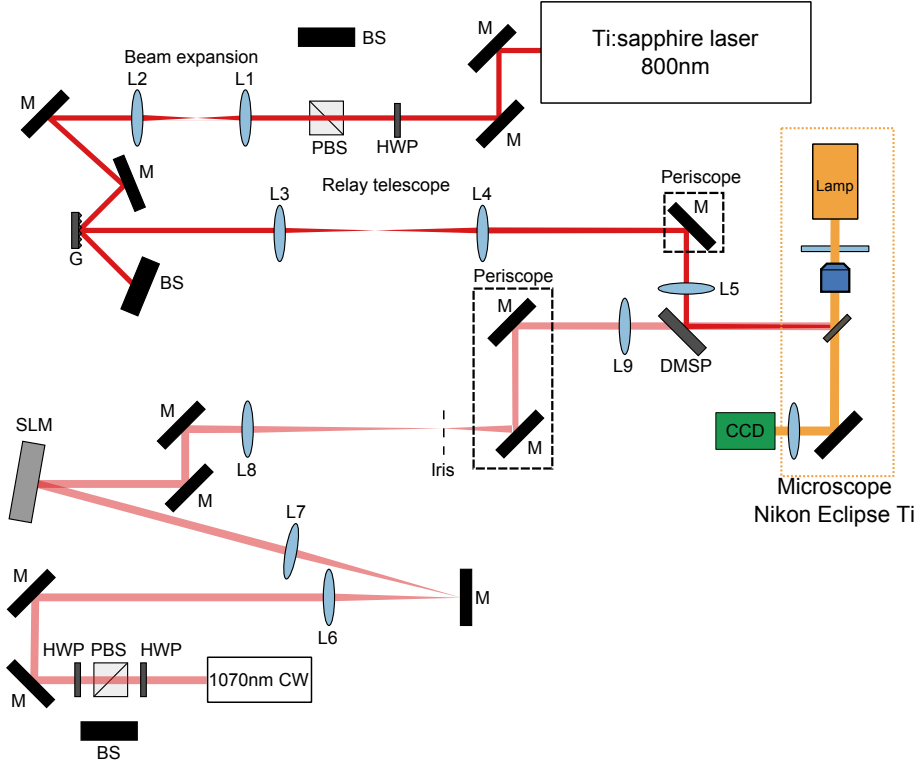


Figure 4.2: Optical setup for the modified workstation for temporal focusing and trapping. A Ti:sapphire laser (Mira, Coherent, $\lambda = 800$ nm, 150 fs pulse duration at a 80 MHz repetition rate) is used for temporal focusing. The power and polarisation are controlled through a combination of a half-wave plate (HWP) and a polarising beam splitter (PBS). The beam is then expanded (L_1 , $f_1 = 75$ mm and L_2 , $f_2 = 250$ mm) before the blazed refractive grating (600 lines/mm). The grating lies on the conjugate plane to the sample. Due to space constraints a relay telescope (L_3 , $f_3 = 100$ mm and L_4 , $f_4 = 100$ mm) is placed after the grating. The final telescope consists of L_5 ($f_5 = 400$ mm) and the objective lens. The trapping arm remains largely the same as before. The beam of an 1070 nm continuous-wave fibre laser (IPG Photonics) is expanded (L_6 , $f_6 = 150$ mm and L_7 , $f_7 = 400$ mm) before the SLM (SLM Hamamatsu X10468-03). The plane of the trapping SLM is relayed by a second telescope consisting of L_8 , $f_8 = 400$ mm and L_9 , $f_9 = 400$ mm. The two lasers are combined by a short-pass dichroic mirror (DMSP1000) before entering the microscope. A commercial Nikon microscope is used with an appropriate dichroic to reflect both the 800 nm and 1070 nm lasers to the microscope objective. Note the second mirror in one of the periscopes has been omitted for clarity.

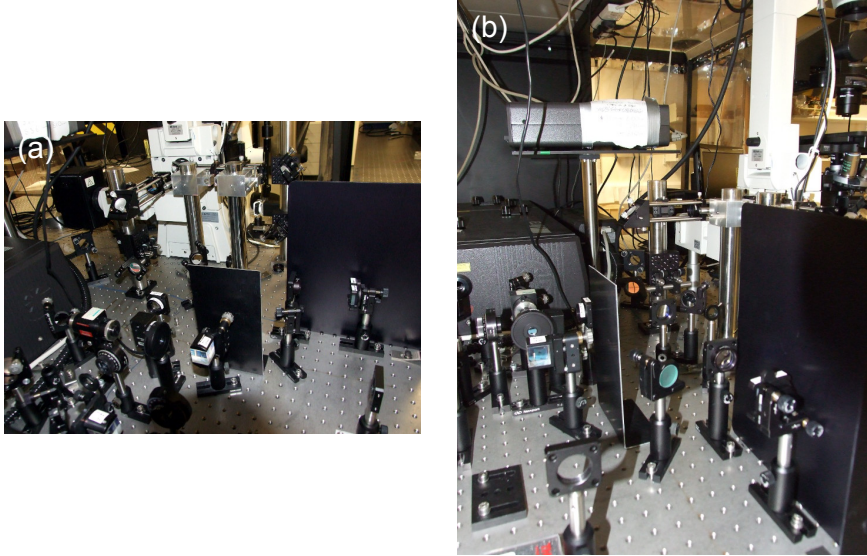


Figure 4.3: Modified workstation (a) + (b) Photos of the optical system for temporal focusing.

4.4 Imaging using temporally focused femtosecond pulses

4.4.1 Temporal focusing with different magnifications

In order to test the imaging capabilities using temporally focused femtosecond light, the axial resolution was measured by exciting a thin fluorescent sample. A variety of fluorescent samples had been previously used to test the axial resolution of a temporal focusing imaging system. Some have used either a $0.8\ \mu\text{m}$ spin-coated layer of the fluorescent dye Coumarin 515 [120, 109] or Rhodamine Chloride 610 in PMMA [118, 119]. Dana et al used either a layer of $10\ \mu\text{m}$ fluorescent beads [114] or a layer of fluorescein [115]. It should be noted that Dana et al used a second objective to image the fluorescence and so using a thin layer, less than the expected full width at half maximum (FWHM), is less critical to measure axial resolution.

This is because the second objective can be moved independently of the objective delivering the temporally focused light.

Here, the sample used was a thin layer of small green fluorescent beads (0.054 μm diameter) which were dried onto a 170 μm thick cover slip. The green fluorescent beads can be excited by the 800 nm femtosecond laser via two-photon excitation. As the same objective is used for both excitation and collection of fluorescence, the beads used for the sample had a diameter that was far smaller than the expected FWHM.

The axial resolution was measured by imaging the fluorescence signal obtained from the layer of green fluorescent beads over a range of objective positions. These images were acquired using a cooled CCD camera in 1 μm intervals by moving the microscope fine focus manually. The magnification of the initial expansion telescope (L_1 and L_2 as depicted in Figure 4.2) was changed by a factor of two. The effect of increasing the spot size incident on the blazed grating is an increase of the lateral field of view. It is expected that, in the case of temporally focusing, increasing the excitation area does not affect the axial resolution (i.e. axial FWHM) whereas in the case without temporal focusing the axial FWHM increases. The latter is equivalent to underfilling the microscope objective. It is this property of temporal focusing which allows for patterned two-photon illumination using a SLM as described by Papagiakoumou et al [118]. This work was then applied to patterned excitation of channelrhodopsin-2 in neurons in 2010 [117]. Figure 4.4 shows the axial response for two different expansion telescopes (i.e. two different spot sizes at the sample). The fluorescence has been normalised for comparison. There is little difference between the observed axial FWHM which is $\sim 7.5 \mu\text{m}$ in each case. This agrees with the expected result in the case of temporal focusing.

The second experiment was to compare the effect of changing the microscope

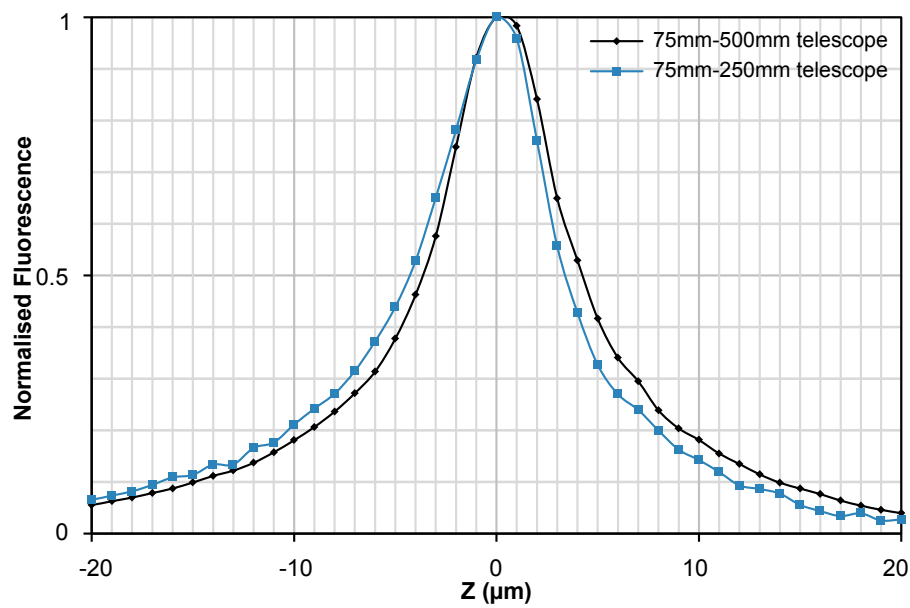


Figure 4.4: Axial profile of temporally focused beam with different beam expansion. The axial response of the system was tested using a 60x WI objective (Nikon, NA = 1.2) to excite a thin layer of $0.054\ \mu\text{m}$ green fluorescent beads. This was measured using a cooled CCD camera (Clara, Andor). In this case the illuminated area was altered by changing the initial beam expansion telescope (where L_1 , $f_1 = 75\ \text{mm}$ and L_2 , $f_2 = 250\ \text{mm}$ or $500\ \text{mm}$ as shown in figure 4.2).

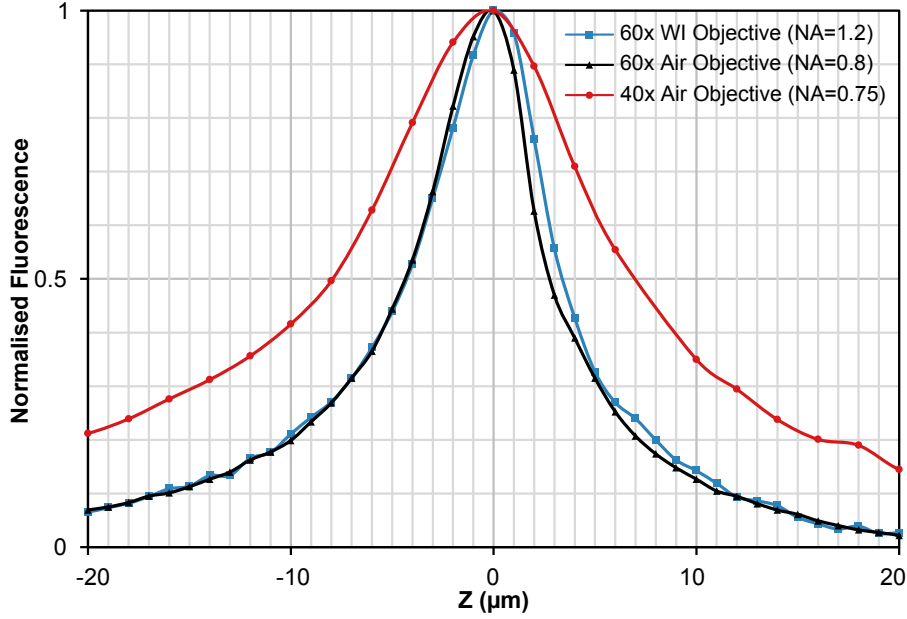


Figure 4.5: Axial profile of temporally focused beam with different objectives. The axial response of the system for different objectives was tested by measuring the fluorescent signal from a thin layer of $0.054\ \mu\text{m}$ green fluorescent beads using a cooled CCD camera (Clara, Andor). The axial FWHM is considerably larger when using the 40x objective compared to using either of the 60x objectives where the FWHMs are approximately equal ($7.5\ \mu\text{m}$).

objective whilst the other optics were kept unchanged. Three different objectives were used, 40x objective ($\text{NA} = 0.75$), a 60x air objective ($\text{NA} = 0.8$) and a 60x WI objective ($\text{NA} = 1.2$). Using a lower magnification objective lens increases the field of view at the expense of axial resolution compared to the 60x objectives resulting in a measured FWHM of $\sim 15\ \mu\text{m}$, as shown in Figure 4.5. The observed axial resolution obtained for both of the 60x objectives was found to be approximately the same despite different NAs. This is unexpected because axial resolution when using temporal focusing is dependent on the NA ($Z_R \approx \frac{\lambda}{\text{NA}^2}$) [112, 111]. A possible explanation for this is that the spread of the spectral components was not sufficient to make use of the full NA of the objective. This could be improved by using a different diffraction grating with a greater number of lines/mm.

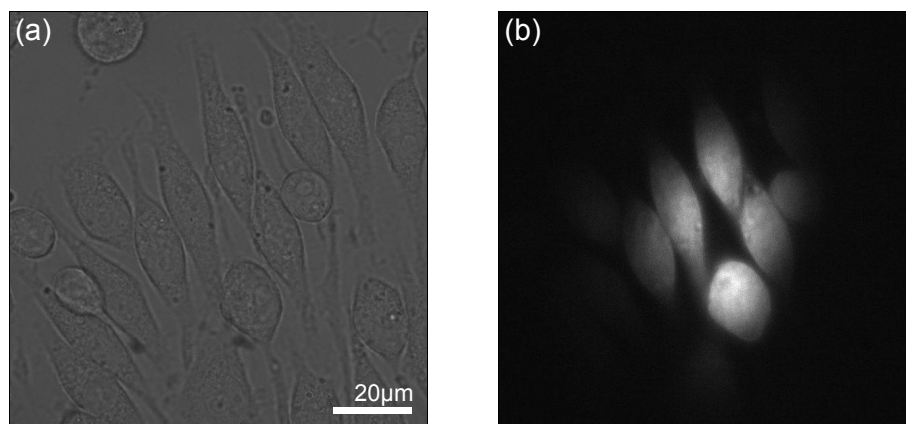


Figure 4.6: Fluorescence image of CHO-K1 cells with calcein-AM (CAM). (a) A bright field image of the CHO-K1 cells. (b) A fluorescence image taken using the temporal focusing system of the same cells stained with CAM. The shape and intensity of the observed fluorescence is a result of the Gaussian laser profile.

4.4.2 Imaging of adherent Chinese hamster ovary cells

After looking at the axial resolution using a thin fluorescent layer, the system was tested using adherent CHO-K1 cells stained with calcein-AM (CAM). The calcein can be excited through two-photon excitation using the femtosecond laser. The CHO-K1 cells were cultured and plated onto glass bottomed dishes as previously described in Section 2.7 and Section 3.8.1. The dish of living cells was incubated with CAM for 20 minutes before it was washed with D-PBS and imaged using the temporal focusing system. An example of the acquired images are shown in Figure 4.6. These images were taken using the 60x air objective ($NA = 0.8$). It should be noted that the intensity of the fluorescence is not uniform across the whole area. This is a result of the Gaussian profile of the laser. A second example is shown in Figure 4.7 where a stack of images has been acquired with $1\ \mu\text{m}$ intervals scanning from the bottom to the top of the cell (left to right). The centre of the cell shows more fluorescence partly due to the previously mentioned non-uniformity of the excitation profile and partly due to the bulbous topology of the cell.

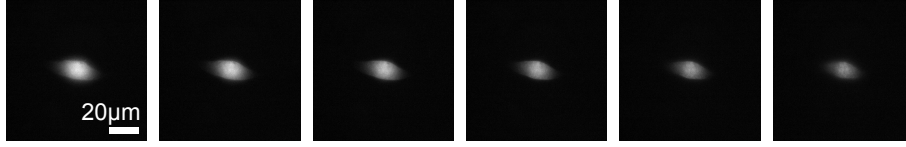


Figure 4.7: Z stack of fluorescence images of CHO-K1 cells with CAM. A series of fluorescence images taken using the temporal focusing setup moving from the bottom to the top of the cell in $1\ \mu\text{m}$ steps by moving the objective.

4.4.3 Temporal focusing for imaging optically trapped cells

Once images had been acquired of adherent CHO-K1 cells, the next step was to combine the temporally focused illumination with optical trapping. In order to obtain good 3D trapping the 60x WI objective lens was used. To prepare the sample, trypsinised cells (after neutralising the trypsin with MEM) were added to a dish containing $2\ \mu\text{M}$ of CAM in MEM. These cells were incubated for 20 min before pipetting to resuspend the CAM stained cells. A small aliquot of these cells were added to a glass bottom dish containing 1 ml of D-PBS.

The trapping laser was set to provide 100 mW at the back aperture. The femtosecond laser was set to 150 mW, also measured at the back aperture. A single cell was selected from the population and optically trapped in 3D. Figure 4.8 shows a series of images from an optically trapped cell. Unlike the adherent cells, the microscope objective was not moved between frames. Instead, the cells was moved axially by applying an appropriate Fresnel lens to the SLM. In Figure 4.8 each image is separated axially by $1\ \mu\text{m}$ as calibrated in the previous chapter (See section 3.6.4).

A second trap was created on the SLM such that the power in each trap was approximately equal. The power at the back aperture was increased to 200 mW. Two CHO-K1 cells were trapped simultaneously in the two SLM-generated optical traps. The two cells were moved next to each other using the LabVIEW interface. A series of brightfield and fluorescence images from a pair of trapped cells is shown

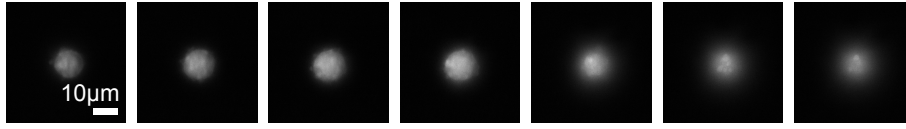


Figure 4.8: Z stack of fluorescence images of an single optically trapped CHO-K1 cell with CAM. A series of fluorescence images taken using the temporal focusing setup moving from the bottom to the top of the cells in $1\ \mu\text{m}$ steps by adjusting the trap position with the SLM.

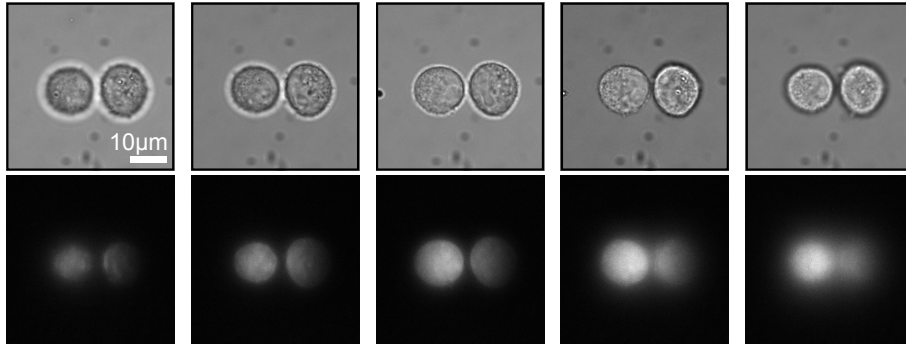


Figure 4.9: Z stack of fluorescence images of two optically trapped CHO-K1 cells with CAM. A series of fluorescence images taken using the temporal focusing setup moving from the bottom to the top of the cells in $1\ \mu\text{m}$ steps by adjusting the trap positions with the SLM.

in Figure 4.9. The Fresnel lens was adjusted to move the pair of cells through the plane of the temporally focused light. It should be noted that the cell on the right fluoresces less strongly as it is nearer the edge of the excitation region.

As the system combines both configurable optical traps with temporally focused illumination, it is relatively straight forward to bring a pair of cells close together or in contact. A potential application is to observe cell-cell interactions at video rates by optically trapping a pair of cells which have appropriate fluorescent markers.

4.5 Conclusions and future work

In this chapter the workstation outlined in the previous chapter (Section 3.3) was modified to provide a platform which combined both temporal focusing for multi-

photon illumination with optical trapping for the micro-manipulation of cells. The benefits of temporal focusing where the temporal profile of femtosecond pulses are focused rather than the spatial profile were discussed. Temporal focusing allows for multi-photon imaging without the requirement for scanning a single point. By temporally focusing the light, the lateral and axial resolutions are effectively decoupled which allows for the excitation area to be altered without affecting the axial resolution of the system.

The system was first tested with a thin layer of small, 0.054 μm diameter, green fluorescent beads. The axial FWHM using a 60x objective was measured to be 7.5 μm in the system. This could potentially be improved by optimising the grating used for temporal focusing. As shown in Figure 4.5, there was no difference observed between the two 60x magnification objectives ($\text{NA} = 0.8$ and $\text{NA} = 1.2$). This suggested that the spectral components were not separated sufficiently to make use of the full NA of the water immersion objective lens which had the highest NA tested. Alternatively, a laser system which provides ultra-short pulses with dispersion compensation would potentially yield better axial resolution.

CHO-K1 cells were stained with CAM and imaged with the temporal focusing system. Whilst the technique covered a much larger area simultaneously compared to a focused beam, the illumination was not flat due to the laser profile. This should be considered when choosing the size of the excitation area. Recently trypsinised cells were optically trapped and imaged. The SLM included in the trapping optical arm allows for control over 3D positioning of trapped cells. This was demonstrated by trapping two cells simultaneously next to one another. The pair of cells could be scanned axially by applying the appropriate Fresnel lenses to the SLM without the need to move the objective lens. In this configuration, the optically trapped cells were moved through the plane of temporally focused femtosecond light. This system

could be applied to looking at cell-cell interactions. Using temporal focusing allows for the full cells to be imaged without the need for scanning. This allows for faster acquisition rates compared to scanning techniques whilst optical trapping provides the means to move a pair of cells into proximity of each other in a controlled way.

4.6 Contributions

The system was designed and built by H. Rendall. H. Rendall carried out all the reported experiments and subsequent data analysis.

4. TEMPORAL FOCUSING FOR MULTIPHOTON IMAGING OF OPTICALLY TRAPPED CELLS

5

Summary and future work

5.1 Summary

This thesis began by discussing two tools for use in biophotonics: photoporation for the sterile injection of membrane-impermeable substances into cells and optical trapping for manipulating microscopic particles. These tools were then used in different permutations for photoporation and imaging of adherent and non-adherent mammalian cells. Chapter 2 described the properties of fluids at the micron scale where mixing occurs only by diffusion. Methods of exploiting these properties, present in low Reynolds number flows, for both 1D and 2D hydrodynamic focusing were then discussed. This was followed by a look at the properties of the propagation-invariant Bessel beam and how this beam can be generated. These tools were combined to create a new method for optical injection in a microfluidic chip. The chip was designed so that the ‘non-diffracting’ Bessel beam core could be placed in the centre of the channel, parallel to the flow of cells. An off-chip approach was used for 2D hydrodynamic focusing which was fabricated and evaluated. It enabled confinement of over 95% of the sample into a region where it would be irradiated by the fs laser. This is a great improvement compared to 20% which is achieved without hydrodynamic focusing. The parallel orientation of the photoporation beam and

the microfluidic flow allowed for higher flow rates to be used whilst still achieving successful optical injection. This was demonstrated by the optical injection of two cell lines, human promyelocytic leukemia (HL-60) cells and Chinese hamster ovary (CHO-K1) cells with viable injection efficiencies of $20.4 \pm 4.2\%$ and $31.0 \pm 9.5\%$ respectively. Throughput was increased by an order of magnitude compared to the previous microfluidic photoporation design by up to 10 cells per second.

The third chapter introduced a multimodal workstation for photoporation studies with optical trapping capabilities. The aim was to have a system capable of probing the parameter space for injection and transfection of non-adherent cells. Methods of beam steering were discussed and evaluated for both photoporation and optical trapping. The system contained two spatial light modulators (SLMs) for 3D beam control within a custom user-interface. Trap stiffness measurements were taken and a series of optical injection studies were performed on adherent CHO-K1 cells. Attempts were made to obtain optical transfection. However, this goal has remained elusive. Once transfection of non-adherent cells has been achieved, the system should be equipped to look at the parameters for transfection of non-adherent cells. This could provide useful information when considering transfection in other environments such as in a microfluidic flow.

In Chapter 4, the workstation outlined in Chapter 3 was modified to create a system which combined optical trapping with temporal focusing for multiphoton illumination. A grating was used to create a region at the sample plane where the femtosecond laser was temporally focused rather than spatially focused. This allowed for scannless multiphoton imaging of CHO-K1 cells. The axial resolution of the system was measured for different objectives and magnifications. A series of images of a CHO-K1 cell was acquired with z-sectioning achieved by moving the trap position axially. This experiment was repeated for a pair of optically trapped cells

stained with calcein-AM (CAM). Future work could include optimising the system for better axial resolution. Additionally by using appropriate markers, a pair of trapped cells could be manipulated and imaged to study cell-cell interactions.

5.2 Future work

Based on the work presented in this thesis, several avenues are possible for future work. The microfluidic photoporation system outlined in Chapter 2 has demonstrated optical injection but not transfection. A natural step would be to aim for transfection using this system in order to achieve high-throughput optical transfection. Very recently, Breunig et al have reported optical transfection on a microfluidic chip [121, 122]. The design incorporates a Bessel beam, as was used in the system presented in Chapter 2. However, there are some differences between the two systems. A microfluidic flow cell and Bessel beam were used in an orthogonal geometry. The core of the Bessel beam was then line-scanned across the channel, perpendicular to the flow of cells. A sub-15 fs Ti:sapphire laser was used for photoporation. The orthogonal geometry restricts the interaction time to a maximum of 1 ms and scanning the microfluidic channel results in 3-14% coverage of the cell flow. The reported transfection efficiency of CHO cells with GFP plasmid was ~2% though it was not stated how much variation there was between experiments. In order to improve the system outlined in Chapter 2, it is possible that using an ultrashort femtosecond laser (i.e. sub 20 fs pulses) may be beneficial in order to obtain transfection at low exposure times. Furthermore by incorporating hydrodynamic focusing rather than line-scanning, a far greater percentage of cells would receive a femtosecond dose leading to improved transfection efficiencies.

Work involving the photoporation workstation could be continued by investi-

gating optical transfection of non-adherent cells. Little work has been published involving transfection of non-adherent cells so a study of the parameter space for successful injection and transfection would be invaluable for further microfluidic photoporation experiments. This could be achieved either by photoporating an optically trapped cell in order to improve consistency of targeting the cell membrane or by using the optical trap as a means of separating targeted cells from the non-treated population. The latter could be realised using a microfluidic chip with multiple reservoirs for treated and untreated cells. This would allow a better understanding of photoporation efficiencies as the small subset of treated cells would not be lost among untreated cells.

Future work for the temporal focusing imaging system outlined in Chapter 4 could include optimising the system for better axial resolution. This could be achieved by decreasing the line spacing on the grating to ensure the full NA of the objective lens is used. Alternatively, using shorter laser pulses (i.e. ~ 10 fs rather than ~ 100 fs) could yield better results. The combination of optical trapping with temporally focused illumination could be used to image a pair of trapped cells to study cell-cell interactions. Optical tweezers provide a method for bringing two cells together in a controlled way and temporal focusing offers good axial resolution without scanning.

Throughout this thesis, a range of techniques have been combined in order to address limitations of current methods or to facilitate new studies of non-adherent cells. Combining different modalities provides a wide toolset for further biological investigations.

Bibliography

- [1] M. Tsukakoshi, S. Kurata, Y. Nomiya, Y. Ikawa, and T. Kasuya, “A novel method of DNA transfection by laser microbeam cell surgery,” *Applied Physics B Photophysics and Laser Chemistry*, vol. 35, pp. 135–140, Nov. 1984.
- [2] G. Palumbo, M. Caruso, E. Crescenzi, M. F. Tecce, G. Roberti, and A. Colasanti, “Targeted gene transfer in eucaryotic cells by dye-assisted laser optoporation,” *Journal of Photochemistry and Photobiology. B, Biology*, vol. 36, pp. 41–46, Oct. 1996.
- [3] H. Schneckenburger, A. Hendinger, R. Sailer, W. S. L. Strauss, and M. Schmitt, “Laser-assisted optoporation of single cells,” *Journal of Biomedical Optics*, vol. 7, pp. 410–6, July 2002.
- [4] L. Paterson, B. Agate, M. Comrie, R. Ferguson, T. Lake, J. Morris, A. Caruthers, C. T. A. Brown, W. Sibbett, P. Bryant, F. Gunn-Moore, A. Riches, and K. Dholakia, “Photoporation and cell transfection using a violet diode laser,” *Optics Express*, vol. 13, pp. 595–600, Jan. 2005.
- [5] U. K. Tirlapur and K. König, “Targeted transfection by femtosecond laser,” *Nature*, vol. 418, pp. 290–291, July 2002.
- [6] S. K. Mohanty, M. Sharma, and P. K. Gupta, “Laser-assisted microinjection into targeted animal cells,” *Biotechnology Letters*, vol. 25, pp. 895–899, June 2003.
- [7] D. J. Stevenson, F. J. Gunn-Moore, P. Campbell, and K. Dholakia, “Transfection by optical injection,” in *Handbook of Photonics for Biomedical Science* (V. V. Tuchin, ed.), ch. 3, pp. 87–118, CRC Press, 2010.
- [8] Y. Zhang and L. C. Yu, “Single-cell microinjection technology in cell biology,” 2008.
- [9] T. Y. Tsong, “Electroporation of cell membranes,” *Biophysical Journal*, vol. 60, no. 2, pp. 297–306, 1991.
- [10] P. L. Felgner, T. R. Gadek, M. Holm, R. Roman, H. W. Chan, M. Wenz, J. P. Northrop, G. M. Ringold, and M. Danielsen, “Lipofection: a highly efficient, lipid-mediated DNA-transfection procedure,” *Proceedings of the National Academy of Sciences of the United States of America*, vol. 84, no. 21, pp. 7413–7417, 1987.

- [11] K. L. Douglas, “Toward development of artificial viruses for gene therapy: A comparative evaluation of viral and non-viral transfection,” in *Biotechnology Progress*, vol. 24, pp. 871–883, 2008.
- [12] A. Vogel, J. Noack, G. Hüttman, and G. Paltauf, “Mechanisms of femtosecond laser nanosurgery of cells and tissues,” *Applied Physics B*, vol. 81, pp. 1015–1047, Nov. 2005.
- [13] A. V. Nikolskaya, V. P. Nikolski, and I. R. Efimov, “Gene printer: laser-scanning targeted transfection of cultured cardiac neonatal rat cells,” *Cell Communication & Adhesion*, vol. 13, no. 4, pp. 217–22, 2006.
- [14] M. L. Torres-Mapa, L. Angus, M. Ploschner, K. Dholakia, and F. J. Gunn-Moore, “Transient transfection of mammalian cells using a violet diode laser,” *Journal of Biomedical Optics*, vol. 15, no. 4, p. 041506, 2010.
- [15] A. P. Rudhall, M. Antkowiak, X. Tsampoula, M. Mazilu, N. K. Metzger, F. Gunn-Moore, and K. Dholakia, “Exploring the ultrashort pulse laser parameter space for membrane permeabilisation in mammalian cells,” *Scientific Reports*, vol. 2, p. 858, Jan. 2012.
- [16] A. Uchugonova, K. König, R. Bueckle, A. Isemann, and G. Tempea, “Targeted transfection of stem cells with sub-20 femtosecond laser pulses,” *Optics Express*, vol. 16, pp. 9357–64, June 2008.
- [17] M. Antkowiak, M. L. Torres-Mapa, D. J. Stevenson, K. Dholakia, and F. J. Gunn-Moore, “Femtosecond optical transfection of individual mammalian cells,” *Nature Protocols*, vol. 8, pp. 1216–1233, May 2013.
- [18] S. Backus, C. G. Durfee III, M. M. Murnane, and H. C. Kapteyn, “High power ultrafast lasers,” *Review of Scientific Instruments*, vol. 69, no. 1, p. 1207, 1998.
- [19] M. Antkowiak, M. L. Torres-Mapa, E. C. Witts, G. B. Miles, K. Dholakia, and F. J. Gunn-Moore, “Fast targeted gene transfection and optogenetic modification of single neurons using femtosecond laser irradiation,” *Scientific Reports*, vol. 3, p. 3281, Jan. 2013.
- [20] M. L. Torres-Mapa, M. Antkowiak, H. Cizmarova, D. E. K. Ferrier, K. Dholakia, and F. J. Gunn-Moore, “Integrated holographic system for all-optical manipulation of developing embryos,” *Biomedical Optics Express*, vol. 2, pp. 1564–75, June 2011.
- [21] C. A. Mitchell, S. Kalies, T. Cizmár, A. Heisterkamp, L. Torrance, A. G. Roberts, F. J. Gunn-Moore, and K. Dholakia, “Femtosecond optoinjection of intact tobacco BY-2 cells using a reconfigurable photoporation platform,” *PloS One*, vol. 8, p. e79235, Jan. 2013.

-
- [22] D. J. Stevenson, F. J. Gunn-Moore, P. Campbell, and K. Dholakia, "Single cell optical transfection," *Journal of the Royal Society, Interface / the Royal Society*, vol. 7, pp. 863–71, June 2010.
- [23] X. Tsampoula, V. Garces-Chavez, M. Comrie, D. J. Stevenson, B. Agate, C. T. A. Brown, F. Gunn-Moore, and K. Dholakia, "Femtosecond cellular transfection using a nondiffracting light beam," *Applied Physics Letters*, vol. 91, no. 5, p. 053902, 2007.
- [24] T. Cizmar, V. Kollarova, X. Tsampoula, F. Gunn-Moore, W. Sibbett, Z. Bouchal, and K. Dholakia, "Generation of multiple Bessel beams for a biophotonics workstation," *Optics Express*, vol. 16, p. 14024, Aug. 2008.
- [25] M. Antkowiak, M. L. Torres-Mapa, F. Gunn-Moore, and K. Dholakia, "Application of dynamic diffractive optics for enhanced femtosecond laser based cell transfection," *Journal of Biophotonics*, vol. 3, pp. 696–705, Oct. 2010.
- [26] R. F. Marchington, Y. Arita, X. Tsampoula, F. J. Gunn-Moore, and K. Dholakia, "Optical injection of mammalian cells using a microfluidic platform," *Biomedical Optics Express*, vol. 1, pp. 527–536, Jan. 2010.
- [27] H. A. Rendall, R. F. Marchington, B. B. Praveen, G. Bergmann, Y. Arita, A. Heisterkamp, F. J. Gunn-Moore, and K. Dholakia, "High-throughput optical injection of mammalian cells using a Bessel light beam," *Lab on a Chip*, vol. 12, pp. 4816–20, Nov. 2012.
- [28] Y. Arita, M. L. Torres-Mapa, W. M. Lee, T. Cizmar, P. Campbell, F. J. Gunn-Moore, and K. Dholakia, "Spatially optimized gene transfection by laser-induced breakdown of optically trapped nanoparticles," *Applied Physics Letters*, vol. 98, no. 9, p. 093702, 2011.
- [29] Y. Arita, M. Ploschner, M. Antkowiak, F. Gunn-Moore, and K. Dholakia, "Laser-induced breakdown of an optically trapped gold nanoparticle for single cell transfection," *Optics Letters*, vol. 38, pp. 3402–5, Sept. 2013.
- [30] A. N. Hellman, K. R. Rau, H. H. Yoon, and V. Venugopalan, "Biophysical response to pulsed laser microbeam-induced cell lysis and molecular delivery," *Journal of Biophotonics*, vol. 1, pp. 24–35, Mar. 2008.
- [31] Y. Arita, M. Antkowiak, V. Venugopalan, F. J. Gunn-Moore, and K. Dholakia, "Dynamics of primary and secondary microbubbles created by laser-induced breakdown of an optically trapped nanoparticle," *Physical Review E*, vol. 85, p. 016319, Jan. 2012.

- [32] M. Schomaker, J. Baumgart, A. Ngezahayo, J. Bullerdiek, I. Nolte, H. Murua Escobar, H. Lubatschowski, and A. Heisterkamp, "Plasmonic perforation of living cells using ultrashort laser pulses and gold nanoparticles," in *Proc. SPIE 7192* (T. Vo-Dinh and J. R. Lakowicz, eds.), vol. 7192, p. 71920U, Feb. 2009.
- [33] S. Kalies, D. Heinemann, M. Schomaker, H. M. Escobar, A. Heisterkamp, T. Ripken, and H. Meyer, "Plasmonic laser treatment for Morpholino oligomer delivery in antisense applications," *Journal of Biophotonics*, vol. 9, pp. 1–9, June 2013.
- [34] D. Heinemann, M. Schomaker, S. Kalies, M. Schieck, R. Carlson, H. Murua Escobar, T. Ripken, H. Meyer, and A. Heisterkamp, "Gold nanoparticle mediated laser transfection for efficient siRNA mediated gene knock down," *PLoS One*, vol. 8, p. e58604, Jan. 2013.
- [35] M. Schomaker, D. Killian, S. Willenbrock, E. Diebold, E. Mazur, W. Bintig, A. Ngezahayo, I. Nolte, H. Murua Escobar, C. Junghanß, H. Lubatschowski, and A. Heisterkamp, "Ultrashort laser pulse cell manipulation using nano- and micro- materials," in *Proc. SPIE 7762* (K. Dholakia and G. C. Spalding, eds.), vol. 7762, p. 77623G, Aug. 2010.
- [36] D. Heinemann, S. Kalies, M. Schomaker, W. Ertmer, H. Murua Escobar, H. Meyer, and T. Ripken, "Delivery of proteins to mammalian cells via gold nanoparticle mediated laser transfection," *Nanotechnology*, vol. 25, p. 245101, June 2014.
- [37] S. Kalies, L. Gentemann, M. Schomaker, D. Heinemann, T. Ripken, and H. Meyer, "Surface modification of silica particles with gold nanoparticles as an augmentation of gold nanoparticle mediated laser perforation," *Biomedical Optics Express*, vol. 5, pp. 2686–96, Aug. 2014.
- [38] M. Schomaker, D. Heinemann, S. Kalies, S. Willenbrock, H. Murua Escobar, A. Buch, B. Sodeik, T. Ripken, and H. Meyer, "Mechanistic investigations and molecular medicine applications of gold nanoparticle mediated (GNOME) laser transfection," in *Proc. SPIE 8972* (A. Heisterkamp, P. R. Herman, M. Meunier, and S. Nolte, eds.), vol. 8972, p. 897207, Mar. 2014.
- [39] A. Ashkin, "Acceleration and Trapping of Particles by Radiation Pressure," *Physical Review Letters*, vol. 24, pp. 156–159, Jan. 1970.
- [40] M. P. MacDonald, G. C. Spalding, and K. Dholakia, "Microfluidic sorting in an optical lattice," *Nature*, vol. 426, pp. 421–4, Nov. 2003.
- [41] M. M. Wang, E. Tu, D. E. Raymond, J. M. Yang, H. Zhang, N. Hagen, B. Dees, E. M. Mercer, A. H. Forster, I. Kariv, P. J. Marchand, and W. F.

- Butler, "Microfluidic sorting of mammalian cells by optical force switching," *Nature Biotechnology*, vol. 23, pp. 83–7, Jan. 2005.
- [42] S. M. Block, L. S. Goldstein, and B. J. Schnapp, "Bead movement by single kinesin molecules studied with optical tweezers," *Nature*, vol. 348, pp. 348–52, Nov. 1990.
- [43] Y. Arita, M. Mazilu, and K. Dholakia, "Laser-induced rotation and cooling of a trapped microgyroscope in vacuum," *Nature Communications*, vol. 4, p. 2374, Jan. 2013.
- [44] A. Ashkin, "Forces of a single-beam gradient laser trap on a dielectric sphere in the ray optics regime," *Biophysical Journal*, vol. 61, pp. 569–582, Feb. 1992.
- [45] T. Imasaka, Y. Kawabata, T. Kaneta, and Y. Ishidzu, "Optical chromatography," *Analytical Chemistry*, vol. 67, no. 7, pp. 1763–1765, 1995.
- [46] A. Ashkin, "Stability of optical levitation by radiation pressure," *Applied Physics Letters*, vol. 24, no. 12, p. 586, 1974.
- [47] K. Svoboda and S. M. Block, "Biological applications of optical forces," *Annual Review of Biophysics and Biomolecular Structure*, vol. 23, pp. 247–85, Jan. 1994.
- [48] J. E. Molloy and M. J. Padgett, "Lights, action: Optical tweezers," *Contemporary Physics*, vol. 43, pp. 241–258, July 2002.
- [49] W. M. Lee, P. J. Reece, R. F. Marchington, N. K. Metzger, and K. Dholakia, "Construction and calibration of an optical trap on a fluorescence optical microscope," *Nature Protocols*, vol. 2, pp. 3226–38, Jan. 2007.
- [50] T. Perkins, "Optical traps for single molecule biophysics: a primer," *Laser & Photonics Review*, vol. 3, pp. 203–220, Feb. 2009.
- [51] C. McDougall, D. J. Stevenson, C. T. A. Brown, F. Gunn-Moore, and K. Dholakia, "Targeted optical injection of gold nanoparticles into single mammalian cells," *Journal of Biophotonics*, vol. 2, pp. 736–43, Dec. 2009.
- [52] M. Waleed, S.-U. Hwang, J.-D. Kim, I. Shabbir, S.-M. Shin, and Y.-G. Lee, "Single-cell optoporation and transfection using femtosecond laser and optical tweezers," *Biomedical Optics Express*, vol. 4, pp. 1533–47, Jan. 2013.
- [53] B. B. Praveen, D. J. Stevenson, M. Antkowiak, K. Dholakia, and F. J. Gunn-Moore, "Enhancement and optimization of plasmid expression in femtosecond optical transfection," *Journal of Biophotonics*, vol. 4, pp. 229–35, Apr. 2011.

- [54] T. Squires and S. Quake, "Microfluidics: Fluid physics at the nanoliter scale," *Reviews of Modern Physics*, vol. 77, pp. 977–1026, Oct. 2005.
- [55] J. P. Brody, P. Yager, R. E. Goldstein, and R. H. Austin, "Biotechnology at low Reynolds numbers," *Biophysical Journal*, vol. 71, pp. 3430–41, Dec. 1996.
- [56] G.-B. Lee, C.-C. Chang, S.-B. Huang, and R.-J. Yang, "The hydrodynamic focusing effect inside rectangular microchannels," *Journal of Micromechanics and Microengineering*, vol. 16, pp. 1024–1032, May 2006.
- [57] B. H. Weigl, R. L. Bardell, and C. R. Cabrera, "Lab-on-a-chip for drug development," *Advanced Drug Delivery Reviews*, vol. 55, pp. 349–377, Feb. 2003.
- [58] A. D. Stroock, S. K. W. Dertinger, A. Ajdari, I. Mezic, H. a. Stone, and G. M. Whitesides, "Chaotic mixer for microchannels," *Science (New York, N.Y.)*, vol. 295, pp. 647–51, Jan. 2002.
- [59] J. D. Tice, H. Song, A. D. Lyon, and R. F. Ismagilov, "Formation of Droplets and Mixing in Multiphase Microfluidics at Low Values of the Reynolds and the Capillary Numbers," *Langmuir*, vol. 19, pp. 9127–9133, Oct. 2003.
- [60] A. E. Kamholz, B. H. Weigl, B. A. Finlayson, and P. Yager, "Quantitative Analysis of Molecular Interaction in a Microfluidic Channel: The T-Sensor," *Analytical Chemistry*, vol. 71, pp. 5340–5347, Dec. 1999.
- [61] A. Y. Lau, L. P. Lee, and J. W. Chan, "An integrated optofluidic platform for Raman-activated cell sorting," *Lab on a Chip*, vol. 8, pp. 1116–20, July 2008.
- [62] T. D. Perroud, J. N. Kaiser, J. C. Sy, T. W. Lane, C. S. Branda, A. K. Singh, and K. D. Patel, "Microfluidic-based cell sorting of *Francisella tularensis* infected macrophages using optical forces," *Analytical Chemistry*, vol. 80, pp. 6365–72, Aug. 2008.
- [63] A. Wolff, I. R. Perch-Nielsen, U. D. Larsen, P. Friis, G. Goranovic, C. R. Poulsen, J. P. Kutter, and P. Telleman, "Integrating advanced functionality in a microfabricated high-throughput fluorescent-activated cell sorter," *Lab on a Chip*, vol. 3, pp. 22–7, Feb. 2003.
- [64] N. Sundararajan, M. Pio, L. Lee, and A. Berlin, "Three-Dimensional Hydrodynamic Focusing in Polydimethylsiloxane (PDMS) Microchannels," *Journal of Microelectromechanical Systems*, vol. 13, pp. 559–567, Aug. 2004.
- [65] C. Simonnet and A. Groisman, "Two-dimensional hydrodynamic focusing in a simple microfluidic device," *Applied Physics Letters*, vol. 87, no. 11, p. 114104, 2005.

-
- [66] P. B. Howell, J. P. Golden, L. R. Hilliard, J. S. Erickson, D. R. Mott, and F. S. Ligler, “Two simple and rugged designs for creating microfluidic sheath flow,” *Lab on a Chip*, vol. 8, pp. 1097–1103, July 2008.
- [67] J. P. Golden, J. S. Kim, J. S. Erickson, L. R. Hilliard, P. B. Howell, G. P. Anderson, M. Nasir, and F. S. Ligler, “Multi-wavelength microflow cytometer using groove-generated sheath flow,” *Lab on a Chip*, vol. 9, pp. 1942–50, July 2009.
- [68] X. Mao, J. R. Waldeisen, and T. J. Huang, ““Microfluidic drifting”—implementing three-dimensional hydrodynamic focusing with a single-layer planar microfluidic device,” *Lab on a Chip*, vol. 7, pp. 1260–2, Oct. 2007.
- [69] M. G. Lee, S. Choi, and J.-K. Park, “Three-dimensional hydrodynamic focusing with a single sheath flow in a single-layer microfluidic device,” *Lab on a Chip*, vol. 9, pp. 3155–60, Nov. 2009.
- [70] Y. Yamaguchi, F. Takagi, K. Yamashita, H. Nakamura, H. Maeda, K. Sotowa, K. Kusakabe, Y. Yamasaki, and S. Morooka, “3-D simulation and visualization of laminar flow in a microchannel with hair-pin curves,” *AIChE Journal*, vol. 50, pp. 1530–1535, July 2004.
- [71] J. Durnin, “Exact solutions for nondiffracting beams. I. The scalar theory,” *Journal of the Optical Society of America A*, vol. 4, p. 651, Apr. 1987.
- [72] J. Arlt, V. Garces-Chavez, W. Sibbett, and K. Dholakia, “Optical micro-manipulation using a Bessel light beam,” *Optics Communications*, vol. 197, pp. 239–245, Oct. 2001.
- [73] L. Paterson, E. Papagiakoumou, G. Milne, V. Garces-Chavez, S. a. Tatarkova, W. Sibbett, F. J. Gunn-Moore, P. E. Bryant, a. C. Riches, and K. Dholakia, “Light-induced cell separation in a tailored optical landscape,” *Applied Physics Letters*, vol. 87, no. 12, p. 123901, 2005.
- [74] T. A. Planchon, L. Gao, D. E. Milkie, M. W. Davidson, J. A. Galbraith, C. G. Galbraith, and E. Betzig, “Rapid three-dimensional isotropic imaging of living cells using Bessel beam plane illumination,” *Nature Methods*, vol. 8, pp. 417–23, May 2011.
- [75] D. McGloin and K. Dholakia, “Bessel beams: Diffraction in a new light,” *Contemporary Physics*, vol. 46, pp. 15–28, Jan. 2005.
- [76] J. Durnin, J. J. Miceli, Jr., and J. H. Eberly, “Diffraction-free beams,” *Physical Review Letters*, vol. 58, pp. 1499–1501, Apr. 1987.

- [77] Y. Lin, W. Seka, J. H. Eberly, H. Huang, and D. L. Brown, “Experimental investigation of Bessel beam characteristics,” *Applied Optics*, vol. 31, pp. 2708–2713, May 1992.
- [78] G. Indebetouw, “Nondiffracting optical fields: some remarks on their analysis and synthesis,” *Journal of the Optical Society of America A*, vol. 6, p. 150, Jan. 1989.
- [79] S. H. Tao, X.-C. Yuan, and B. S. Ahluwalia, “The generation of an array of nondiffracting beams by a single composite computer generated hologram,” *Journal of Optics A: Pure and Applied Optics*, vol. 7, pp. 40–46, Jan. 2005.
- [80] R. MacDonald, S. Boothroyd, T. Okamoto, J. Chrostowski, and B. Syrett, “Interboard optical data distribution by Bessel beam shadowing,” *Optics Communications*, vol. 122, pp. 169–177, Jan. 1996.
- [81] Z. Bouchal, J. Wagner, and M. Chlup, “Self-reconstruction of a distorted nondiffracting beam,” *Optics Communications*, vol. 151, pp. 207–211, June 1998.
- [82] J. Durnin, J. J. Miceli, and J. H. Eberly, “Comparison of Bessel and Gaussian beams,” *Optics Letters*, vol. 13, p. 79, Feb. 1988.
- [83] A. Terray and S. J. Hart, ““Off-the-shelf” 3-D microfluidic nozzle,” *Lab on a Chip*, vol. 10, pp. 1729–1731, July 2010.
- [84] O. Brzobohatý, T. Cizmár, and P. Zemánek, “High quality quasi-Bessel beam generated by round-tip axicon,” *Optics Express*, vol. 16, pp. 12688–700, Aug. 2008.
- [85] T. Čižmár, L. C. D. Romero, K. Dholakia, and D. L. Andrews, “Multiple optical trapping and binding: new routes to self-assembly,” *Journal of Physics B: Atomic, Molecular and Optical Physics*, vol. 43, p. 102001, May 2010.
- [86] B. E. A. Saleh, M. C. Teich, and C. J. Wiley, “Acousto-optics,” in *Fundamentals of Photonics*, ch. 20, p. 992, John Wiley & Sons, first ed., 1991.
- [87] K. Visscher, S. Gross, and S. Block, “Construction of multiple-beam optical traps with nanometer-resolution position sensing,” *IEEE Journal of Selected Topics in Quantum Electronics*, vol. 2, no. 4, pp. 1066–1076, 1996.
- [88] G. Duemani Reddy, K. Kelleher, R. Fink, and P. Saggau, “Three-dimensional random access multiphoton microscopy for functional imaging of neuronal activity,” *Nature Neuroscience*, vol. 11, pp. 713–20, June 2008.

-
- [89] G. Milne, D. Rhodes, M. MacDonald, and K. Dholakia, “Fractionation of poly-disperse colloid with acousto-optically generated potential energy landscapes,” *Optics Letters*, vol. 32, p. 1144, May 2007.
- [90] T. Čižmár, H. I. C. Dalgarno, P. C. Ashok, F. J. Gunn-Moore, and K. Dholakia, “Optical aberration compensation in a multiplexed optical trapping system,” *Journal of Optics*, vol. 13, p. 044008, Apr. 2011.
- [91] G. C. Spalding, J. Courtial, and R. D. Leonardo, “Holographic Optical Tweezers,” in *Structured Light and its Applications* (D. L. Andrews, ed.), ch. 6, pp. 139–168, Academic Press, first ed., 2008.
- [92] J. W. Goodman, *Introduction to Fourier Optics*. McGraw-Hill, second ed., 1996.
- [93] J. Liesener, M. Reicherter, T. Haist, and H. Tiziani, “Multi-functional optical tweezers using computer-generated holograms,” *Optics Communications*, vol. 185, pp. 77–82, Nov. 2000.
- [94] Newport, “The effect of dispersion on ultrashort pulses.” <http://www.newport.com/The-Effect-of-Dispersion-on-Ultrashort-Pulses/602091/1033/content.aspx>. Accessed March 2015.
- [95] P. Mthunzi, *Optical Sorting and Photo-transfection of Mammalian Cells*. Phd, 2010.
- [96] R. J. Noll, “Zernike polynomials and atmospheric turbulence,” *Journal of the Optical Society of America*, vol. 66, p. 207, Mar. 1976.
- [97] G. D. Love, “Wave-front correction and production of Zernike modes with a liquid-crystal spatial light modulator,” *Applied Optics*, vol. 36, p. 1517, Mar. 1997.
- [98] K. D. Wulff, D. G. Cole, R. L. Clark, R. DiLeonardo, J. Leach, J. Cooper, G. Gibson, and M. J. Padgett, “Aberration correction in holographic optical tweezers,” *Optics Express*, vol. 14, p. 4170, May 2006.
- [99] M. J. Booth, M. A. A. Neil, R. Juskaitis, and T. Wilson, “Adaptive aberration correction in a confocal microscope,” *Proceedings of the National Academy of Sciences of the United States of America*, vol. 99, pp. 5788–92, Apr. 2002.
- [100] D. Débarre, E. J. Botcherby, T. Watanabe, S. Srinivas, M. J. Booth, and T. Wilson, “Image-based adaptive optics for two-photon microscopy,” *Optics Letters*, vol. 34, p. 2495, Aug. 2009.

- [101] T. Čižmár, M. Mazilu, and K. Dholakia, “In situ wavefront correction and its application to micromanipulation,” *Nature Photonics*, vol. 4, pp. 388–394, May 2010.
- [102] P. Mthunzi, K. Dholakia, and F. Gunn-Moore, “Phototransfection of mammalian cells using femtosecond laser pulses: optimization and applicability to stem cell differentiation,” *Journal of Biomedical Optics*, vol. 15, no. 4, p. 041507, 2010.
- [103] S. Brunner, T. Sauer, S. Carotta, M. Cotten, M. Saltik, and E. Wagner, “Cell cycle dependence of gene transfer by lipoplex, polyplex and recombinant adenovirus,” *Gene Therapy*, vol. 7, no. 5, pp. 401–407, 2000.
- [104] D. Lechardeur, K. J. Sohn, M. Haardt, P. B. Joshi, M. Monck, R. W. Graham, B. Beatty, J. Squire, H. O’Brodvich, and G. L. Lukacs, “Metabolic instability of plasmid DNA in the cytosol: a potential barrier to gene transfer,” *Gene Therapy*, vol. 6, no. 4, pp. 482–497, 1999.
- [105] Addgene, “Addgene - pCAG-GFP Plasmid Data.” <https://www.addgene.org/11150/>. Accessed July 2014.
- [106] D. Stevenson, B. Agate, X. Tsampoula, P. Fischer, C. T. a. Brown, W. Sibbett, A. Riches, F. Gunn-Moore, and K. Dholakia, “Femtosecond optical transfection of cells: viability and efficiency,” *Optics Express*, vol. 14, pp. 7125–33, Aug. 2006.
- [107] M. Minsky, “Memoir on inventing the confocal scanning microscope,” *Scanning*, vol. 10, pp. 128–138, Aug. 1988.
- [108] W. Denk, J. H. Strickler, and W. W. Webb, “Two-photon laser scanning fluorescence microscopy,” *Science (New York, N.Y.)*, vol. 248, pp. 73–6, Apr. 1990.
- [109] D. Oron, E. Tal, and Y. Silberberg, “Scanningless depth-resolved microscopy,” *Optics Express*, vol. 13, pp. 1468–76, Mar. 2005.
- [110] E. Tal and Y. Silberberg, “Transformation from an ultrashort pulse to a spatiotemporal speckle by a thin scattering surface,” *Optics Letters*, vol. 31, no. 23, p. 3529, 2006.
- [111] D. Oron, E. Papagiakoumou, F. Anselmi, and V. Emiliani, *Two-photon optogenetics*, vol. 196. Elsevier B.V., 1 ed., Jan. 2012.
- [112] M. E. Durst, G. Zhu, and C. Xu, “Simultaneous spatial and temporal focusing for axial scanning,” *Optics Express*, vol. 14, pp. 12243–54, Dec. 2006.

-
- [113] G. Zhu, J. van Howe, M. Durst, W. Zipfel, and C. Xu, “Simultaneous spatial and temporal focusing of femtosecond pulses,” *Optics Express*, vol. 13, pp. 2153–9, Mar. 2005.
- [114] H. Dana and S. Shoham, “Numerical evaluation of temporal focusing characteristics in transparent and scattering media,” *Optics Express*, vol. 19, pp. 4937–48, Mar. 2011.
- [115] H. Dana, N. Kruger, A. Ellman, and S. Shoham, “Line temporal focusing characteristics in transparent and scattering media,” *Optics Express*, vol. 21, pp. 5677–87, Mar. 2013.
- [116] B. Sun, P. S. Salter, and M. J. Booth, “Effects of aberrations in spatiotemporal focusing of ultrashort laser pulses,” *Journal of the Optical Society of America. A, Optics, Image Science, and Vision*, vol. 31, pp. 765–72, Apr. 2014.
- [117] E. Papagiakoumou, F. Anselmi, A. Bègue, V. de Sars, J. Glückstad, E. Y. Isacoff, and V. Emiliani, “Scanless two-photon excitation of channelrhodopsin-2,” *Nature Methods*, vol. 7, pp. 848–54, Oct. 2010.
- [118] E. Papagiakoumou, V. de Sars, D. Oron, and V. Emiliani, “Patterned two-photon illumination by spatiotemporal shaping of ultrashort pulses,” *Optics Express*, vol. 16, pp. 22039–47, Dec. 2008.
- [119] E. Papagiakoumou, V. de Sars, V. Emiliani, and D. Oron, “Temporal focusing with spatially modulated excitation,” *Optics Express*, vol. 17, pp. 5391–401, Mar. 2009.
- [120] E. Tal, D. Oron, and Y. Silberberg, “Improved depth resolution in video-rate line-scanning multiphoton microscopy using temporal focusing,” *Optics Letters*, vol. 30, no. 13, p. 1686, 2005.
- [121] H. G. Breunig, A. Uchugonova, A. Batista, and K. König, “High-throughput continuous flow femtosecond laser-assisted cell optoporation and transfection,” *Microscopy Research and Technique*, vol. 00, pp. 1–6, Aug. 2014.
- [122] H. G. Breunig, A. Uchugonova, and K. König, “Towards optical cell transfection inside a micro flow cell,” in *Proc. SPIE 8947* (D. L. Farkas, D. V. Nicolau, and R. C. Leif, eds.), vol. 8947, p. 89471J, Mar. 2014.

BIBLIOGRAPHY

A

Appendix

A.1 Contents of supplementary CD

The supplementary CD which accompanies this thesis contains Matlab code and LabVIEW files which I have created.

The contents of the CD are:

- Measure Bessel beam (Matlab)
- Hydrodynamic focusing evaluation (LabVIEW)
- Workstation UI (LabVIEW)

‘Measure Bessel beam’ was used to measure the propagation length and core size of the Bessel beam generated in Chapter 2 (Section 2.6 and Figure 2.13). It measures the core size from a stack of images which have been captured at regular intervals along the Bessel beam. Plots of peak intensity and core size against position are produced.

‘Hydrodynamic focusing evaluation’ is a LabVIEW file used to evaluate the quality of 2D hydrodynamic focusing (Section 2.5 and Figure 2.10). It takes an AVI file of test particles (4 μm beads) flowing through the ‘s’-bend of the microfluidic channel (i.e. with an ‘end on’ view). The region of interest is chosen by the user to mark the channel walls and each frame is then processed to detect beads which are

in focus. The positions of the beads are recorded and saved as a CSV output for further analysis.

‘Workstation UI’ is a LabVIEW project used to control the workstation in Chapter 3 and Chapter 4. It includes control for two spatial light modulators (SLMs), a CCD camera (Basler piA640-210gm) and a mechanical shutter. Additional files have been included which were used for calibration of the ‘point and shoot’ and ‘drag and trap’ UI. Details of how the program is structured are included in Section 3.6.

These files were tested using LabVIEW 2012 and Matlab 2011.